Fakultät für Mathematik, Informatik und Naturwissenschaften | RWTH AACHEN UNIVERSITY

Thin Film Growth of Chalcogenide Compounds via Molecular Beam Epitaxy and Their Characterization

Von der Fakultät für Mathematik, Informatik und Naturwissenschaften der RWTH Aachen University zur Erlangung des akademischen Grades eines Doktors der Naturwissenschaften genehmigte Dissertation

vorgelegt von

Hetal Kanjibhai Vaishnav, M.Sc.
aus
Rajkot, India

Berichter*:* Prof. Dr. rer. nat. Matthias Wuttig

Prof. Dr. rer. nat. Joachim Mayer

Tag der mündlichen Prüfung*: 10.07.2025*

Forschungszentrum Jülich GmbH

Peter Grünberg Institute 10 (PGI-10)

JARA Institute Energy-efficient information technology (PGI-10)

Hetal, Vaishnav:

Thin Film Growth of Chalcogenide Compounds via Molecular Beam Epitaxy and Their Characterization

PhD Thesis, Forschungszentrum Jülich GmbH,

Peter Grünberg Institute 10, 2025

This thesis is dedicated to all the diligent girls out there who dream big and pursue their passions with courage and determination.

Abstract

In recent years, chalcogenide-based compounds have been found to have extensive applications across various fields, especially in data storage technologies. Chalcogenide-based phase change materials (PCMs) are particularly effective for binary data storage because they rapidly switch between a highly conductive crystalline state and a low-conductive amorphous state through Joule heating. The unique properties of this material class are assumed to originate from their unconventional bonding mechanism, the metavalent bonding. Studies indicate that confining PCMs in ultra-thin films can lead to distinct effects. However, several questions remain: To what extent properties can be tuned by changing film thickness? How does reducing film thickness affect their structure and properties, and how does this impact their phase-change behavior? Addressing these questions necessitates the development of highly textured thin-films to systematically explore these intricate phenomena.

This study focused on optimizing the growth conditions for chalcogenide-based thin films using molecular beam epitaxy (MBE) and thoroughly characterizing their atomic arrangement and properties. Highly textured thin films of SnTe, GeTe, and SnSe were deposited on various Si(111) surfaces, including 1x1, 7x7 reconstructed, and Sb-terminated Si surfaces. Subsequently the growth dynamics across these substrates were systematically compared. The first part of this study focuses on the epitaxial growth of GeTe on the three Si(111) surfaces, facilitating meaningful comparisons with related studies. Growth was monitored using in-situ Reflection High-Energy Electron Diffraction (RHEED) to examine the films' growth mode and surface reconstructions. On Si(111) 1x1 and 7x7 reconstructed surfaces, the GeTe films exhibit an amorphous-to-crystalline transition at the early stages of growth. In contrast, the films arrange directly into a crystalline phase on Sb-terminated surfaces. Further experimental work explored the influence of substrate temperature on the critical thickness for the amorphous-to-crystalline transition in GeTe films on the Si(111) 1x1 surface. Analysis of rotational domains via ARHEED and X-ray Diffraction (XRD) phi-scans reveals a strong suppression of twin domains on Sb-terminated surfaces. In contrast, twisted rotational domains appear on the 7x7 reconstructed surface. A growth series of GeTe thin films, ranging from 2 nm to 80 nm in thickness, is also presented, showing that thickness-dependent structural changes in GeTe correspond to confinement-induced modifications in chemical bonding. The second material investigated is SnTe. Its growth on Si(111) surfaces was compared, examining thickness-dependent lattice shifts in films grown on the Si(111) 1x1 surface using RHEED and XRD. Finally, the epitaxial growth of SnSe was studied on Si(111) 1x1, 7x7 reconstructed, and Sb-terminated surfaces. Highly textured SnSe films grow along the (100) direction on all three surfaces. Detailed XRD and Reciprocal Space Mapping analyses indicate that the ultra-thin SnSe films exhibit lattice distortions. Specifically, SnSe films transition from an orthorhombic Pnma phase towards a higher-symmetry Cmcm phase at thicknesses below 5 nm, a phenomenon observed through Raman spectroscopy. These findings enhance the understanding of thin film effects, providing valuable insights for their use in electronic and thermoelectric devices.

સારાંશ

તાજેતરના વર્ષોમાં, કેલ્કોજનાઇડ આધારિત સંયોજનોનું વિવિધ ક્ષેત્રોમાં, ખાસ કરીને ડેટા સ્ટોરેજ ટેકનોલોજીમાં વિશાળ ઉપયોગ જોવા મળે છે. કેલ્કોજનાઇડ આધારિત ફેઝ-ચેન્જ મટિરિયલ્સ (PCMs) બાઇનરી ડેટા સ્ટોરેજ માટે ખાસ અસરકારક સાબિત થાય છે, કારણ કે તેઓ જૂલ ગરમી દ્વારા ઉચ્ચ વાહકતા ધરાવતી સ્ફટિકાકાર સ્થિતિ અને નીચી વાહકતા ધરાવતી અનામોર્ફસ સ્થિતિ વચ્ચે ઝડપથી બદલાય છે. આ મટિરિયલ વર્ગના અન્ય ગુણધર્મો તેમની અસામાન્ય બોન્ડિંગ મિકેનિઝમ, મેટાવેલન્ટ બોન્ડિંગ,માંથી ઉભા થવા માને છે. અભ્યાસ સૂચવે છે કે, પીસીએમને અલ્ટ્રા-થિન ફિલ્મોમાં કરવાથી, જેમ કે સ્વયંસ્ફુરિત ક્રિસ્ટલાઇઝેશન જેવા અનન્ય અસરો થાય છે. તેમ છતાં કેટલાક પ્રશ્નો હજી બાકી છે: શું ગુણધર્મોને ફિલ્મની જાડાઈમાં ફેરફાર કરીને સુમેળમાં લાવી શકાય? જાડાઈ ઘટાડવાથી તેમની રચના અને પાયરલ્સ ડિસ્ટોર્શન પર શું અસર થાય છે, અને આ અસર તેમના ફેઝ-ચેન્જ વર્તનને કેવી રીતે અસર કરે છે? આ પ્રશ્નોના ઉકેલ માટે ઊંડાણપૂર્વક આ જટિલ ઘટનાઓનું અન્વેષણ કરવા માટે અત્યંત ટેક્સ્ચર્ડ થિન-ફિલ્મ માળખાંની જરૂરિયાત છે.

આ અભ્યાસ મોલેક્યુલર બીમ એપિટેક્સી (MBE) નો ઉપયોગ કરીને કેલ્કોજનાઇડ આધારિત થિન-ફિલ્મના વૃદ્ધિ પરિબળોને ઓપ્ટિમાઇઝ કરવા અને તેમની રચનાત્મક અને કાર્યાત્મક ગુણધર્મોની વિશેષિત રીતે વિશ્લેષણ પર કેન્દ્રિત છે. SnTe, GeTe અને SnSeના અત્યંત ટેક્સ્ચર્ડ થિન ફિલ્મોને વિવિધ Si(111) સપાટીઓ, જેમ કે 1x1, 7x7 પુનઃરચનાકૃત અને Sb-ટર્મિનેટેડ સપાટીઓ પર જમાવવામાં આવ્યા હતા, અને આ સબસ્ટ્રેટ્સમાં વૃદ્ધિ ગતિશીલતાનું તુલનાત્મક વિશ્લેષણ કરવામાં આવ્યું. આ અભ્યાસનો પહેલો ભાગ GeTeના Si(111) સપાટીઓ પર એપિટેક્ષિયલ વૃદ્ધિ પર કેન્દ્રિત છે, જે સંબંધિત અભ્યાસ સાથે અર્થપૂર્ણ તુલનાઓને સુલભ બનાવે છે. વૃદ્ધિને ઇન-સાઇટ્યુ રિફ્લેક્શન હાઈ-એનર્જી ઇલેક્ટ્રોન ડિફ્રેક્શન (RHEED) દ્વારા મોનિટર કરવામાં આવી હતી, જે ફિલ્મોની વૃદ્ધિ મોડ અને સપાટી પુનઃરચનાઓને તપાસવા માટે ઉપયોગી છે. Si(111) 1x1 અને 7x7 પુનઃરચનાકૃત સપાટીઓ પર, GeTe ફિલ્મો તેમના વૃદ્ધિના પ્રારંભિક તબક્કામાં અનામોર્ફસ-થી-સ્ફટિકાકાર પરિવર્તન દર્શાવે છે. વિપરીત રીતે, Sb-ટર્મિનેટેડ સપાટીઓ પર ફિલ્મો સીધી જ સ્ફટિકાકાર અવસ્થામાં જમા થાય છે. વધુ પ્રયોગશીલ કાર્યમાં Si(111) 1x1 સપાટી પર GeTe ફિલ્મોમાં અનામોર્ફસ-થી-સ્ફટિકાકાર પરિવર્તન માટે જરૂરી ક્રિટિકલ થિકનેસ પર સબસ્ટ્રેટ તાપમાનના પ્રભાવનું અન્વેષણ કરવામાં આવ્યું. ARHEED અને X-રે ડિફ્રેક્શન (XRD) ફી-સ્કેન્સ દ્વારા રોટેશનલ ડોમેઇનના વિશ્લેષણ દર્શાવે છે કે Sb-ટર્મિનેટેડ સપાટીઓ પર ટ્વીન ડોમેઇનનું દમન થયેલું છે, જ્યારે 7x7 પુનઃરચનાકૃત સપાટીઓ પર મુડેલા રોટેશનલ ડોમેઇન દેખાય છે. GeTe થિન ફિલ્મોનું એક વૃદ્ધિ સિરિઝ પણ રજૂ કરવામાં આવ્યું, જેમાં જાડાઈ 2 nm થી 80 nm સુધી ફેલાયેલ છે, જે દર્શાવે છે કે GeTeમાં જાડાઈ પર આધારિત રચનાત્મક ફેરફારો કન્ફાઇનમેન્ટ દ્વારા આકારમાં ફેરફારનો પરિણામ આપે છે. બીજા મટિરિયલ તરીકે SnTeનું અન્વેષણ કરવામાં આવ્યું. Si(111) સપાટીઓ પર તેની વૃદ્ધિની તુલના કરવામાં આવી હતી, જેમાં RHEED અને XRDનો ઉપયોગ કરીને Si(111) 1x1 સપાટી પર ફિલ્મોમાં જાડાઈ આધારિત જાળીબંધણની ફેરફારોનું વિશ્લેષણ કરવામાં આવ્યું. છેલ્લે, SnSeના Si(111) 1x1, 7x7 પુનઃરચનાકૃત અને Sb-ટર્મિનેટેડ સપાટીઓ પર એપિટેક્ષિયલ વૃદ્ધિનું અધ્યયન કરવામાં આવ્યું. તમામ ત્રણ સપાટીઓ પર અત્યંત ટેક્સ્ચર્ડ SnSe ફિલ્મો (100) દિશામાં વૃદ્ધિ પામે છે. વિગતવાર XRD અને રિસિપ્રોકલ સ્પેસ મેપિંગ વિશ્લેષણ દર્શાવે છે કે અલ્ટ્રા-થિન SnSe ફિલ્મો જાળીમાં વિકાર દર્શાવે છે. ખાસ કરીને, SnSe ફિલ્મો 5 nmથી ઓછી જાડાઇ પર ઓર્થોરોમ્બિક Pnma ફેઝમાંથી ઊંચા-સમમિતી ધરાવતી Cmcm ફેઝમાં પરિવર્તન દર્શાવે છે, જે રામન સ્પેક્ટ્રોસ્કોપી દ્વારા જોઈ શકાય છે. આ શોધો થિન ફિલ્મના અસરોને સમજવામાં વધારો આપે છે, જે ઇલેક્ટ્રોનિક અને થર્મોએલેક્ટ્રિક ઉપકરણોમાં તેમના ઉપયોગને માટે મૂલ્યવાન પરિચિતો પ્રદાન કરે છે.

Declaration of originality

I certify that the work in this thesis has not previously been submitted for a degree nor has it been submitted as part of requirements for a degree except as fully acknowledged within the text.

I also certify that the thesis has been written by me. Any help that I have received in my research work and the preparation of the thesis itself has been acknowledged. In addition, I certify that all information sources and literature used are indicated in the thesis.

Hetal Kanjibhai Vaishnav
Jülich, 10th July 2025

Contents

1 Motivation 1
1.1 Metavalent bonding 3
1.2 Scope of thesis: 6
2 Fundamentals of Thin Films and Molecular Beam Epitaxy 7
2.1 Epitaxy in General 7
2.1.1 Lattice Misfit and Domain Match Epitaxy 8
2.1.2 Formation of Epitaxial Domains 10
2.2 Fundamentals of Molecular Beam Epitaxy 12
2.2.1 Nucleation and Molecular Interaction on Surfaces 13
2.2.2 Thin film growth modes 15
2.3 Molecular Beam Equipment setup 16
2.4 Helmholtz Nano Facility (HNF) - Nanocluster Facility and Module 5 17
2.5 Choice of Substrate and Sample holder: 20
2.6 Wet Chemical Wafer Cleaning 22
3 Experimental Setup 25
3.1 Reflection High-Energy Electron Diffraction 25
3.1.1 Fundamentals of RHEED 25
3.1.2 RHEED Pattern 28
3.1.3 Kikuchi Lines 30
3.1.4 RHEED Oscillations 31
3.2 Azimuthal RHEED 35
3.3 X-ray Diffraction 37
3.4 X-ray reflectometry (XRR) 38
3.5 Scanning Electron Microscopy 39
4 Surface Termination of Silicon 41
4.1 Si (111)-1x1-H 41
4.2 Si (111)-1x1 surface 43
4.3 Si (111)-7x7 reconstruction 44
4.4 Si (111)-(√3×√3)R30°-Sb surface 46
4.5 Si-1x1 Te 50
5 Thin film growth of IV-VI mono chalcogenides 51
5.1 GeTe 52

5.1.1 Crystal structure of GeTe : ... 52
5.1.2 Growth of GeTe: ... 53
5.1.3 Analysis of GeTe growth ... 55
5.2 SnTe: ... 62
5.2.1 Crystal structure of SnTe : ... 62
5.2.2 Growth of SnTe: ... 63
5.2.3 Analysis of SnTe growth ... 64
5.3 SnSe ... 70
5.3.1 Epitaxial growth of SnSe ... 72
5.3.2 Analysis of SnSe growth ... 73
6 Thin film effects ... 82
6.1 Impact of substrate temperature on the critical thickness of blackout in GeTe films ... 82
6.2 Structural changes through confinement in GeTe. ... 85
6.3 SnSe Phase transition from Pnma towards Cmcm in ultra-thin film thicknesses ... 90
7 Conclusion and Outlook ... 97
Appendix ... 99
Bibliography ... 102
Acknowledgements ... 110

1 Motivation

The exponential growth in global data volumes, driven by the proliferation of mobile electronics and artificial intelligence applications, poses significant challenges to existing memory technologies. Today's computing systems rely heavily on the von Neumann architecture, which separates memory from processing units. This architecture includes various memory types that form a complex hierarchy based on speed, volatility, and storage capacity. As shown in Figure 1.1, this hierarchy includes fast but volatile memory types such as static random access memory (SRAM) and dynamic random access memory (DRAM), as well as slower but non-volatile storage options like solid-state drives (SSDs) and hard disk drives (HDDs). While SRAM and DRAM offer high-speed operation, their volatility and limited storage capabilities necessitate frequent data transfers between memory types, creating performance bottlenecks and increasing power consumption.[1]

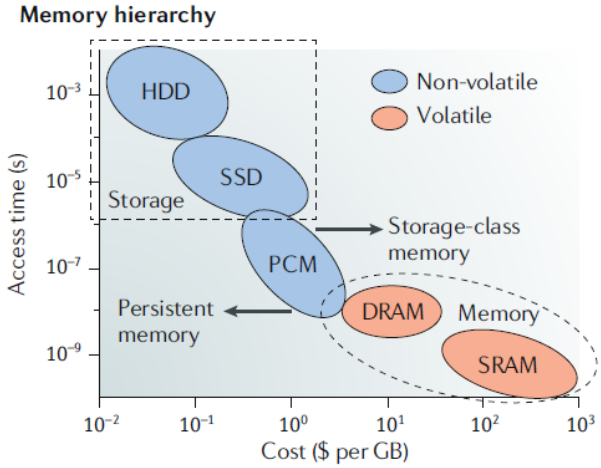

Figure 1.1: Memory hierarchy of current computing devices, illustrating the distinction between non-volatile storage (hard disk drives and solid-state drives) and volatile memory (dynamic random access memory and static RAM). Phase-change materials are highlighted for their advantageous combination of speed, non-volatility, storage density, and moderate fabrication costs.[1]

Phase-change materials (PCMs) represent a breakthrough solution to these challenges, offering a unique combination of speed, non-volatility, and scalability. PCMs can store data by exploiting the substantial contrast in electrical resistance between their amorphous and crystalline states. The fast, reversible switching between these states makes PCMs particularly suitable for non-volatile memory applications.

This switching mechanism involves applying a controlled voltage pulse that induces crystallization (SET) or amorphization (RESET) through localized Joule heating (PCM), as illustrated in the Figure 1.2. The amorphous phase exhibits high electrical resistance (logic "0"), while the crystalline phase demonstrates low resistance (logic "1").

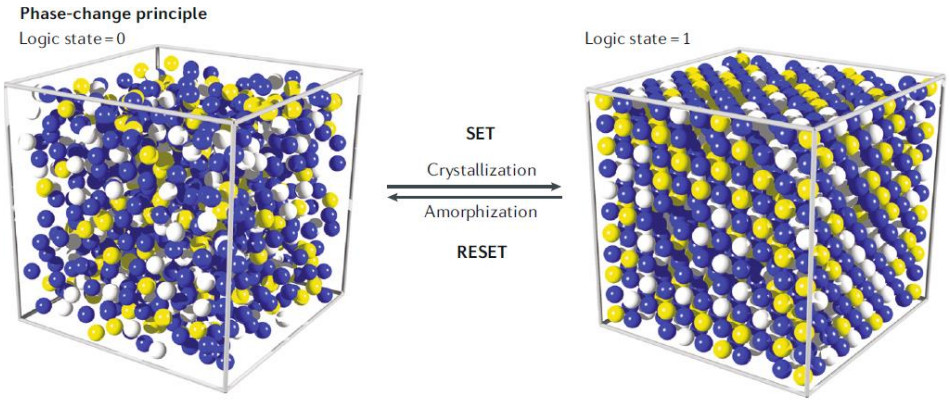

Figure 1.2: The distinct electrical resistance contrast between the amorphous and crystalline phases of phase-change materials (PCMs) designates the two logic states, 0 and 1. The swift and reversible transitions between these states are facilitated by the processes of crystallization (SET/write) and amorphization (RESET/erase).[1]

In recent years, PCM-based random-access memories (PRAMs) have gained considerable attention due to their potential to fill the performance gap between DRAM and SSD. These materials promise not only faster and more reliable data storage but also the possibility of combining processing and memory in the same physical unit, thereby simplifying the memory hierarchy and reducing data traffic (PCM). For example, 3D XPoint technology integrates PCMs into storage-class memory (SCM) architectures, offering a balance between speed, non-volatility, and fabrication costs.[1]

One of the most well-known classes of PCMs is based on chalcogenides, compounds that contain sulfur, selenium, or tellurium. Most PCMs are compounds of Ge, Sb and Te (GST) along the pseudobinary line between GeTe and Sb_2Te_3 and AgInSbTe-combinations, as illustrated in Figure 1.3. These materials exhibit pronounced property contrasts between their states and rapid crystallization kinetics, making them highly efficient for data processing and storage. The ability of PCMs to switch phases is influenced not only by their bonding characteristics but also by nanoscale confinement. Thin films and nanoparticles of PCMs often exhibit altered crystallization temperatures and enhanced stability in their amorphous phases. [1–3] This nanoscale effect is critical in optimizing the performance of PCMs for memory applications. A critical factor in the functionality of PCMs is the nature of their bonding mechanism. [4] Traditionally, the bonding in PCMs has been described using terms such as resonant bonding, but recent studies, propose a novel concept known as metavalent bonding (MVB).[5, 6] This new bonding model helps explain the peculiar combination of properties exhibited by phase change materials.[5]

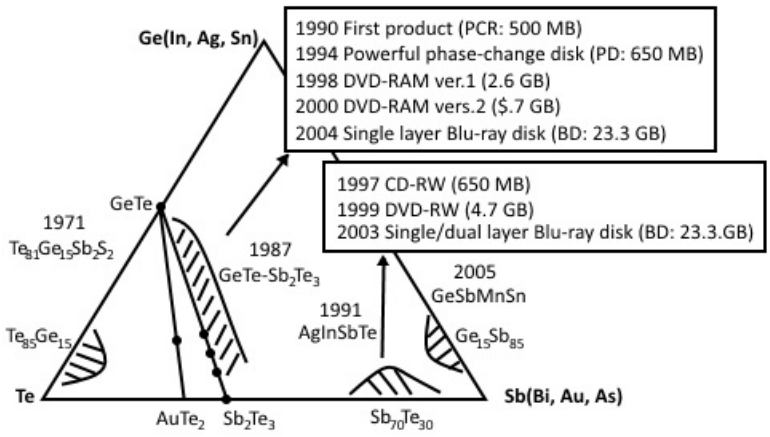

Figure 1.3: Ternary phase diagram of Ge, Sb and Te. It gives an overview of the evolution of PCM based optical storage applications.[2]

1.1 Metavalent bonding

Chemical bonding has traditionally been categorized into distinct types, including covalent, ionic, and metallic bonds. However, recent research has identified a novel type of bonding known as metavalent bonding (MVB), which does not fit neatly into these conventional categories. MVB exhibits a unique combination of characteristics distinctively different from both metallic and covalent bonds.[5]

The term "metavalent" is derived from the Greek prefix "meta-" (meaning "beyond" or "adjacent to") and the Latin word "valentia," which refers to "strength" or "capacity." [5] Thus, "metavalent" implies a bonding mechanism that transcends traditional bonds such as covalent or metallic bonding. Importantly, metavalent bonding is not merely a hybrid of metallic and covalent bonds; it represents a fundamentally different type of bonding that is distinct from both. Its unique characteristics have been observed in several IV-chalcogenides compounds, such as GeTe, PbTe, and SnTe, which are significant for various functional applications, including thermoelectrics, phase-change memory (PCM), and nanoelectronics.

Characteristics of Metavalent Bonding:

The following table highlights of the properties as fingerprint of different bonding in materials.

Bonding properties identifier	Ionic (e.g., NaCl, MgO)	Covalent (e.g., Si, GaAs)	Metavalent (incipient metals, e.g., GeTe, PbTe)	Metallic (e.g., Cu, NiAl)
Electronic conductivity (electrical identifier)	Very low ($<10^{-8}$ S cm^{-1})	Low to moderate (10^{-8}–10^{2} S cm^{-1})	Moderate (10^{1}–10^{4} S cm^{-1})	High ($>10^{5}$ S cm^{-1})
Coordination number) (structural identifier)	4 (ZnS), 6 (NaCl),8 (CsCl)	8-*N* rule typically satisfied	8-*N* rule not satisfied	8 (bcc), 12 (hcp/fcc)
Optical dielectric constant ε_∞ (optical identifier)	Low (≈2–3)	Moderate (≈5–15)	High (>15)	Not applicable to the metallic state
Born effective charges *Z** (chemical bond polarizability)	Low (1–2)	Moderate (2–3)	High (4–6)	Vanishes (0)
Mode specific Grüneisen parameters (anharmonicity)	Moderate (2–3)	Low (0–2)	High (>3)	Low (0–2)

Table 1.1: Property-based "fingerprints" used to define bonding characteristics in inorganic materials. For metavalent solids, five specific identifiers must be present in a material. For example, while both NaCl and PbTe exhibit the same structural identifier, NaCl demonstrates significantly lower electronic conductivity.[5]

Electron Sharing and Moderate Delocalization: In MVB, electrons are partially shared between atoms without forming full covalent bonds. The sharing of a single electron between neighboring atoms results in intermediate conductivity, with electrical properties place MVB materials between conventional metals and semiconductors. This electron-sharing feature allows for partial delocalization, unlike the fully delocalized electron sea in metallic bonds, but provides flexibility absent in purely covalent or ionic systems. [7]

Unique Structural and Physical Properties: MVB is notably present in materials with octahedral-like coordination and a tendency toward phase-change behavior. For instance, the GeTe and Sb_2Te_3 compounds can transition between amorphous and crystalline phases, a property is leveraged in data storage. These crystalline compounds typically exhibit high Grüneisen parameters for transverse optical modes, indicating their inherent anharmonicity, which supports low thermal conductivity, a valuable feature for thermoelectric materials.[8]

Bond-Rupture Behavior: A distinguishing feature of MVB is its unusual bond-rupture mechanism, which is often observed through atom probe tomography. When subjected to high-field evaporation,

MVB compounds exhibit a high probability of multiple fragment releases, a behavior that underscores the collective nature of their bonds. This behavior differs significantly from conventional materials, where bond rupture typically produces single fragments. For example, crystalline phase change materials like GeTe and $Ge_2Sb_2Te_5$, over 70% of ions come from multiple events, suggesting a unique bond-breaking process that is not seen in materials like Si, GeSe, or metals.[9]

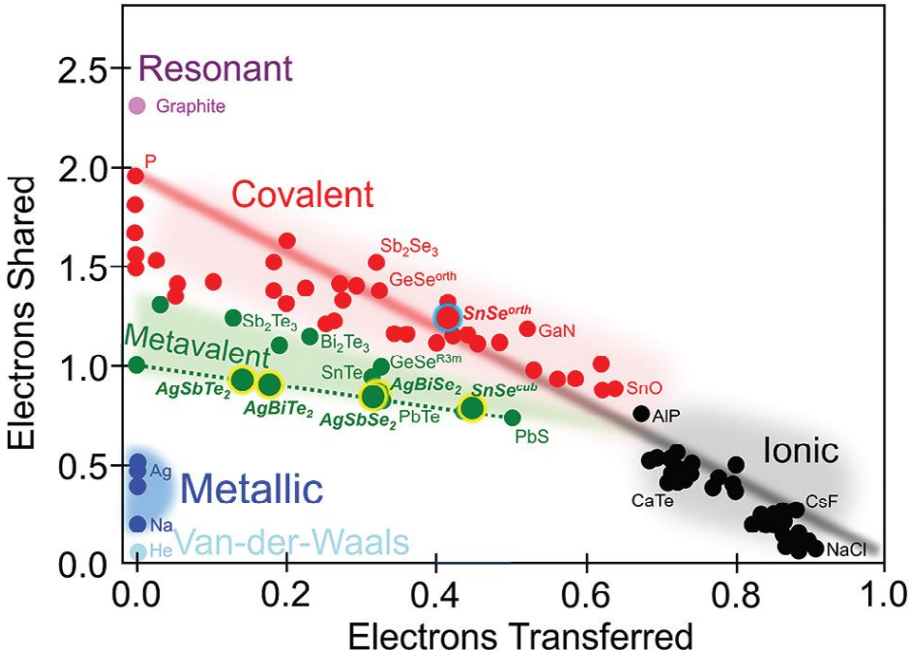

Figure 1.4: A 2D map of electronic interactions and bonding in materials. The amount of electrons transferred (x-axis) and shared between neighboring basins (y-axis). [10]

Apart from these key figures, a materials map has been developed to distinguish metavalent bonding from traditional bonding types—ionic, covalent, and metallic.[10] This map shown in Figure 1.4, is based on quantum mechanical calculations and uses two main factors: the number of electrons transferred (indicating ionic character) and the number of electrons shared (indicating covalent or delocalized bonding). The materials map reveals distinct regions that correlate with specific bonding mechanisms, effectively visualizing how materials employing MVB occupy a unique space on this map, intermediate to other bonding types. Traditional ionic compounds like NaCl cluster separately from covalent materials such as silicon. Notably, metavalent materials, including GeTe and PbTe, are positioned in an intermediate region, illustrating their unique bonding characteristics defined by partial electron sharing and limited charge transfer. Additionally, the map serves as a predictive tool, linking the positioning of materials with properties such as the optical dielectric constant and Born effective charge. This allows researchers to forecast materials properties based on bonding classifications. Overall, the materials map provides a valuable framework for designing advanced materials, particularly for applications in thermoelectrics, phase-change memory, and photonics, by enabling researchers to identify promising compounds through insights into bonding trends and their associated properties.[5]

Within this work, the epitaxial growth of GeTe, SnTe, and SnSe is conducted to investigate the bonding mechanisms and properties of these materials, with a particular focus on ultra-thin films.

1.2 Scope of thesis:

This thesis primarily addresses the deposition and characterization of epitaxial films of IV-VI monochalcogenides, such as GeTe, SnTe, and SnSe, using molecular beam epitaxy, with a focus on the effects of ultra-thin films. Chapter 2 provides an overview of thin films and epitaxial growth. While the dissertation examines the growth of different material systems, the foundational concepts of nucleation, growth, and the impact of lattice mismatch between the substrate and the deposited layer remain consistent across systems. This chapter focuses on key parameters that control the growth process and can serve as tools for the crystal grower to manipulate the properties of epilayers. Much of the discussion centers on the Helmholtz Nano Facility (HNF) – Nanocluster Facility at Forschungszentrum Jülich, specifically Module 5, which was used in this research and includes an MBE chamber dedicated to the growth of phase-change materials. Chapter 3 provides a brief overview of the various *in-situ* and *ex-situ* analytical techniques employed to optimize the growth conditions of IV-VI monochalcogenide thin films and their characterization. Silicon serves as the primary substrate for this study, and therefore Chapter 4 delves into the critical aspect of silicon surface reconstruction, exploring the different silicon surfaces investigated. Chapters 5 and 6 present the main experimental findings of this work. Chapter 5 discusses the growth and characterization of GeTe, SnTe, and SnSe on Si(111) surfaces, including the 1x1 surface, 7x7 reconstruction, and Sb termination. Film structure analysis is based on RHEED, ARHEED, and XRD data, with discussions on how surface modifications, elemental composition, substrate temperature, and surface properties influence film growth and impact the resulting film characteristics. Chapter 6 summarizes the effects of thin films in GeTe, SnTe, and SnSe, focusing on how reduced thickness leads to changes in crystal structure and variations in in-plane and out-of-plane lattice constants due to confinement effects.

2 Fundamentals of Thin Films and Molecular Beam Epitaxy

The properties of a thin film of a given material depend on its real structure, which is determined by the deposition technique used and the process parameters utilized. Understanding these fundamentals is crucial for this work.

Sections 2.1 discusses the formation of epitaxial thin films, starting with nucleation, progressing through coalescence, and continuing with film growth. Each stage can be influenced by deposition parameters and the substrate surface.

Sections 2.2 introduces the fundamentals of the Molecular Beam Epitaxy (MBE) technique, the general experimental implementation is provided in Section 2.3. Section 2.4 describes in detail the MBE system, particularly the Module-5 facility at HNF Nano cluster, where the experiments for this thesis were conducted.

Sections 2.5 and 2.6 focus on the treatment of the substrate and substrate holder before deposition and detail the specific processes involved. For more detailed information on these techniques, the reader is referred to standard textbooks on the subject [11, 12].

2.1 Epitaxy in General

Epitaxy is a process of growing crystal layers with precise orientation on a crystalline substrate or seed layer. The deposited crystalline film is called an epitaxial film or epitaxial layer if it is aligned with respect to the substrate . The term "epitaxy" is derived from the French word "épitaxie," which has Greek roots: "epi" meaning "above" and "taxis" meaning "order" or "manner." The word was first used in 1928 by French mineralogist L. Royer in his work: “Recherches expérimentales sur l’épitaxie ou orientation mutuelle de cristaux d’espèces différentes”[13, 14]. Epitaxial growth can be categorized into two primary types: homoepitaxy and heteroepitaxy. In homoepitaxy, the deposited layer is made of the same material as the substrate, and it has the same crystal structure and orientation. This process is commonly used to improve the quality of a single crystal by growing another layer with the same crystal structure on top of it. The most important example of homoepitaxy comes from silicon technology, where the (001)-oriented wafers are usually refined by an epitaxial Si deposition, whose quality is superior to that of the original substrate surface.

In heteroepitaxy, the deposited layer is made of a different material from the substrate but growns in a compatible crystal structure, allowing it to align with the substrate's lattice. Heteroepitaxy is often used to introduce new materials with specific properties into a substrate. Homoepitaxy has no strained interfacial bonds in ideal conditions due to identical lattice parameters. Conversely, in heteroepitaxial growth, the film-substrate interface experiences residual strain. This strain arises from the lattice mismatch and plays a crucial role in determining the films' growth characteristics, morphology, and chemical and physical properties. Consequently, comprehending the lattice mismatch is of utmost importance for controlling the quality and properties of the films. To determine the probability of epitaxial growth, an important parameter is the lattice misfit ε_m at the interface which can be calculated using the following equation;

$$\varepsilon_m(\%) = \left(\frac{d_f - d_s}{d_s}\right) \times 100$$

Where d_f and d_s are lattice spacing parameters in the in-plane directions between the film and the substrate, respectively.

Based on the percent of misfit, epitaxial growth process can be explained under Lattice Match Epitaxy (LME) and Domain Match Epitaxy (DME).[15]

2.1.1 Lattice Misfit and Domain Match Epitaxy

In the context of thin film growth, the conventional method of lattice matching epitaxy (LME) requires relatively small lattice misfits in the range of ε_m< 7-8%. In LME, the growth occurs with bond formation between corresponding atoms across the film-substrate interface. In the case of a difference in the lattice constants of film and substrate, lattice strain in the film is induced, which increases with film thickness up to the critical thickness. In such strained films, atoms experience dual forces:

- The first force arises from interactions with neighboring atoms in the film material, guiding them toward their optimal positions in alignment with the crystalline structure.
- The second force applied by the atoms in the substrate simultaneously compelling them to conform to their ideal lattice configurations.

Depending on the bonding at the interface between grown film and substrate, the thin films can grow pseudomorphically up to a "critical thickness", above which it becomes energetically favorable for the film to contain dislocations. Notably, the critical thickness exhibits an inverse correlation with the lattice misfit; a larger lattice misfit prompts dislocation-induced relaxation at a smaller film thickness. [16] One of the well-known example is Ge growth on Si(111) substrate.[17]

For the larger lattice mismatch of more than 8%, the conventional lattice-matching epitaxy is unable to accommodate the strain to establish an epitaxial growth of the thin film. However, epitaxial growth has also been observed in this kind of system, such as ZnO(0001)/Al_2O_3(0001) [18] and TiN(100)/Si(100) [19]. Domain match epitaxy (DME), a unique approach to epitaxy, has been introduced to understand these larger misfits. [15]. This technique involves aligning lattice planes

between the film and substrate with similar crystal symmetry. The matching of lattice planes could be different in different directions of the film–substrate interface. In contrast, LME requires matching the same planes between the film and substrate. In DME, the initial misfit strain could be relaxed by matching the *m* numbers of planes of the film with the *n* numbers of the substrate lattice planes. This matching of integral multiples of lattice planes leaves a residual strain of ε_r given by;

$$\varepsilon_r = \left(\frac{m}{n}\right) \cdot \left(\frac{d_f}{d_s}\right) - 1$$

where, *m* and *n* are simple integers. In the case of a perfect lattice matching $(md_f = nd_s)$, the residual strain ε_r is zero.[16]

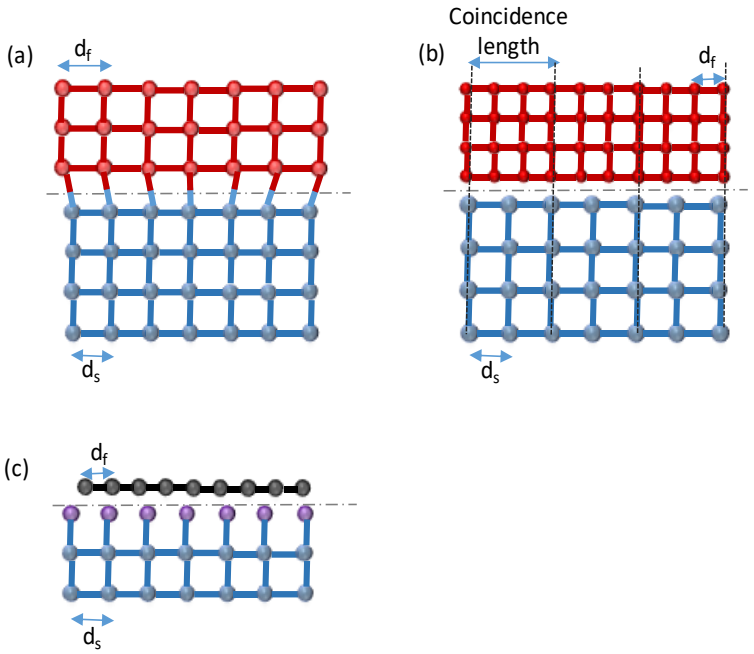

Figure 2.1: (a) Lattice match (b) coincidence domain match (c) van der Waals epitaxy

For example, TiN or MgO films exhibit epitaxial growth with a lattice misfit of approximately 25%, achieved through aligning four planes of the film with three planes of the substrate. In cases where the misfit falls between integral multiples, any remaining misfit beyond the integral matching is managed through domain variation. In this process, two domains alternate with a specific frequency, ultimately achieving a zero misfit, for more information refer [15].

The lattice mismatch plays an important role in classical epitaxy where 3D bonded materials are used as substrates and also thin film consist 3D bonded system. The forced combination of both the 3D materials, results in a strong chemical coupling between the thin film and substrate owing to the covalent, ionic or metallic interactions at the interface as in the case of, 3D chalcogenide like GeTe, SnTe grown on Si substrates. In van der Waals (vdW) epitaxy, where 2D bonded materials are grown on 2D bonded substrates, strong chemical bonding is not possible. Instead, the epitaxy process is governed by vdW interactions, which are typically an order of magnitude weaker than covalent interactions. This weak interaction at interface increases the possibilities of achieving a fully relaxed

film from beginning of the film growth.[13, 20] Now, in the case of a 2D bonded thin film grown over a 3D bonded substrate also known as quasi- vdW epitaxy, the interface interactions are not fully understood for this type of epitaxy. However, it is observed that the surface of the substrate plays a crucial role in in-plane epitaxial alignments. A detailed study on Sb_2Te_3 growth over Si(111) reconstructed surfaces was conducted to understand the growth mechanisms in 2D thin films on 3D substrate in [20]. In this, the quasi-vdW epitaxy system is found to generate rotational domains, whose presence is explained by the formation of coincident lattices with the underlying dangling bonds of the Si(111) substrate's surface in order to reduce the lattice mismatch. This clearly demonstrates the crucial impact of the starting surface's symmetry and orientation on the in-plane domains of 2D crystals in quasi-vdW heteroepitaxy. Hence, it is crucial to understand the formation of rotation domains in heteroepitaxy, which is explained in section 2.1.2.

2.1.2 Formation of Epitaxial Domains

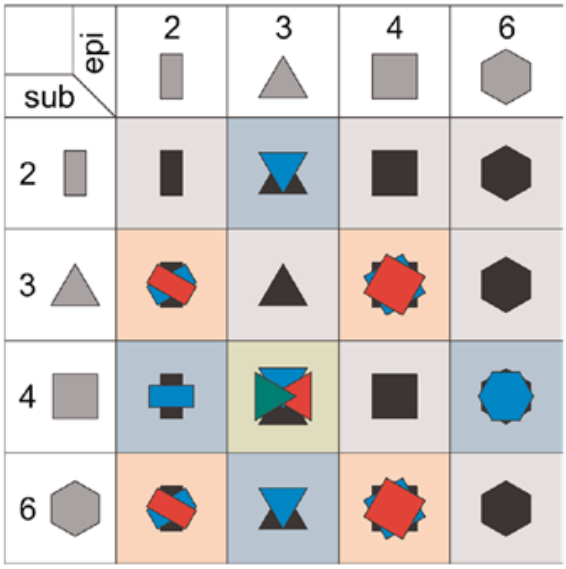

Figure 2.2: Schematic graphical representation of the minimum number of rotational domains formed in epitaxy; columns belong to the same symmetry of the thin film, and rows belong to the substrate. [21]

Rotation domains in the thin film are domains with the same crystallographic direction along the growth direction but different in-plane azimuthal orientation. The presence of rotational domains introduces large-angle grain boundaries in thin films, affecting properties such as surface roughness, strain distribution, impurity distribution and carrier mobility. The formation of epitaxial domains in heteroepitaxy depends fundamentally on the relation of the crystal symmetries; especially rotational symmetries of the epilayer and substrate. Grundmann et al. (2010) described using group theory the possible formation of domains for all combinations of the two-dimensional (2D) point symmetries of substrate and thin film, including cases of aligned and misaligned symmetry directions. The substrate surface two-dimensional (2D) point symmetry generally belongs to one of the ten 2D point groups. These are 1, m, 2, 2mm, 3, 3m, 4, 4mm, 6 and 6mm. In the case the substrate and thin film's

symmetries are aligned, the minimum formation of domains in the grown film can be predicted from Figure 2.2. [21]

In the case of substrate and thin film having the same geometric symmetry; the minimum number of domains would be one. For example hexagonal ZnO(0001) on Al_2O_3(0001) shows the expected single domain growth. By changing the substrate to Si(001) which consist of 4 fold symmetry growth of hexagonal ZnO(0001) exhibits two domains in the thin film, which are rotated by 30° to each other. This can be explained by Figure 2.2 The growth of Cubic SnTe(001) on Si(111) exhibits the presence of 3 rotational domains based on four fold symmetry over three fold symmetry. Each are rotated to 30° in plane. The detailed study of rotational domains in thin film based on this theory is demonstrated in chapter 5.

In the case where the mirror symmetry plans of the substrate and thin film are misaligned, the number of rotational domains increases in the film. The table below gives the details about the possible number of rotational domain in mirror planes for the aligned and misaligned cases.

G_S/G_E	**1**	**m**	**2**	**2mm**	**3**	**3m**	**4**	**4mm**	**6**	**6mm**
1	1	1	1	1	1	1	1	1	1	1
m	2	1|2	2	1|2	2	1|2	2	1|2	2	1|2
2	2	2	1	1	2	2	1	1	1	1
2mm	4	2|4	2	1|2	4	2|4	2	1|2	2	1|2
3	3	3	3	3	1	1	3	3	1	1
3m	6	3|6	6	3|6	2	1|2	6	3|6	2	1|2
4	4	4	2	2	4	4	1	1	2	2
4mm	8	4|8	4	2|4	8	4|8	2	1|2	4	2|4
6	6	6	3	3	2	2	3	3	1	1
6mm	12	6|12	6	3|6	4	2|4	6	3|6	2	1|2

Table 2.1: The number of rotational (or mirror) domains is specified for all 2D point groups of the substrate (GS) arranged in rows and the thinfilm (GE) in columns. In cases where two numbers are provided (x|y), the first number signifies the count of domains when mirror symmetry planes of the substrate and epilayer align and second number represents count of domains in misalign case. [21].

The additional epitaxial domains can be present in another case such as, when substrate surface has higher symmetry than the bulk, and nucleation process is only influenced by the top surface. When substrate surface has non equal step height to translational vector of the lattice. For more details refer to[21].

In this thesis, we have explained two epitaxy types: one 3D thin film on 3D substrate and 2D thin films on 3D substrates and the impact of substrate surface reconstructions on rotational domains in thin film in Chapter 5 and 6. Now let's focus on the how the epitaxial thin film deposition works and molecules interacts on substrates surface to understand the growth mechanism.

2.2 Fundamentals of Molecular Beam Epitaxy

Numerous methods are available for depositing epitaxial films such as Liquid Phase Epitaxy (LPE), Atomic Layer Deposition (ALD), Chemical Vapor Deposition (CVD), Metal Organic Chemical Vapor Deposition (MOCVD), Metal Organic Molecular Beam Epitaxy (MOMBE), Metalorganic Vapour-Phase Epitaxy (MOVPE), Pulsed Laser Deposition (PLD), and Molecular Beam Epitaxy (MBE) being among the most commonly employed techniques, as documented in [22]. For all the thin film deposition, in this work the MBE technique was employed which is explained in this section. All the IV- VI chalcogenide materials discussed in this thesis were grown by MBE, and this section discusses the details of this important growth technique.

Molecular Beam Epitaxy (MBE) is an epitaxial growth technique used for depositing thin films of single crystals, developed by J.R. Arthur and A.Y. Cho in the late 1960s at Bell Laboratories. The inception of MBE closely coincides with the developmental trajectory of the semiconductor industry. MBE has wide-ranging applications in the growth of diverse semiconductor materials, encompassing III–V, II–IV, IV–VI, IV–IV, and oxide semiconductors.[23] MBE is a process in which a thin single crystal layer is deposited on a single crystal substrate using atomic or molecular beams generated in Knudsen cells contained in an ultra-high vacuum chamber. The deposition rate is generally less than 1Å per second, which is an important characteristic of molecular beam epitaxy that permits the films to grow epitaxially. Such deposition rates demand ultra-higher vacuum conditions, pressure ranging from 10^{-9} to 10^{-12} mbar. The term "molecular beam" means that no interaction results between the evaporated atoms with each other or vacuum chamber gases until they get to the wafer, owing to the long mean free paths of the atoms. Deposition of thin films via the MBE process comprises three key stages: the generation of the molecular beams, the transport of the molecular beam from the source to the substrate, the interaction between the molecular beam and the substrate, and the growth process that takes place on the substrate. This section provides a brief overview of the MBE environment and growth control.

1) Generation of molecular beams

The source beams can be created in a number of ways, including (1) melting and evaporation of solids or liquids contained in crucibles (2) solid sublimation from a crucible, (3) ion beam bombardment, and (4) cracking various chemical species. The molecular beam is generated by ultrapure solid materials housed in effusion cells, the flux from these cells is determined solely by the vapor pressure of the material, a parameter easily controlled by the crucible temperature. Normal effusion cells with crucibles made of materials like hBN, Al2O3, graphite, W, or Ta, and filament radiation heating are suitable for materials with vapor pressures attainable in a wide temperature rage, 100°C – 2000°C. For the metal that melt at evaporation temperatures, such as Al, In, Bi, and Ge, double-walled crucibles can be used to minimize the risk of crucible cracking and to prevent contamination of the effusion cell filament.

Certain elements like Se, Te, and Sb evaporate as cluster molecules, such as octamers and tetramers [24]. Special cracker cells are used to break these tetramers into dimers to enhance reactivity and stoichiometric control. Electron beam evaporators are generally employed to achieve higher temperatures beyond 2000°C for evaporating materials. Typically, effusion cells are equipped with computer-controlled mechanical shutters for better functionality control.

2) Transmission of molecular beams

The directional flow of the beam in an ultra-high vacuum environment often leads to the occurrence of beam crossing, especially when multiple beams are employed in compound growth processes. This effect is notably pronounced in equipment utilized for chemical vapor deposition (CVD), where molecular collisions and chemical reactions frequently take place during cross-transport. As a result, the reactivity of atoms or ions decreases upon reaching the substrate, resulting in a reduction in the quality of the resulting film. In contrast, molecular beam epitaxy (MBE) equipment benefits from the relatively large average free path of molecules and atoms, reducing the probability of collisions among molecules or atoms in the cross molecular beam. As a result, the molecular beam remains highly active during deposition, aiding in the preservation of atomic or ionic activity. This is advantageous for lowering the temperature necessary for epitaxial growth on the substrates and enhancing crystal quality.

3) The interaction between molecular beam and substrate, and the growth process on substrate. It is explained further in section 2.1.1 and 2.1.2.

2.2.1 Nucleation and Molecular Interaction on Surfaces

During the deposition process, molecules and/or atoms undergo a series of interactions with the surface. These includes the deposition of atoms on the substrate, the re-evaporation from the substrate, the diffusion of atoms on the surface of the substrate, and the interdiffusion on the crystal plane.

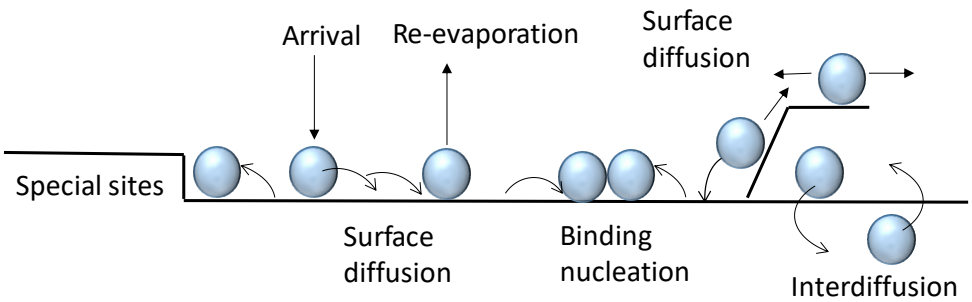

Figure 2.3: Surface processes of incident atoms during epitaxial growth. [25]

Figure 2.3 represents the arrival of atoms or molecules on the substrate surface and the interactions that occur on it. One of the major factors which directly influences the molecular interaction to the substrate is the substrate surface temperature. If the temperature of the substrate is too high, incoming atoms can directly re-evaporate. The atom cannot re-evaporate directly when the

temperature is lower than a specific substrate temperature. Still, the atom can move parallel to the substrate surface and then re-evaporate again or combine with the substrate to get incorporated. If surface diffusion is fast enough, a randomly deposited adatom will diffuse to the energetically most favorable places like steps and kinks. Such locations provide preferred nucleation sites for incoming atoms. Once an atom has nucleated, other atoms can bind to it to extend the deposited layer, or desorb away.

Nucleation sites are not uniformly distributed across the substrate surface. They often appear in areas with favorable surface conditions, such as defects, step edges, or areas with a specific crystallographic orientation. It also depends on diffusion energy and surface energy. High-energy sites may be more favorable for nucleation because they can facilitate stronger adhesion, for example, consider an unsaturated silicon surface having dangling bonds that serve as binding sites for the initial formation of nuclei.[26] The steps on the surface of the substrate are another common initial point. During the manufacturing of a silicon wafer, atomic steps are created across the entire wafer when the cutting plane deviates slightly from being parallel to the crystal planes. Atoms with sufficient diffusion energy can move across these steps, or get incorporated at step edges. By definition a thin film has a very large surface-to-volume ratio. Surface energy controls the nucleation as well as on the heterogeneous epitaxial growth processes. The surface energy determines whether or not one material wets another and forms a uniform adherent layer in the case of heterogeneous epitaxial growth. A material with a very low surface energy will tend to wet a material with a higher surface energy so that epitaxial growth is possible. On the other hand, if the material to be deposited has a higher surface energy than the substrate surface, it tends to form clusters ("ball up") on the low-surface-energy substrate.[27] In some cases, the incident atoms tend to diffuse into the substrate, such as in the case of Sb on a Te-terminated Si(111) surface.[28] [29] After the above physical or chemical processes, the atoms that reach the substrate will be incorporated on the surface to form a thin film. Due to the different types of evaporation of atoms, nature of substrates, and process conditions, the formation and structure of the films are different, and the films may be amorphous, polycrystalline, or single crystal.

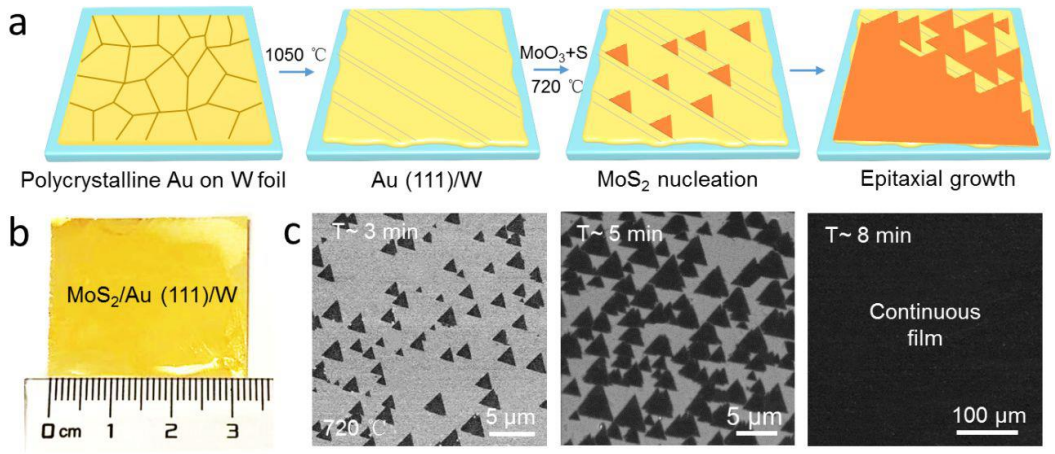

Figure 2.4: (a) Schematic illustration of the Au (111) formation and MoS_2 growth process. (b) Photograph of a MoS_2 monolayer on Au (111)/W foil substrate (c) SEM images revealing the step edges nucleation.[30].

2.2.2 Thin film growth modes

During the epitaxial growth of a film, atoms or molecules can be deposited and arranged on a substrate in different ways, which are referred to as "growth modes". Thin film growth modes are an important aspect of epitaxy. Since they determine the structure, quality, and properties of the resulting thin film. Typically, the growth of thin films can be categorized into three types: (i) Frank-van der Merwe (FM), (ii) Volmer-Weber (VW), and (iii) Stranski-Krastanov (SK). This classification is based on equilibrium considerations regarding the surface energies of the substrate(γ_s), the film(γ_f), and the interface(γ_i). The characteristics of these three growth modes are illustrated in Figure 2.5 [22].

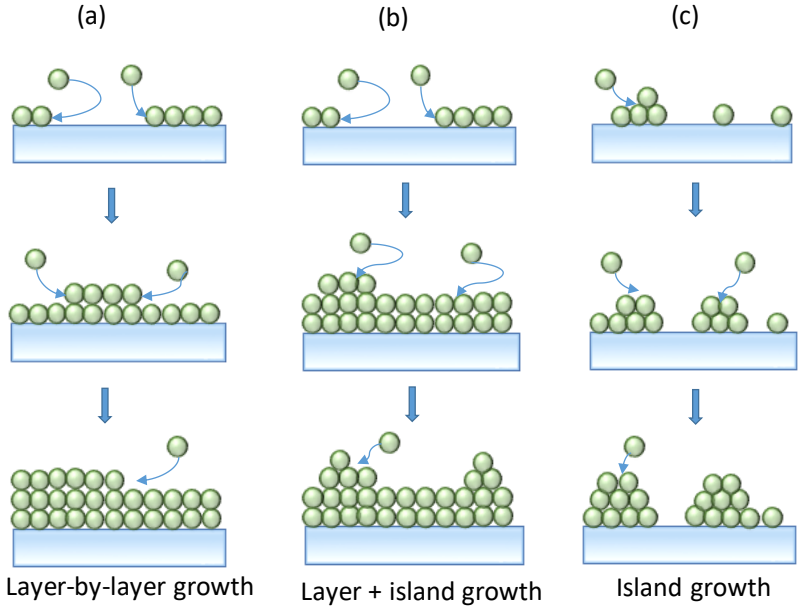

Figure 2.5 illustrates the three growth modes (a) Frank-van der Merwe, 2D layer growth which follows the completion of the layer before the subsequent layer formation; (b) Stranski-Krastanov, initial 2D layer growth, subsequent 3D island formation; (c) Volmer-Weber, 3D island growth from nucleation sites.

Layer-by-layer growth, also known as two-dimensional (2D) or Frank-van der Merwe growth, is anticipated when the combined surface free energy of the epitaxial film and the energy at the film-substrate interface is less than the surface free energy of the substrate ($\gamma_f + \gamma_i \leq \gamma_s$). Nucleation and growth of each successive layer commences only after the completion of the preceding one. This type of growth is commonly observed in systems with well-matched lattices (mismatch smaller than 1.5%) and strong interfacial bond energies. This growth mechanism typically yields a uniform and continuous film.

In contrast, when the sum of the surface free energy of the epitaxial film and the energy at the film-substrate interface surpasses the surface free energy of the substrate ($\gamma_f + \gamma_i > \gamma_s$) it leads to the development of three-dimensional islands, often referred to as three-dimensional (3D) or Volmer-Weber growth. In this growth mode, the initial atoms that reach the substrate condense and serve as nucleation sites. Subsequent atoms that arrive tend to cluster around these nuclei, leading to

three-dimensional growth and the gradual formation of thin films. As a result, thin layers typically possess significant surface roughness because the deposited material does not wet the surface. The surface can regain smoothness upon the formation of a coalescent layer. This mode is observed when the atoms or molecules in the deposit have stronger binding to each other than to the substrate. It is a common occurrence in the growth of heteroepitaxial thin films.

Conversely, the Frank-van der Merwe mode, exhibits contrasting characteristics. Here, the atoms have stronger affinities for the substrate than for each other. As a result, the adsorbed atoms form a uniform monolayer on the surface and proceed to grow layer by layer. The Stranski-Krastanov mode represents a combination of two-dimensional growth followed by three-dimensional island growth. The first few monolayers are deposited in the initial stages through a layer-by-layer process until a specific critical thickness is achieved. Further layer growth becomes less favorable, leading to the development of islands on top of this intermediate layer. The transition to three-dimensional growth occurs as stress accumulates, often due to factors like lattice mismatch.

Epitaxial growth of germanium (Ge) on a silicon (Si) surface exemplifies the Stranski-Krastanov (SK) growth mode for mismatched materials. Initially, Ge grows layer by layer in a two-dimensional (2D) mode, but this transitions to three-dimensional (3D) island growth beyond a critical thickness. This transition is thermodynamically favorable, driven by the energy gained from strain relaxation through elastic deformation, which outweighs the increase in surface energy due to increased surface area [17].

2.3 Molecular Beam Equipment setup

MBE chambers are designed to maintain ultra-high vacuum (UHV) environments during deposition, typically ranging from 10^{-9} to 10^{-11} mbar. The chamber's pumping system integrates a combination of low to high vacuum pumps – venturi, rotary (typically dry), turbo molecular, cryogenic, ion getter, and titanium sublimation pumps. Cryogenic pumps are commonly included in medium- to large-scale MBE systems. A schematic diagram of a typical MBE system is shown in Figure 2.6. Constructed from nonmagnetic stainless steel with full metallic sealing, the chamber features liquid nitrogen-cooled cryoshrouds that act as additional cryopumps, absorbing residual gas molecules and further reducing pressure. To prevent outgassing, all heating elements and effusion cells are water-cooled. Effusion cell filaments are typically linked to PID control loops to stabilize temperature. A computer controls the shutters in front of each effusion cell, allowing precise control of layer thickness down to a single atomic layer. This precise control of fluxes enables accurate regulation of film thickness and material doping, making it particularly suitable for studying thin film effects.[23]

Many MBE chambers also have a movable ion gauge to measure flux from the effusion cells, which are typically arranged in a circle with their focal point on the sample. The substrate holder is equipped with a heater and thermocouple. Several variables within MBE, including source temperature, flux rate, and substrate temperature, can be independently adjusted and monitored to optimize growth quality. The UHV conditions also allow for the use of surface-sensitive electron diffraction-based analytical techniques, such as RHEED, which provide real-time, in-situ information on the growth process. RHEED is further explained in Chapter 3.

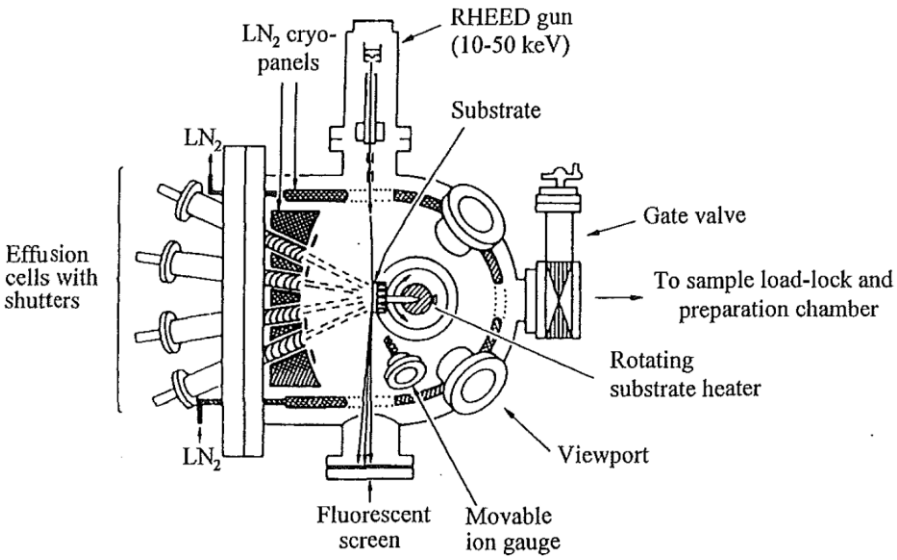

Figure 2.6 schematic diagram of Molecular Beam Epitaxy chamber[31]

2.4 Helmholtz Nano Facility (HNF) - Nanocluster Facility and Module 5

HNF - Nanocluster at Forschungszentrum Jülich is dedicated primarily to thin film growth. The Nanocluster, a collaborative effort among various institutes in Jülich and RWTH Aachen, facilitates seamless collaborations. The Nanocluster currently encompasses multiple deposition chambers, two preparation chambers, five load-locks, featuring a range of deposition techniques and analytic tools from MBE to sputtering, electron beam evaporation, LEED, STM and an ALD chamber as shown in Figure 2.9. Interconnected chambers allow the transfer of samples without breaking the vacuum.

The module utilised in this work is module 5. It is the dedicated MBE-chamber for growth of phase change materials. The chamber is equipped with five high temperature effusion cells, two special cracker cells, and one electron beam evaporator, as shown in Figure 2.7. The high temperature effusion cells are loaded with Sn, Ge, Te, Ti, Bi, and special cracker cells are used for evaporation Sb and Se. A movable ion gauge or a quartz microbalance is employed to measure the fluxes. A manipulator for substrate holding is located at the center of the chamber, complemented by a heater near the substrate to ensure the requisite temperature for epitaxial growth. The manipulator is motor controlled and can be rotated 360° in-plane to achieve a more homogeneous deposition, and it enables the ARHEED analysis (see section 3.2). Additionally, a RHEED system is integrated into the growth chamber.

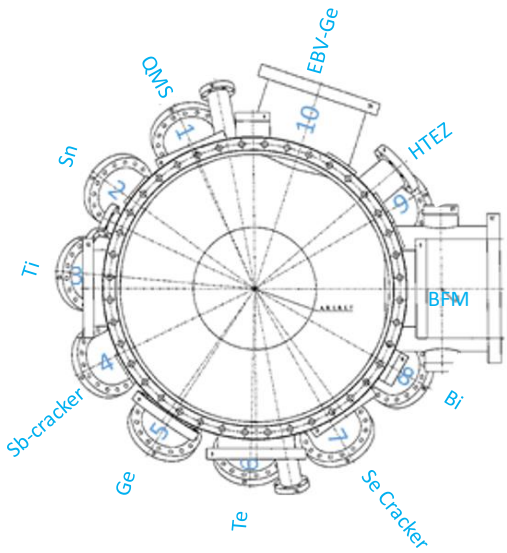

Figure 2.7: Schematic diagram of placement of effusion cells in Module 5

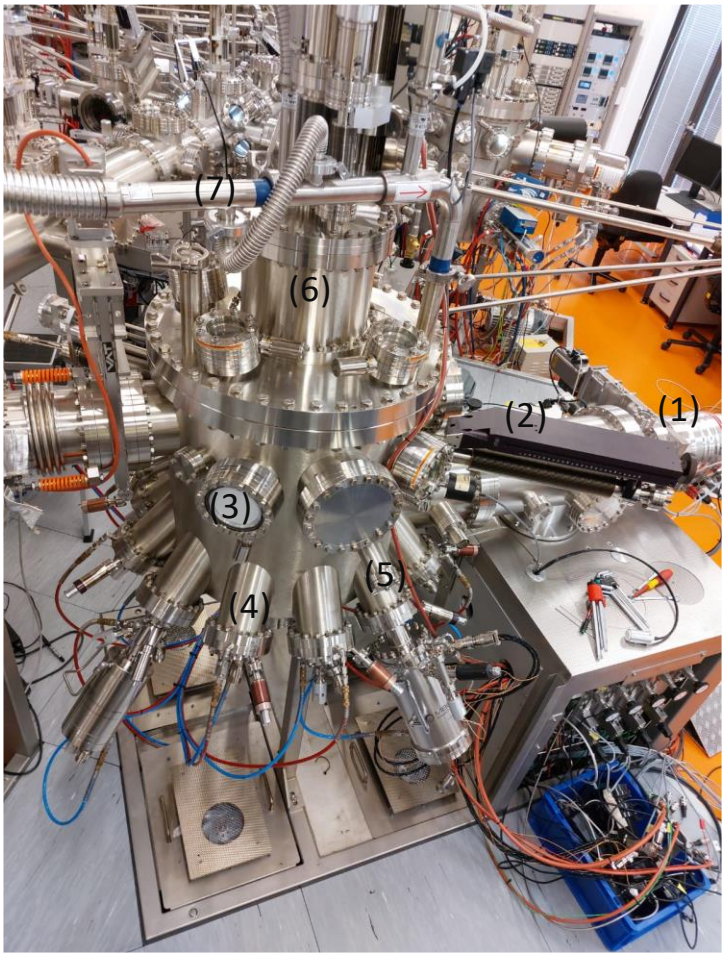

Figure 2.8: Nanocluster Facility Module 5: key components highlighted - (1) pump arm, (2) beam flux monitor, (3) RHEED screen, (4) effusion cell, (5) cracker cell, (6) upper part of the manipulator, and (7) liquid nitrogen inlet.

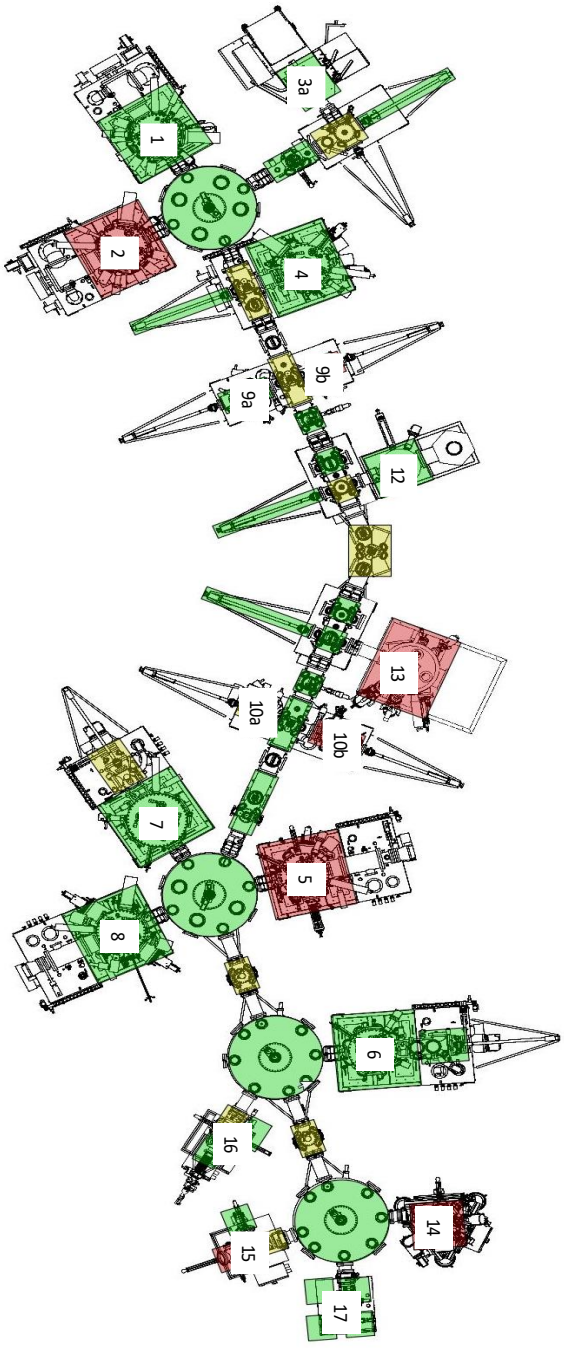

Figure 2.9: Overview of Nanocluster HNF: 1) III-V-MBE (As) 2) III-V-MBE (Sb) 3) ALD 4) metal MBE 5) PCM MBE 6) oxide sputter tool 7) metal sputter tool 8) metal-oxide MBE 9a/b) left load lock system 10a/b) right load lock system 12) II-VI MBE 13) TI-MBE 14) SEM/FIB 15) LS SPM-Module 16) Leed-Module 17) TLE-Module.

2.5 Choice of Substrate and Sample holder:

The extensive investigation by Wang et al. [32] into the growth of GeTe on Si(111) has unveiled distinctive phenomena related to the amorphous-to-crystalline transition, especially noticeable at ultra-thin film thickness. This thesis significantly contributes to exploring Peierls distortion in such films, emphasizing its comparative analysis on silicon surfaces due to the precedent set by prior research on this substrate. Growth of GeTe, SnTe SnSe has been reported in the literature on substrates such as BaF_2, GaAs, MgO and Sapphire. This work investigates Silicon as a potential substrate material.

The selection of silicon as the substrate material is justified by its advantageous attributes, including ready availability, cost-effectiveness, non-toxicity, stability, and comprehensive understanding. Given its foundational role in modern electronics, Silicon, functioning as a semiconductor, facilitates controlled conductivity modulation by introducing dopants.

In a classical approach, a substrate material is chosen based on the mismatch to the desired film. This choice ensures minimal film stress and a small number of dislocations at the interface of film and substrate. In the table, lattice mismatch is shown for the materials studied on silicon surfaces in this thesis.

Epitaxial relationship	**Lattice mismatch[%]**	**Ref.**
GeTe[110]||Si[110]	8.38	[33]
GeTe[010]||Si[110]	43.50	[32]
GeTe[112]||Si[112]	8.38	[32]
GeTe[100]||Si[112]	148.56	[33]
4 × GeTe[010]||6 × Si[110]	3.69	[33]
4 × GeTe[100]||11 × Si[112]	2.04	[33]
SnTe[001]||Si[111]	17.9	[34]
SnTe [111]||Si[111]	16.1	[35]
6 x SnTe[001]||5 x Si[111]	1.5	[36]
Sb2Te3[0001]||Si[111]	10.4	[36]
SnSe[010]||Si[110]	15.62	[37]
SnSe[001]||Si[110]	7.68	[37]

Table 2.2: Lattice mismatch of studied materials

Furthermore, the compatibility between the silicon substrate and the silicon holder offers a significant advantage, as both materials share similar optical and thermal properties, ensuring a uniform temperature profile. This thesis utilizes single-crystalline silicon wafers sourced from Siegert Wafer, grown in the (111) direction with a miscut of ±0.5° and a thickness of 0.5 mm. The n-doped (phosphorus) wafers, with a diameter of 100 mm (4 inches) and a resistivity of 3,000 Ω·cm, are polished on both sides. To maximize sample yield and fully utilize the surface area of the 100 mm wafer, it is sectioned into 35 mm x 35 mm pieces, as illustrated in the figure.

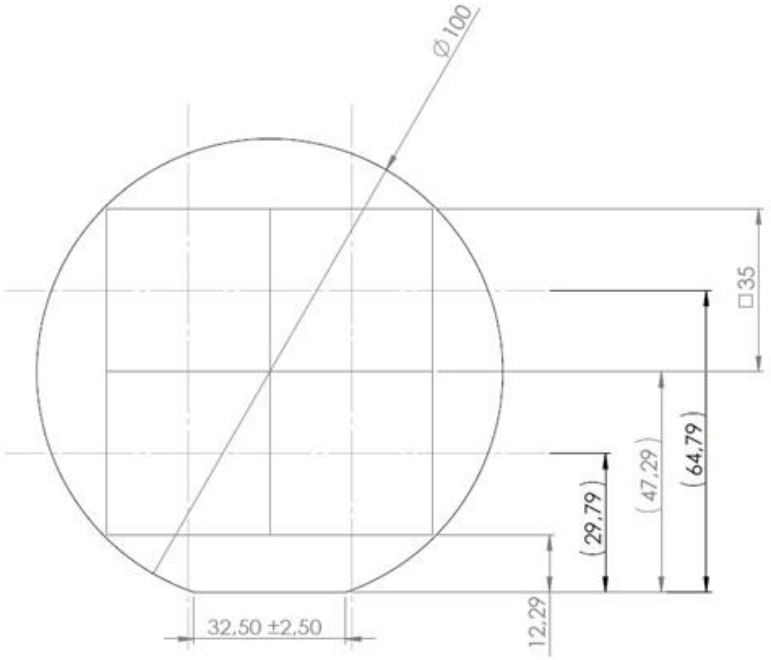

Figure 2.10 The 4-inch silicon wafer is precision-cut into four individual square samples, each with dimensions of 35x35 mm², ensuring accuracy in sample preparation.

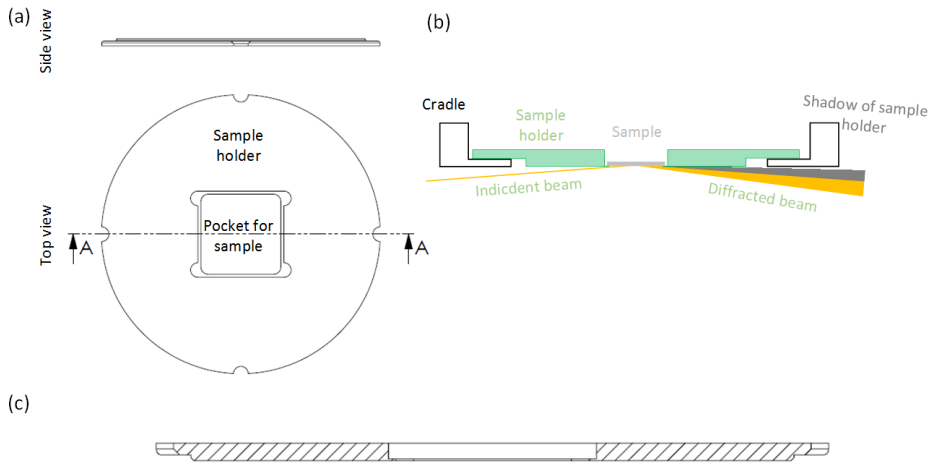

Figure 2.11: The figure (a) illustrates the side and top views of the sample holder design. Both the sample holder and the substrate are fabricated from silicon material. The standard holder accommodates a 35x35 mm^2 sample. The holder's positioning is adjusted to achieve a low RHEED angle, as depicted in (b). A cross-section at plane A, as defined in (a), is depicted in (c). Four QR codes and labels are also etched onto the surface to facilitate holder identification. Taken from [36]

The sample holder is typically made from silicon, molybdenum, titanium, or tantalum for use in nanocluster experiments. It is required to clean the sample holder after each deposition to prevent cross- contamination in the nanocluster. Aqua regia is a potential cleaning agent for holders that have been deposited with the materials studied in this work. However, molybdenum, a common holder material, poses a challenge as it corrodes in aqua regia.

In ultrahigh vacuum (UHV) environments, titanium, tantalum, and silicon are viable alternatives. Titanium's high vapor pressure limits its use to low temperatures, and tantalum is both expensive and difficult to machine. Despite silicon’s brittleness, it shares key properties with the sample material, which helps ensure a uniform temperature profile. The holder design optimizes the RHEED beam angle by positioning the sample at the lowest point, thereby enhancing mechanical endurance, as illustrated in the Figure 2.11.

2.6 Wet Chemical Wafer Cleaning

Initially, the 100 mm wafer undergoes a protective resist spin-coating process using AZ5214E photoresist from Micro Chemicals. This photoresist protects against contamination from particles and cooling liquid during the sawing process. Subsequently, the wafer is cut into 35x35 mm^2 pieces, and the resist is removed using acetone followed by isopropanol.

The cleaning process aims to eliminate both organic and metallic particles while removing the native oxide layer from the silicon surface. Removal of the native oxide is crucial as it obstructs the silicon single crystal required for epitaxy. The cleaning procedure follows the RCA (Radio Corporation of America) protocol commonly adopted in semiconductor industries. Essentially, the RCA-based process involves etching particles to remove them from the surface, often involving oxide deposition

and removal cycles. To clean the silicon wafer pieces, they are immersed for 10 minutes in a freshly prepared piranha solution, comprising 2 parts 30% hydrogen peroxide and 1 part 96% sulfuric acid. The exothermic reaction between hydrogen peroxide and sulfuric acid generates heat, eliminating the need for external heating during the cleaning process. Subsequently, the substrates are rinsed with DI-water and then immersed in a 1% HF solution for 2 minutes.

Following this, the substrates are subjected to SC-1 solution, heated to 60°C, consisting of 20 parts DI-water, 4 parts 30% hydrogen peroxide, and 1 part 30% ammonia solution, for 10 minutes. After rinsing with DI-water, the substrates are immersed in 1% HF for 2 minutes. Next, the substrates are treated with SC-2 solution, heated to 60°C, and comprised of 20 parts DI-water, 1 part 30% hydrogen peroxide, and 1 part 37% hydrochloric acid, for 10 minutes. After a final rinse with DI-water, the samples can be stored for at least 2-3 months under clean room conditions. Before the sample was used, they were immersed in 10% HF for 2 minutes and rinsed with DI-water. This final step removes the oxide layer and passivates the Si surface with hydrogen atoms, preventing further oxidation in air for a limited time. The substrate is then immediately placed in the load lock under a vacuum range of 10^{-6} to 10^{-8} mbar. Once the pressure reaches the range of 10^{-8} mbar, the substrate is transferred to the MBE chamber, where a base pressure is in the order of 10^{-10} to 10^{-11} mbar.

3 Experimental Setup

This chapter provides an overview of the various in-situ and ex-situ analytical techniques employed in this work to optimize the IV-VI monochalcogenide thin film growth conditions and their characterization. Due to the strong interaction of electrons with matter, Reflection High-Energy Electron Diffraction (RHEED) is highly surface-sensitive, making it a powerful technique for detecting changes in surface-level order, and hence particularly useful for examining ultra-thin films. Section 3.1 covers the fundamentals of the RHEED setup, which plays a crucial role in examining the substrate surface before and during deposition, ensuring sample reproducibility. This section also details the correlation between RHEED patterns and thin film growth modes, lattice constant calculations, growth rate determination, and crystal azimuth adjustments using Kikuchi lines. Section 3.2 describes the RHEED analysis performed during sample rotation and generation of an ARHEED image. Sections 3.3, 3.4, and 3.5 focus on the ex-situ techniques used in this study to calculate lattice constants, analyze the epitaxial relation with the substrate, and determine thin film roughness and thickness.

3.1 Reflection High-Energy Electron Diffraction

Nishikawa and Kikuchi pioneered Reflection High Energy Electron Diffraction (RHEED) in 1928. RHEED is an in-situ, surface-sensitive technique widely employed in nearly all Molecular Beam Epitaxy (MBE) systems for real-time characterization of growth processes. It facilitates the determination of essential parameters such as growth rate, unit cell dimensions, in-plane lattice constants, surface roughness, growth mode, crystallinity, surface reconstruction, and the epitaxial relationship between the substrate and the film.

Due to the low glancing angle of incidence, RHEED electrons interact with only the top few atomic layers, making it highly sensitive to surface characteristics. This sensitivity allows for effective monitoring of surface-level order changes during deposition, which is particularly advantageous for studying ultra-thin film effects. In this work, RHEED was employed as a critical tool to examine the substrate surface both, before and during the deposition process, ensuring sample consistency and reproducibility.

3.1.1 Fundamentals of RHEED

The RHEED setup is relatively simple; the three main components of a RHEED experiment are an electron gun, a sample with a pristine surface, and a fluorescence screen. (Figure 3.1) The electron beam is set to an energy value ranging from 8KeV to 100KeV and hits a sample at a fairly low incident angle, usually 0.5° to 6°. The resulting diffraction pattern is sensed by a phosphorescent screen

opposite the electron gun and recorded digitally by a charge-coupled device. According to Kanaya and Okayama [38], the penetration depth of the electrons depends on the accelerating voltage of the electrons, the material the electron is penetrating, and the angle the electrons are impinging on the surface. The equation below can be used for estimating the penetration depth R:

$$R = \frac{2.76 \times 10^{-12} E^{1.67} A}{\rho Z^{\frac{8}{9}}}$$

A is the atomic weight, *E* is the accelerating voltage (20 keV), *ρ the* density, and *Z* is the atomic number. For Silicon, the calculated penetration depth is about 47.3 Å. Further, the penetration depth decreases by a factor $l = Rsin\theta$ *at* an angle of θ. For a grazing incidence angle of 2.6°, the penetration depth is about 2.14 Å, resulting in highly surface sensitive diffraction at the surfaces. A low incident angle is crucial for studying surface order in the system. Typically, the incident angle of the electron beam is below 3°, making this technique highly surface-sensitive, with only the first few monolayers contributing to the RHEED pattern. Thus, real-time monitoring of surface evolution during growth is possible with RHEED. In this work, measurements were conducted with an accelerating voltage of 20 keV, a current of 1.42 mA, and an incident angle of about 2.6° at the sample. The electron beam has an estimated diameter of 100 µm, and when it intersects the surface, it forms an ellipse with a diameter of approximately 3 mm. Unfortunately, the larger spot size due to the grazing angle leads to averaging across the surface.

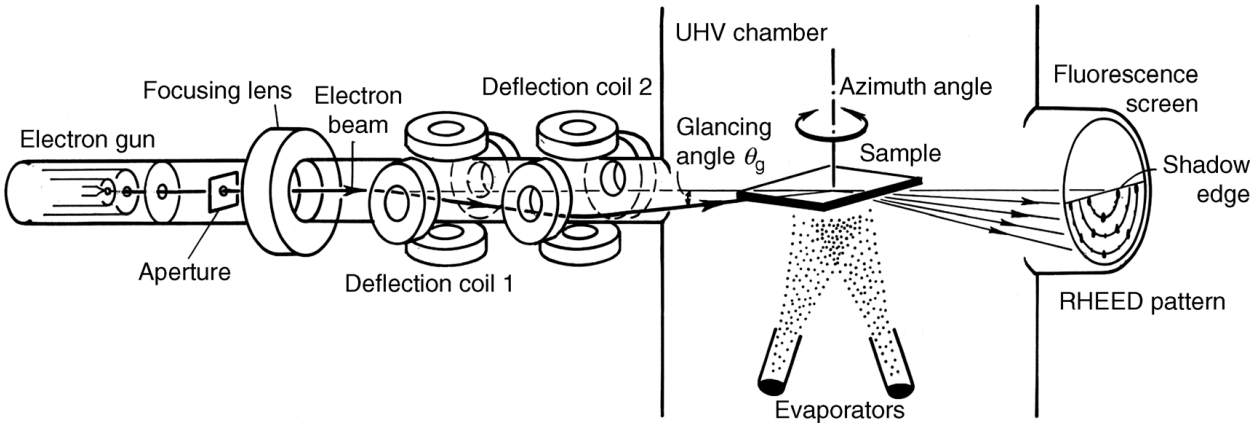

Figure 3.1: The simplest RHEED setup includes an electron gun, a sample, and a fluorescent screen across from the gun. A lens focuses these electrons on the sample through deflection coils. The glancing angle ϑg is typically 1°to 4°. A rotation of the sample is possible. The diffracted electrons are visualized on a fluorescence screen Taken from[39].

The diffraction observed is based on Bragg diffraction principles. In kinematical scattering theory, electrons undergo a single, elastic scattering event, satisfying the condition for constructive interference. This means that intensity on the screen can only occur if the difference between the

incident wave vector (k_i) and the diffracted wave vector (k_f) is a reciprocal lattice vector (Δk), as described by the Laue equation. This key relation leads to the model of the Ewald sphere in reciprocal space, which is employed in RHEED. According to the elastic scattering approximation, the energy of the electrons is conserved, so that $|k_i| = |k_f|$.

The de Broglie wavelength (λ in Å) of an electron by a voltage difference accelerated V (in eV) is given by:

$$\lambda = \sqrt{\frac{150.4}{V}}$$

For a 20 keV electron beam, λ is 0.087 Å, and the corresponding magnitude of the wavevector k is 72.5 $Å^{-1}$. As a result, the Ewald sphere will be very large. For comparison, the unit cell of GaAs is roughly 70 times smaller.

The sample's lattice can be considered as a two-dimensional lattice due to the low penetration depth of the electrons. In reciprocal space, the reciprocal lattice of a two-dimensional surface is represented by infinitely long, one-dimensional rods perpendicular to the surface, known as Crystal Truncation Rods (CTRs). Figure 3.2(a) and (b) illustrate the sample's surface in reciprocal space, while Figure 3.2(c), (d), and (e) show how the CTRs intersect the Ewald sphere to produce diffraction maxima on the screen. As shown in Figure 3.2(c), reflections from the same series of vertical rods lie on the same Laue circle. The smallest circle represents the 0^{th} Laue zone, and the next one is the 1^{st} Laue zone, and so on. Ideally, a perfect single crystal with an atomically flat surface would have well-defined atomic positions, resulting in reciprocal rods with infinitesimally small diameters and uniform intensity. This would produce spots only on the Laue circle with consistent intensity on the RHEED screen, as shown in Figure 3.2(c). However, in practice, the intensity along reciprocal rods is modulated due to factors such as the electron beam's interaction with both surface and subsurface atoms, beam divergence, and non-ideal surface conditions. Figure 3.2(d) shows the case where monolayer roughness of the surface causes the reciprocal rods to broaden, leading to intersections with the Ewald sphere that appear more like elongated ellipsoids, which manifest as broader reflections on the screen. In the case of a highly rough surface, reciprocal lattice points result in a transmission spot pattern on the RHEED screen as in Figure 3.2(e). The detailed cases of different surface conditions and the corresponding RHEED patterns are discussed further in section 3.1.2.

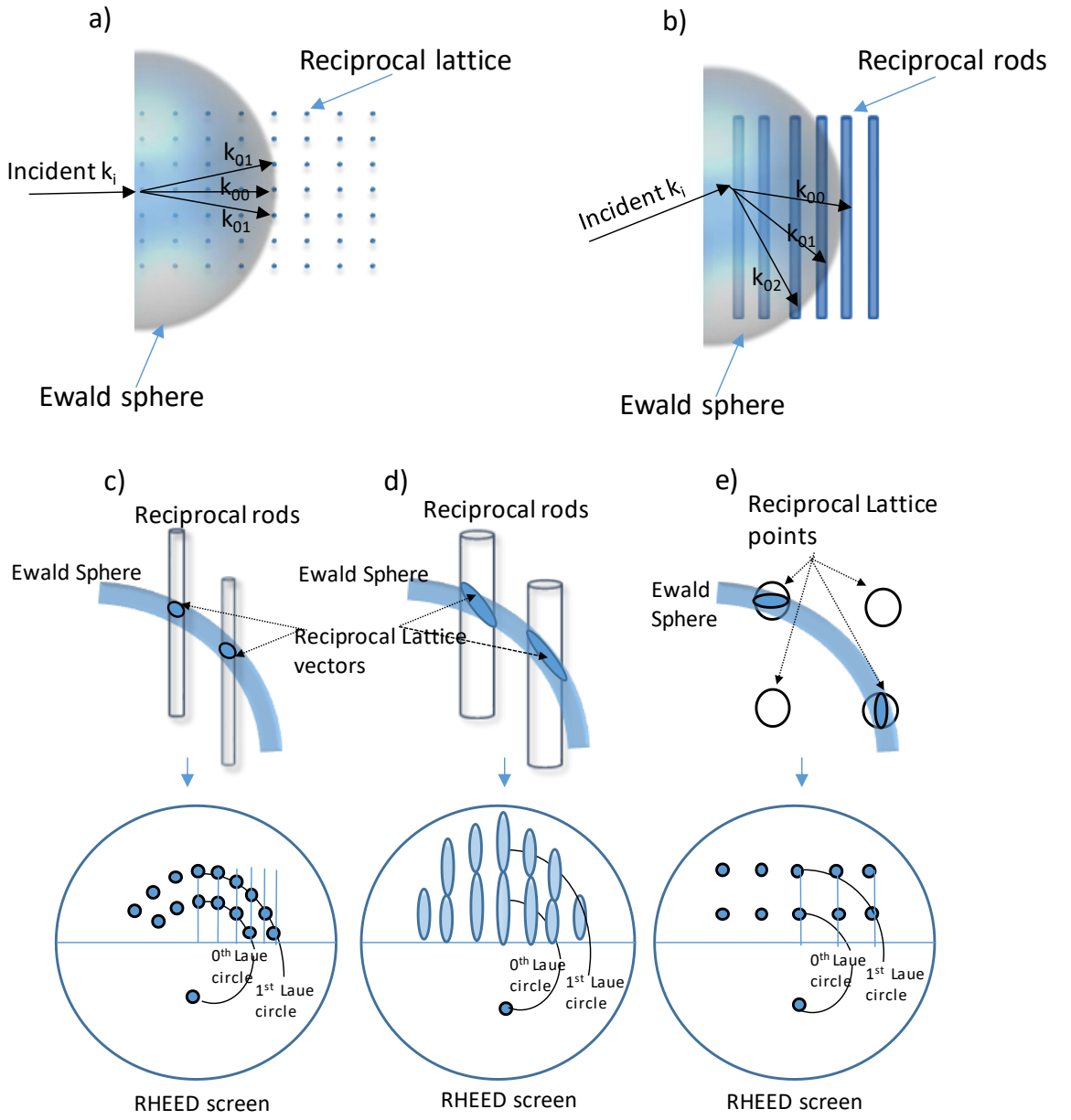

Figure 3.2: The Ewald sphere's principal construction in top view (a) and side view (b). (c,d,e) illustrates how reciprocal rods intersect with the Ewald sphere in different cases of film surface roughness and corresponding reflexes pattern on RHEED screen. (c) ideal single-crystal surfaces produce sharp reflections on Laue circles. (d) monolayer roughness broadens reciprocal rods, leading to elongated reflections. (e) highly rough surfaces like 3D islands result in transmission spot patterns.[recreated using concept [39]]

3.1.2 RHEED Pattern

Actual crystals often deviate from ideal conditions: their surfaces may not be atomically flat or may contain domain sizes smaller than the electron beam's coherence length. In such cases, reciprocal rods appear broader, and their intersections with the Ewald sphere form larger ellipses, resulting in elongated and broader diffraction spots (streaks) on the RHEED pattern, as shown in Figure 3.3.(b)

Typically, the average size of the domains (grains) is inversely proportional to the width of the reciprocal rods or the width and length of the RHEED spots. [39] Therefore, the smaller streaks are indicative of larger grains.

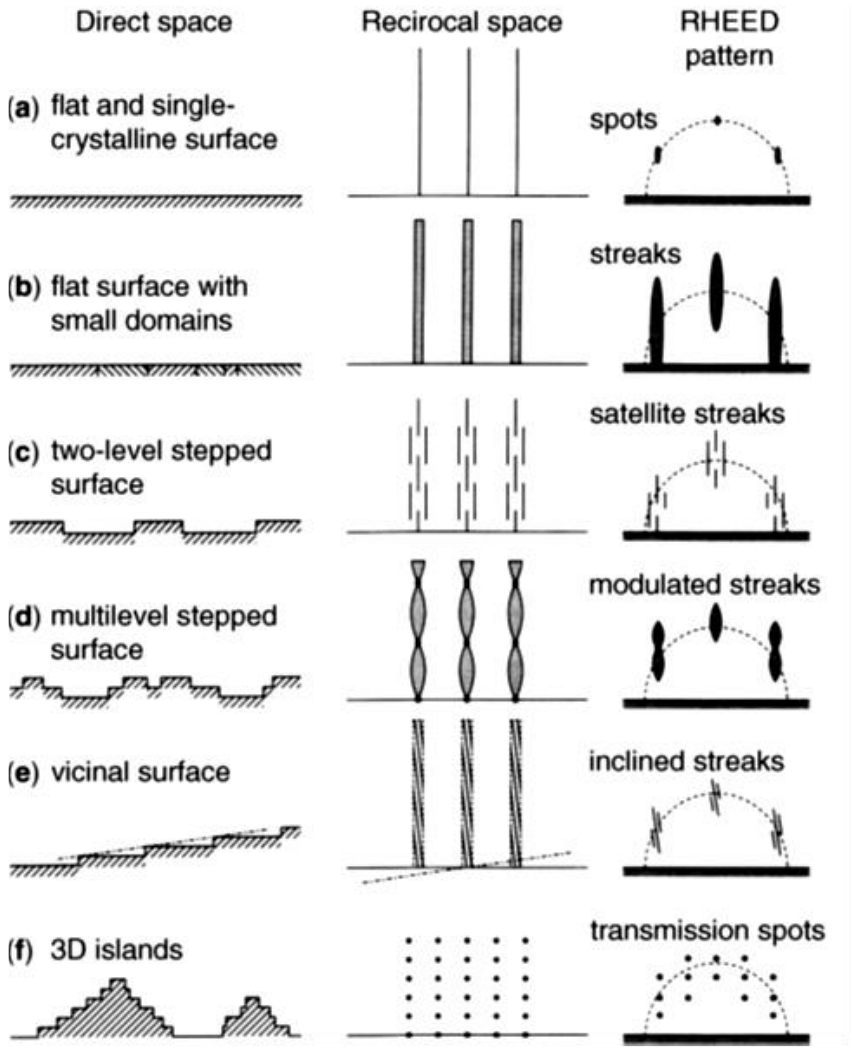

Figure 3.3 Schematics of various realistic surfaces, illustrating their real-space morphology, reciprocal space representation, and corresponding RHEED patterns.[39]

Further, RHEED patterns or reciprocal rods become more complex when the surface has two-level steps with a one-atomic height difference, as illustrated in Figure 3.3(c). In this scenario, the terraces cause the diffracted waves from the lower and upper steps to interfere with each other, either constructively or destructively. Constructive interference results in sharp reciprocal rods with intensity similar to that of atomically flat surfaces. Conversely, destructive interference from two terraces leads to the splitting of reciprocal rods into two, with the diffraction spots also splitting into satellite streaks. The intensity of the diffracted beam is weakened. In the case of a multilevel stepped surface, the reciprocal rods exhibit twisted, broader structures, as shown Figure 3.3(d). This occurs due to the multiple times' destructive interference of waves from different terrace and can be understood as a superposition of split reciprocal rods in Figure 3.3(c), with changes in their positions.

Sharp node-like features appear due to the fulfillment of constructive interference conditions, leading to modulated streaks in the RHEED patterns.[39]

For a vicinal, stair-like surface, the reciprocal rods consist of thinner and finer rods within the broader rods, oriented perpendicular to the surface of the steps. However, since the surface is slightly inclined, the resulting RHEED pattern exhibits inclined streaks, as seen in Figure 3.3 (e). Additionally, as shown in Figure 3.3(f), when the surface is rough with three-dimensional islands, and islands are epitaxial grown on the surface, the reciprocal lattice consists of a three-dimensional array of reciprocal points instead of rods. Here, the electrons transmit through the islands and get refracted. Regardless of the azimuthal angle, the transmission spots on the RHEED screen remain unchanged. It is a visibly different spot pattern than one originating from a flat, single crystalline surface. In the case of amorphous film growth, where periodicity is lacking, no reflexes appear on the RHEED screen. Thus, it is easy to identify amorphous versus crystalline growth with in-situ RHEED. Consequently, the surface morphology and thin film growth modes can be studied based on the arrangement of reflexes on the RHEED screen. In this work, RHEED patterns were used to monitor surface morphology and serve as an indicator of surface flatness during deposition, as demonstrated in Chapter 5.

3.1.3 Kikuchi Lines

Apart from the previously discussed patterns, specific Kikuchi patterns are also observed on the RHEED Screen. These patterns originate from the inelastic scattering of incident electrons, followed by diffraction at the lattice. The line-like features of Kikuchi patterns are shown in Figure 3.4. The intensity of these Kikuchi lines is highly sensitive to surface morphology, with scattering from small steps and terraces causing broadening of the lines. Sharp and well-defined Kikuchi lines are indicative of a highly crystalline film with an atomically smooth surface. One of the key characteristics of Kikuchi lines is their rotation with changes in the crystal's azimuth. Even slight adjustments in the azimuth angle such as less than one degree, can lead to noticeable shifts in the position of these lines on the RHEED screen. This sensitivity allows Kikuchi patterns to be used as a precise tool for setting the crystal azimuth along a symmetry direction. This makes Kikuchi patterns invaluable for ensuring that the crystal is properly oriented during surface studies and thin film deposition processes in this work. [40]

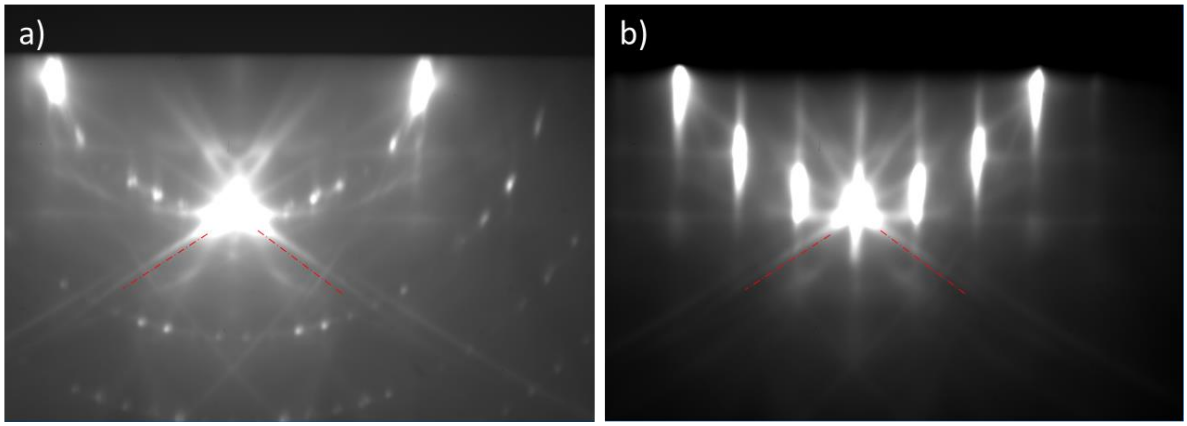

Figure 3.4: RHEED pattern (a) shows a Si(111)7 × 7 reconstructed surface and (b) Si(111)-(√3 ×√3)R30°-Sb terminated surface measured at 20 keV electrons, in the incident direction[11$\bar{2}$]. Sharp line-like features indicated with red line in both images, known as Kikuchi patterns.

3.1.4 RHEED Oscillations

In the early 1980s, Dobson, Harris, Joyce, and Wood (Harris et al., 1981) first reported the observation of RHEED intensity oscillations. They measured the intensity of the specular diffracted beam as a function of time following the initiation of growth on a smooth GaAs surface. These oscillations provide critical insights into film growth dynamics, including the growth rate, growth mode, surface diffusion, and overall film quality during layer deposition.

RHEED is highly sensitive to surface conditions, enabling the detection of intensity variations between partially deposited and fully closed monolayers. These oscillations are particularly valuable for distinguishing between different growth modes, such as layer-by-layer growth and island nucleation. In layer-by-layer growth, the oscillations exhibit a regular periodicity, corresponding to the completion of each atomic layer. The period of these oscillations is directly related to the time required to deposit a single monolayer, facilitating precise calibration of the growth rate.

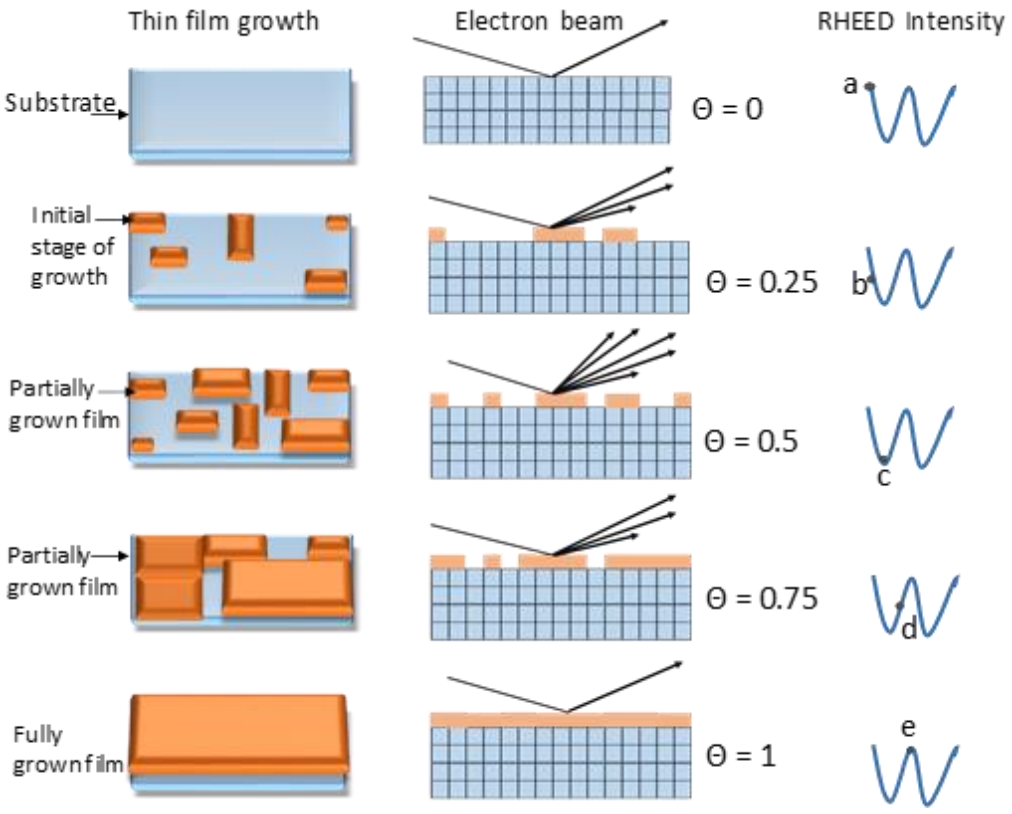

Figure 3.5: The schematic diagram shows the origin of RHEED oscillations in two-dimensional thin film growth. As growth proceeds, nucleation creates additional scattering centers on the substrate surface that decrease the intensity of the reflected electrons. As the monolayer is completed, the RHEED intensity increases. Recreated from [39]

Conversely, in island nucleation, the oscillatory patterns are more complex, often due to variations in surface roughness. The amplitude and envelope of the oscillations provide additional information on surface roughness and island density, with oscillation amplitude typically diminishing as growth progresses, reflecting increased roughness and the coalescence of islands. Although these oscillations can be visualized on a phosphor screen, they are more commonly recorded over time using a CCD camera for detailed temporal analysis.

A simplified schematic of RHEED intensity oscillations is shown in Figure 3.5. During the growth of a two-dimensional layer on the crystalline substrate, the intensity of the RHEED zero-order (specular spot) diffraction beam varies as a function of atomic coverage (θ), as depicted by the RHEED intensity at points (a, b, c, d, e) in Figure 3.5. Initially, the bare crystalline substrate (θ = 0) produces a high diffraction intensity (a), typically at its maximum due to the perfect crystalline structure. As growth begins, two-dimensional crystal nuclei form and expand, increasing diffuse scattering and causing a decrease in the specular spot intensity (b). The intensity continues to decline (c) until a half-monolayer is deposited (θ = 0.5). With further growth, the coalescence of nucleated islands leads to the formation of a complete monolayer (θ = 1), at which point the intensity again reaches a maximum (e), indicating the completion of each layer.

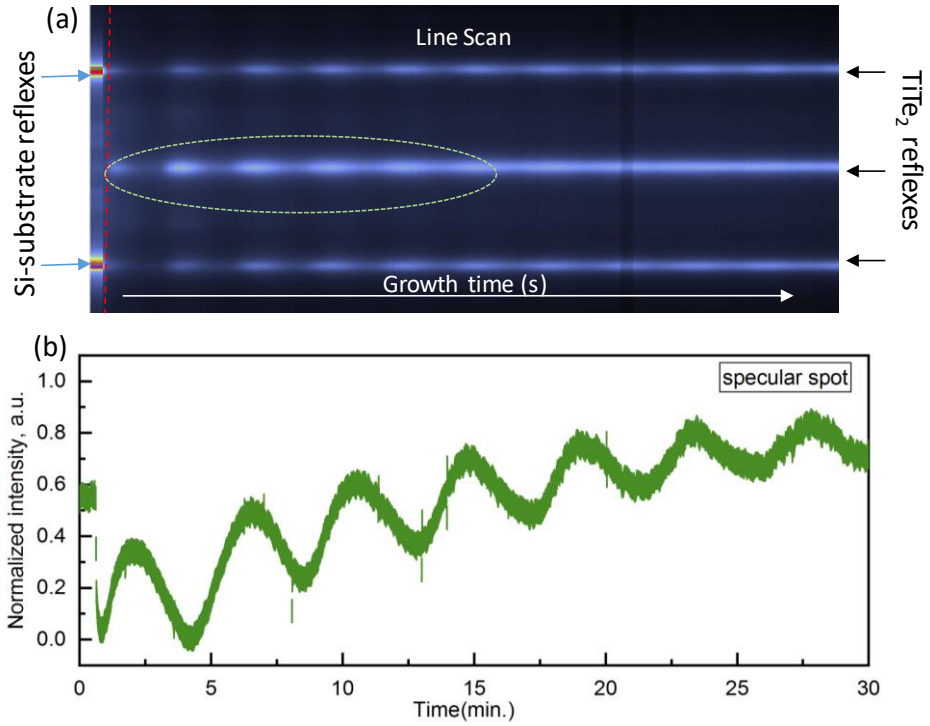

Figure 3.6: (a) the RHEED line scan indicates the presence of intensity oscillation (b) plot of specular spot intensity as function of growth time.

For example, during the deposition of $TiTe_2$ on a silicon substrate, RHEED intensity oscillations were observed and recorded by measuring the intensity of the specular reflection spot through a line scan Figure 3.6 (a). The variation in specular spot intensity was plotted as a function of deposition time shown in Figure 3.6 (b). It is important to note that RHEED oscillations are typically associated with layer-by-layer growth and are rarely observed during the growth of phase-change materials (PCMs).

In this work, RHEED is used to monitor the growth process and to investigate the crystal orientation of the grown films.

Most analysis of RHEED images require a static sample. Much information, such as the growth mode and lattice evolution at ultra-thin film thicknesses, is often lost when films are grown with a rotating substrate condition. From the construction of the Ewald sphere (more details section 0) and its intersections with the diffraction rods, it is evident that the distance between diffraction spots on the screen is directly proportional to the lattice parameters. Thus, static RHEED images can be used to determine the in-plane lattice constants of the grown crystal film.

To accurately determine lattice constants, system calibration is essential. This involves measuring a material with a known lattice parameter, such as a silicon substrate, which is readily available and ideal for this purpose. The unknown lattice parameter of the film, a_{film} , can be calculated using equation:

$$a_{film} = \frac{d_{ref}}{d_{film}} . a_{ref}$$

Where, a_{ref} is the lattice parameter of the reference substrate, d_{ref} *is* the distance between the reflexes of the substrate crystal, and d_{film} is the corresponding distance for the film. It is important to ensure that the reference material has a crystalline structure identical to the film being measured. For example, the hexagonal surface of a Si(111) substrate is suitable for determining the lattice parameter of hexagonal Sb_2Te_3, but not for cubic SnTe. In such cases, a lattice transformation is required.

With RHEED installed in the MBE chamber alongside a CCD camera, it becomes possible to investigate the lattice parameter as a function of time or film thickness, even at ultra-thin film scales. If the in-plane lattice constant changes due to strain or a crystal structure transition, the corresponding rods will shift, leading to a corresponding movement of the reflexes on the screen.

In this work, Si(111) was selected as the substrate for thin film growth. Figure 3.6 shows an illustrative measurement where the silicon reflexes have a distance of approximately 858 pixels, while those of GeTe measure 792 pixels. Multiplying the ratio of these distances by the lattice parameter of the Si(111) surface, which is 3.84 Å, yields a value close to the literature value of 4.16 Å for hexagonal GeTe. Further analysis of lattice constant of the materials studied thin films is discussed in Chapter 6.

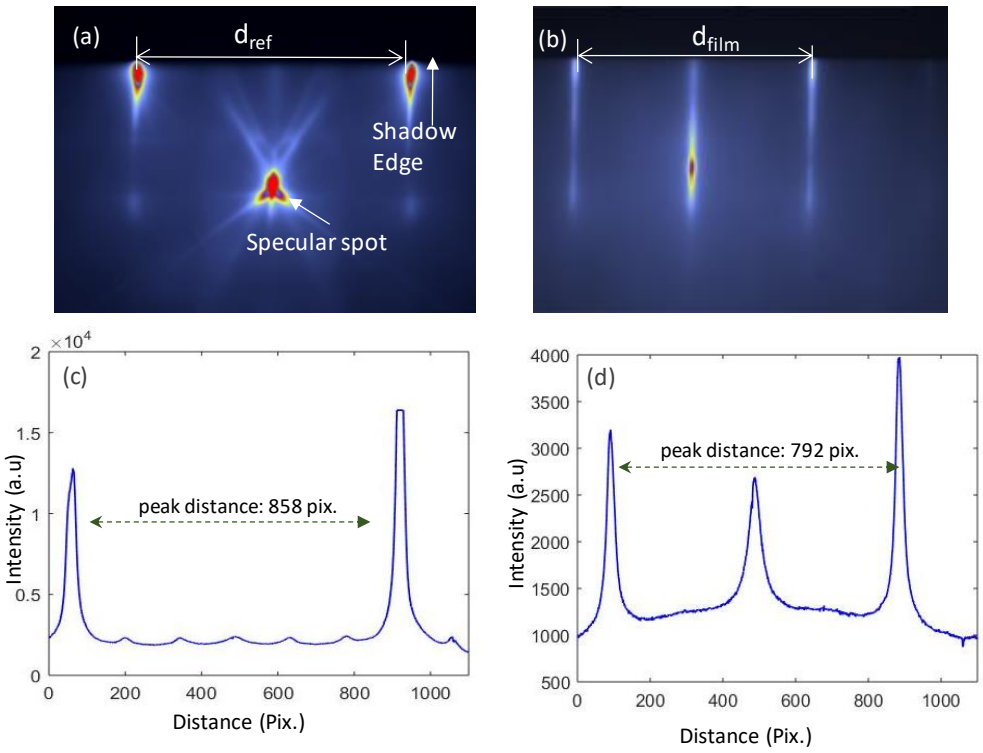

Figure 3.7: (a) RHEED image of Si(111)1x1 surface (b) RHEED image of GeTe reflexes at the end of growth. Intensity plots showing the peak distance for used for lattice constant analysis of Si(111) reflexes (c) and GeTe reflexes(d).

3.2 Azimuthal RHEED

In 1998, Braun et al. introduced Azimuthal RHEED (ARHEED), also known as Weissenberg RHEED (W-RHEED), to investigate GaAs surface reconstruction. This technique involves collecting multiple RHEED patterns by varying the azimuthal angle (φ) of the incident electron beam, rather than altering the glancing angle (θg). To understand ARHEED image formation, it is essential to consider the construction of the Ewald sphere. During sample rotation, the (00) reciprocal rod acts as the center of an array of rotating reciprocal rods (see Figure 3.8). The Ewald sphere remains stationary in space, assuming any system wobble is negligible. As the sample rotates, some rods enter the fixed Ewald sphere, while others exit.

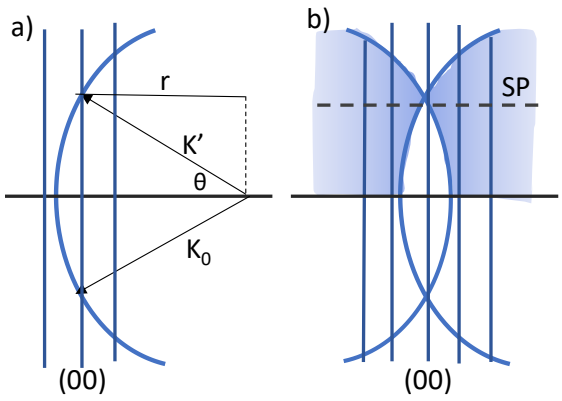

Figure 3.8: shows a schematic diagram of (a) the Ewald sphere for a static RHEED picture and (b) for the whole rotation; the sample is rotated around (00). The shaded area represents the volume of reciprocal space accessible during a single sample rotation. The plane without a void in the center is the specular plane that intersects the specular spot indicated by a dashed line. Redrawn from [41]

Because the Ewald sphere is fixed, it scans nearly the entire upper half of the reciprocal space during the sample's rotation, as represented by the shaded area in the figure. The largest volume of reciprocal space is scanned when the electron beam's incidence angle is smallest, which enhances surface sensitivity. Although this setup theoretically allows for the reconstruction of nearly the entire upper half of the reciprocal space during one full rotation of the sample, real-time analysis is constrained by current computational limitations. To manage data effectively, the analysis is typically focused on a specific plane parallel to the surface, known as the specular plane (SP). This plane, marked by a dashed line in the figure, is selected because it contains the specular spot (a bright reflection point in RHEED patterns) and is continuous across the (00) rod. Details on ARHEED are further discussed in [41–43].

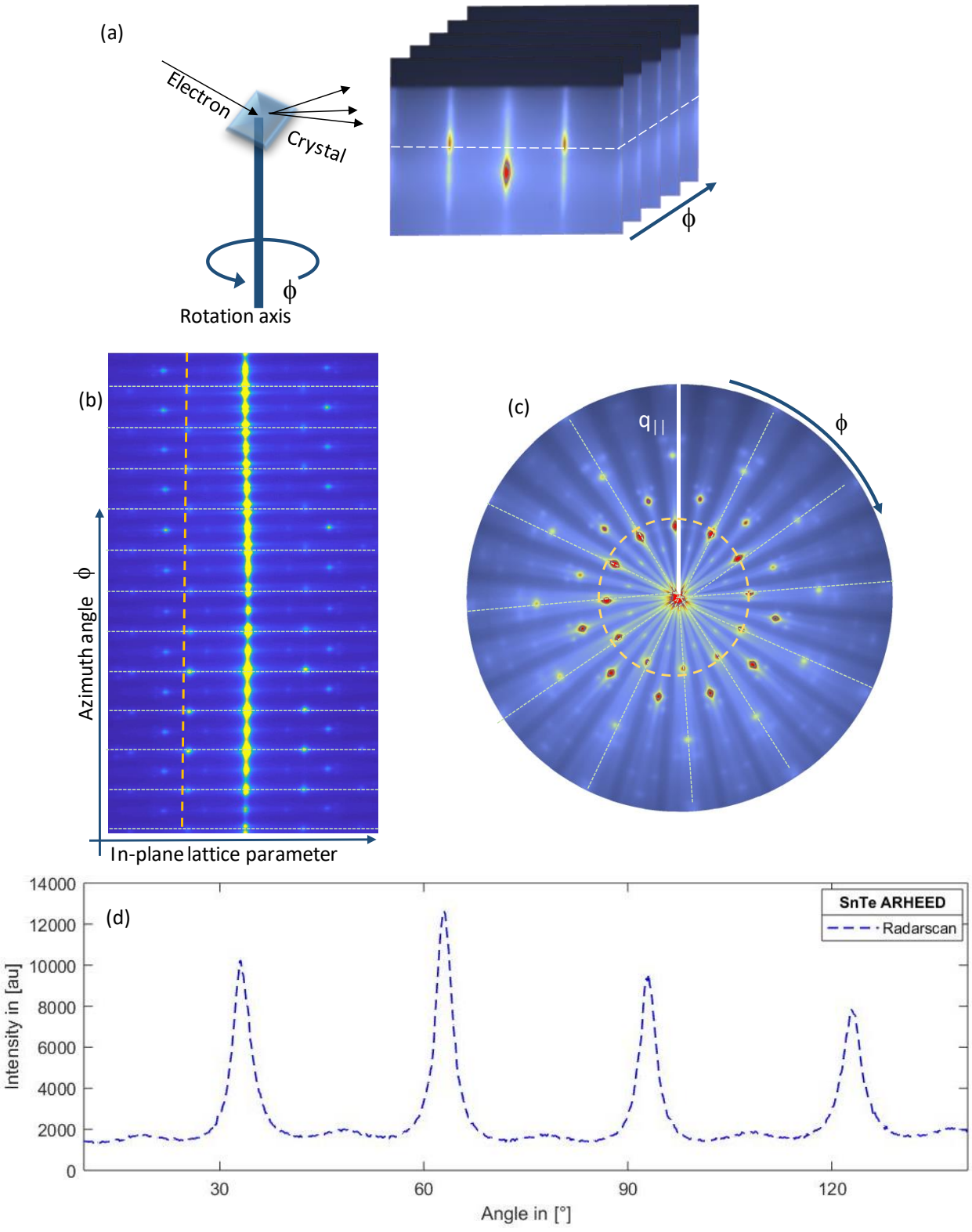

Figure 3.9: ARHEED image generation. (a) Multiple RHEED images are collected by varying the azimuthal angle (ϕ) of the incident electron beam followed by choosing a line from each frame, (b) plotted as a function of the azimuth angle ϕ, (c) keeping specular spot as center, assembled images in circular picture and selected circle is analyzed further and (d) plotted as intensity vs azimuth angle for domain analysis in thin film.

To construct the ARHEED image, multiple images are taken during rotation ϕ of crystalline sample, which allows access to several individual cuts of the reciprocal lattice. The rotation speed must be known to correlate the rotation angle with the frames of the recorded line-scan video. Each frame's chosen line for analysis contains a specular spot parallel to the shadow edge as demonstrated in Figure 3.9 (a). These lines are plotted as a function of the azimuth angle ϕ as in Figure 3.9 (b) and assembled in a circular picture by keeping the specular spot position fixed as illustrated in Figure 3.9 (c). The resulting image provides the information about epitaxial domains present in the film. To closely observe the epitaxial domain along the dashed line in image (c), the azimuthal angle vs the intensity is plotted in Figure 3.9 (d). In chapter 5, this method is used to study the epitaxial domains at the end of the film growth. The system used here for the analysis of ARHEED captures a frame every 140 ms using a CCD camera. In this work, the parameters used are consistent with those in Ref. [36]

ARHEED is a fast measuring method since it is possible to measure in real-time during deposition within the growth chamber. It provides information on the lattice constant and the epitaxial orientation of the deposited film. ARHEED is comparable to the pole figures obtained from X- ray Diffraction (XRD). The advantage of ARHEED is in-situ analysis. Compared to the phi scan from XRD, the ARHEED is a much more sensitive technique for analyzing rotational domains in ultra-thin films.[36]

In conclusion, in this work, ARHEED is used to construct the reciprocal space maps and determine the symmetry of thin films on Si surfaces. Since it is possible to acquire data for ultra-thin films, it is an opportunity to compare the structure and rotational domains as a function of film thickness. Further experiments will be discussed in Chapter 5.

3.3 X-ray Diffraction

X-ray diffraction (XRD) stands as one of the most extensively utilized nondestructive techniques for analyzing crystal materials, providing insights into lattice constants, orientation, and internal stress. Particularly significant in the study of thin film materials, XRD aids in identifying film crystallinity and discerning strain effects between the film and substrate. Depending on the size of the investigated structures, different elements and, therefore, wavelengths can be chosen. In this work, Cu-radiation is used. The incident X-ray beam, when diffracted, follows specific directions dictated by the crystal structure. Through analysis of the angles and intensities of the diffracted beams, X-ray diffraction allows the identification of the three-dimensional structure of the crystal, following the principles of Bragg's Law:

$$n\lambda = 2d \sin\theta$$

where λ is the wavelength of the X-ray, d is the lattice plane spacing(d-spacing), and θ is the incident beam angle, n is an integer.

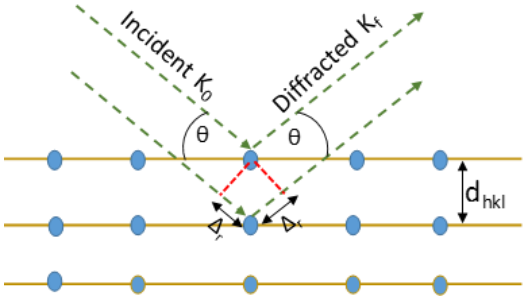

Figure 3.10: The schematic of Bragg's Law

In this work, the sample to be analyzed is mounted on sample stage in such a way that an X-ray beam illuminates the center of the sample. The sample can be rotated around three axes commonly referred axes as ω, χ, and φ shown in Figure 3.11 to obtain information about the different planes of the crystal. When the crystal (or the X-ray source) undergoes rotation around ω, the detector identifies the diffracted beam at 2θ. This rotation results in the diffraction of X-rays by the planes in the growth direction (typically out-of-plane) of the thin films. For the epitaxial films, the in-plane texture can be studied by rotating the sample around φ, in a process known as phi-scan. Another technique for in-plane analysis is the determination of the pole figure, which requires rotation of a sample around χ and φ. Detailed information about the structure of a crystal, including strain, crystallite size, lattice parameters and mosaicity, can be obtained from reciprocals space mapping (RSM) in XRD. For a more thorough insight on the techniques, refer to [44, 45].

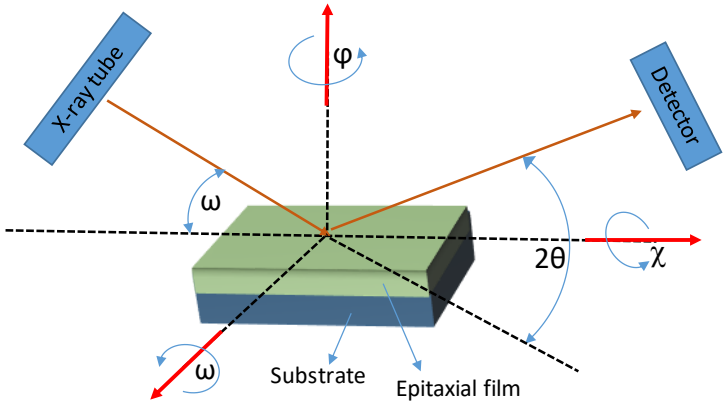

Figure 3.11: Schematic diagram of X-Ray Diffraction

3.4 X-ray reflectometry (XRR)

X-ray reflectometry (XRR) is an analytical technique used to investigate thin layered structures, surfaces, and interfaces by utilizing the effect of total external reflection of X-rays. In reflectivity experiments, the X-ray reflection of a sample is measured around the critical angle, which occurs at grazing incidence angles. Below the critical angle of total external reflection, X-rays penetrate only a

few nanometers into the sample; above this angle, the penetration depth increases rapidly. At each interface where the electron density changes, a portion of the X-ray beam is reflected. The interference of these partially reflected X-ray beams creates the oscillation pattern observed in reflectivity experiments. These reflectivity curves are used to determine layer parameters such as thickness, density, interface, and surface roughness.

X-ray diffraction and X-ray reflectometry analyses were conducted using a Bruker D8 Discover setup in this work, as part of a collaboration with the RWTH Aachen group. The incident X-ray beam is first parallelized with a Goebel mirror. The beam path offers versatility with options including a manual slit ranging from 0.1 mm to 1.2 mm, a monochromator, and a nozzle with diameters between 0.3 mm and 1 mm. Additionally, part of the measurements was carried out in collaboration with Dr. Jalil Abdur Rehman at Forschungzentrum PGI-9, utilizing a Rigaku Smart Lab system.

3.5 Scanning Electron Microscopy

The morphology of the thin-films grown were analyzed using scanning electron microscopy (SEM). In an SEM a beam of electrons is rastered across the surface, and the secondary electrons or the backscattered electrons are analyzed to study the topography of the sample. An SEM consists of an electron gun and electron optics to focus the beam on the sample, scanning coils to enable the beam to be rastered across the sample and various detectors to look at back-scattered electrons, secondary electrons and X-rays. The FEI Helios NanoLab 650 scanning electron microscope (SEM) was used in this study, operating at 10 kV and 400 nA, with a tilt angle of 0° and a variable working distance of 2-5 mm. Images were captured at up to 52° tilt angles and appropriately labeled. Chemical characterization was enabled by an integrated energy-dispersive X-ray (EDX) detector, with measurements conducted at a 5 mm working distance, 10 kV, and 0.4-0.8 nA. Electron backscattering diffraction (EBSD) analysis was performed at a surface tilt of 70°, with a working distance of 11 mm and electron beam settings of 20 kV and 1.6 nA. Furthermore, the SEM setup included an additional Ga source for focused ion beam (FIB) milling of samples. The FIB, mounted at 52° with respect to the electron beam, was utilized to prepare lamellae for transmission electron microscopy studies in collaboration with the Gemeinschaftslabor für Elektronenmikroskopie (GFE) of the RWTH Aachen.

4 Surface Termination of Silicon

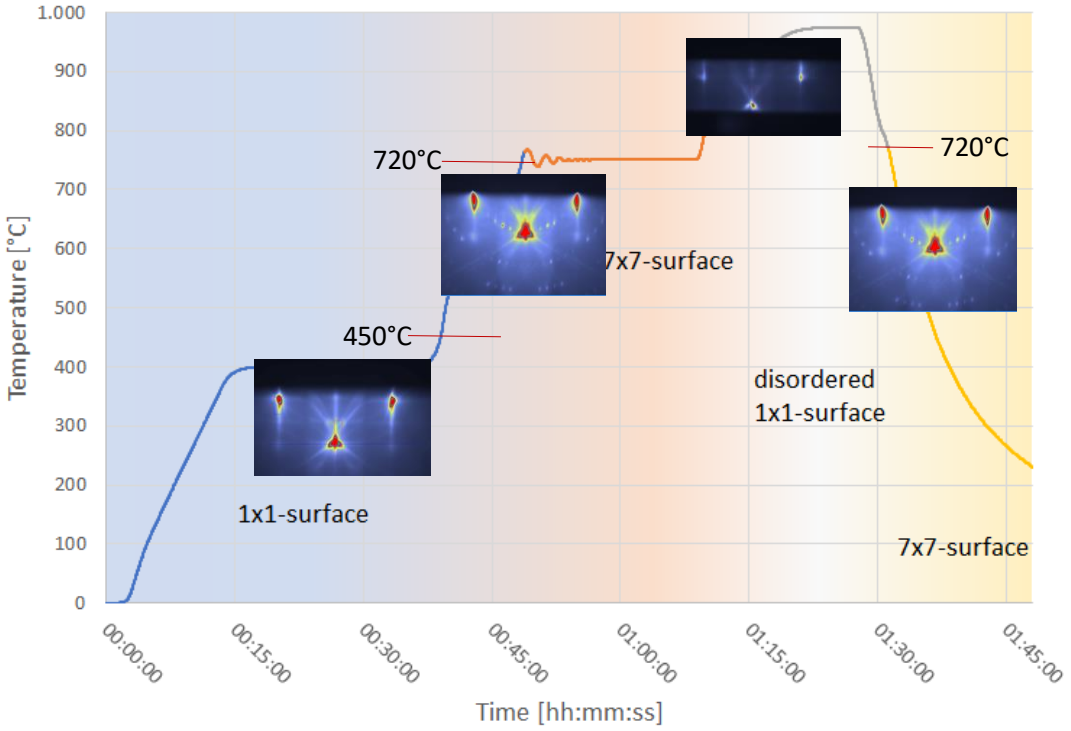

Figure 4.1 Temperature profile for Si(111) surface reconstruction used in Module 5 upon annealing.

The temperature profile of a system is influenced by several factors, including the heating ramp rate of the manipulator, power supply settings, the status of the shutter (open or closed), and the type of substrate (double-side polished or single-side polished). This study focused on preparing substrate surfaces, utilizing a temperature profile outlined in above Figure 4.1.

4.1 Si (111)-1x1-H

The Si(111)-1x1-H surface is based on the unmodified primary surface of silicon, passivated with a monolayer of hydrogen atoms, as illustrated in the atomic arrangements in Figure 4.2. Ideally in this configuration each silicon atom present on the surface is saturated with hydrogen atoms, which means zero dangling bond present on the surface. Two primary methods exist for preparing this surface termination: the most commonly used approach involves HF dipping the silicon substrate (as described in Section 2.6), while an alternative method is exposing the silicon surface to hydrogen ions, such as through a hydrogen atom beam source.[46] The monolayer of hydrogen atoms prevents the silicon surface from oxidation for a short time under a vacuum. However, hydrogen

tends to desorb from the surface upon heating, so thermal processes must be minimized to preserve the hydrogen passivation.[46]

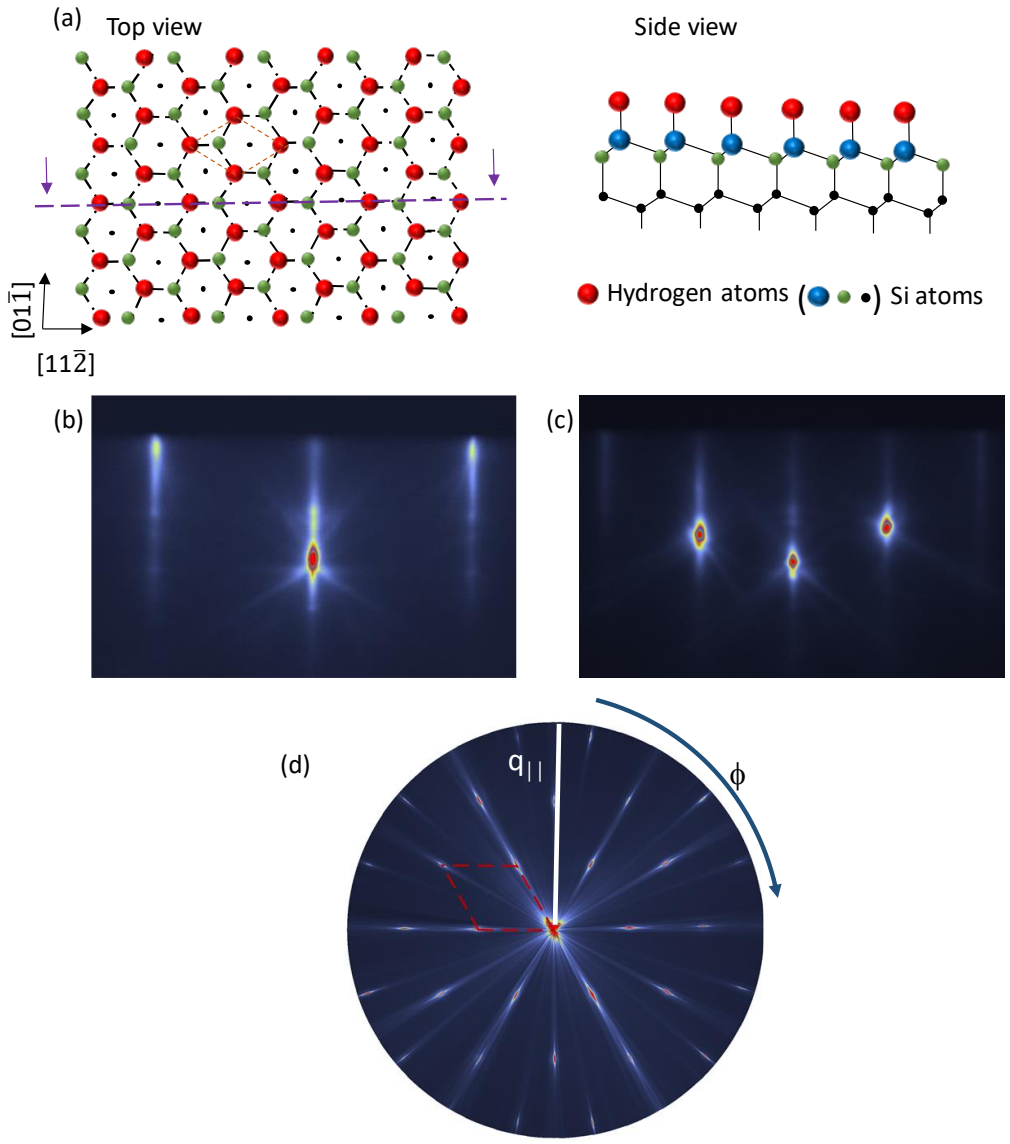

Figure 4.2: Surface of Si(111)-1x1-H is shown in (a) top view, with the red dashed line indicating the unit cell. The side view, projected along the purple dashed line in the top view, shows that each surface silicon atom is saturated with a hydrogen atom. The atomic size indicates the position in Z direction. (b) RHEED pattern of the Si(111)-1x1-H surface measured at a glancing angle of 2.6° using 20 keV electrons, taken in the $[01\bar{1}]$ *direction, and (c) RHEED pattern taken in the* $[11\bar{2}]$ *direction. (d) ARHEED pattern of the Si(111)-1x1-H surface, with the red dashed line marking the 1x1 unit cell. The RHEED patterns (b), (c), and ARHEED (d) were obtained after the sample was dipped in 10% HF for 2 minutes.*

4.2 Si (111)-1x1 surface

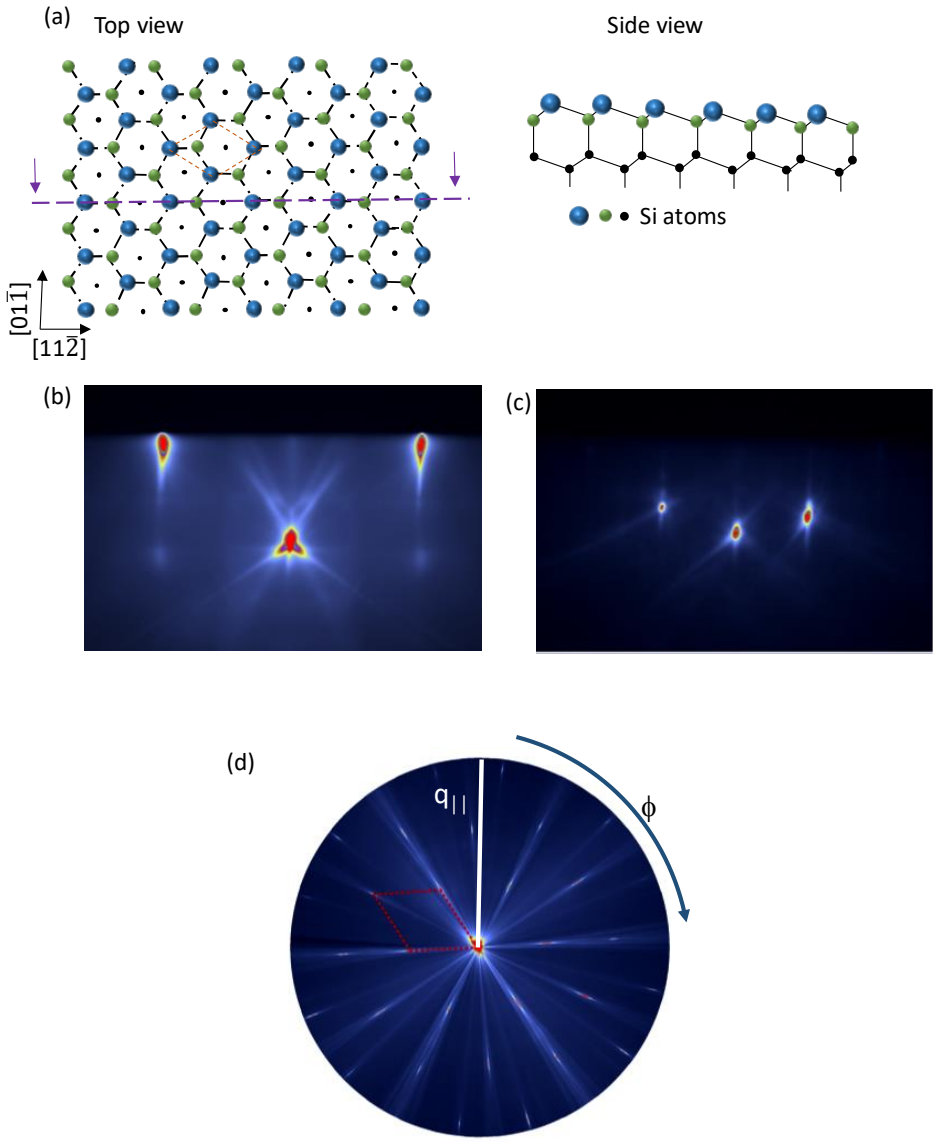

Figure 4.3: Surface of Si(111)-1x1 is shown in (a) top view, with the red dashed line indicating the unit cell. The side view, projected along the purple dashed line in the top view. The atomic size indicates the position in Z direction. (b) RHEED pattern of the Si(111)-1x1 surface measured at a glancing angle of 2.6° using 20 keV electrons, taken in the $[01\bar{1}]$ *direction, and (c) RHEED pattern taken in the* $[11\bar{2}]$ *direction. (d) ARHEED pattern of the Si(111)-1x1-H surface, with the red dashed line marking the 1x1 unit cell.*

The Si(111)-1x1-H and Si(111)-1x1 surfaces share the same primitive unit cell, with the primary difference being the presence of dangling bonds. On the Si(111)-1x1-H surface, these dangling bonds are saturated by hydrogen atoms, whereas the Si(111)-1x1 surface remains unsaturated. Upon heating, hydrogen desorbs from the Si(111)-1x1-H surface, resulting in a surface with one dangling bond per silicon atom. For detailed study on hydrogen desorption from silicon surfaces refer to [47] . In this work, the Si(111)-1x1 surface is obtained by heating the Si(111)-1x1-H surface to 350°C for 30 minutes in the module 5 facility. The optimal temperature is established via continuous monitoring of RHEED, facilitating the removal of hydrogen passivation while preventing surface

reconstruction. The corresponding RHEED pattern is shown in Figure 4.3, with the ARHEED pattern confirming the expected trigonal surface symmetry. As both Si(111)-1x1-H and Si(111)-1x1 share the same (1x1) structure, their RHEED patterns are similar.

4.3 Si (111)-7x7 reconstruction

Scalier and Farnsworth first discovered the Si(111)-7x7 surface structure in 1959, and since then, numerous studies have been conducted on it [48, 49]. The Si(111)-7x7 surface undergoes a complex multi-layer reconstruction aimed at minimizing surface dangling bonds. In 1985, the dimer-adatom-stacking-fault (DAS) model was proposed, providing a comprehensive description of this reconstruction, which involves the rearrangement of the first three atomic layers of the silicon surface.[49]

Figure 4.4 illustrates the detailed atomic arrangements of these three reconstructed layers. The solid blue line marks the 7x7 unit cell. Figure 4.4 (a) shows the bottom layer, consisting of second-layer atoms (yellow) and dimer atoms (light blue), totaling 48 Si atoms, which are closest to the bulk Si(111). Notably, Si atoms along the unit cell edges form dimer pairs (blue atoms). Figure 4.4 (b) depicts the middle layer, composed of first-layer atoms (green) and rest atoms (red), containing a total of 42 Si atoms. The top layer, illustrated in Figure 4.4 (c), consists of 12 adatoms Figure 4.4 (d) combines all three layers, showing a top view of the 7x7 reconstructed surface. The 7x7 unit cell exhibits six-fold (p6mm) in-plane symmetry, in contrast to the three-fold (p3m1) symmetry of bulk Si(111). An additional mirror symmetry line, indicated by a dashed red line in Figure 4.4 (d), bisects the unit cell into two distinct halves: faulted and unfaulted. In the faulted half, the stacking sequence is disrupted, masking the underlying bulk layers. In contrast, the unfaulted half continues the ABC diamond stacking of the substrate. Moreover, the 7x7 reconstruction introduces a level of pseudo-symmetry within the unit cell, adding further complexity to the surface structure.[50]

As its name implies, the Si(111)-7x7 surface has a primitive unit cell that is seven times larger than that of the Si(111)-1x1 surface. Furthermore, compared to the 1x1 surface, the 7x7 reconstruction reduces the number of dangling bonds by 38%, with only 19 atoms providing dangling bonds out of the 49 surface atoms. Each adatom, rest atom, and corner hole contributes one dangling bond, which plays a significant role in the surface's unique properties.

The Si(111)-7x7 reconstructed surface is achieved by heating the substrate immediately after an HF dip. Based on the temperature profile of module 5 (Figure 4.1) and observations using RHEED, surface rearrangement begins around 450°C and the complete 7x7 reconstruction forming between 720°C and 850°C. At approximately 860°C, the surface atoms reorder, leading to the formation of a distorted Si(111)-1x1 structure. During this process, carbon contamination may occur, leading to the formation of SiC, which can be detected via RHEED. SiC can be effectively removed by flashing the substrate at around 975°C.

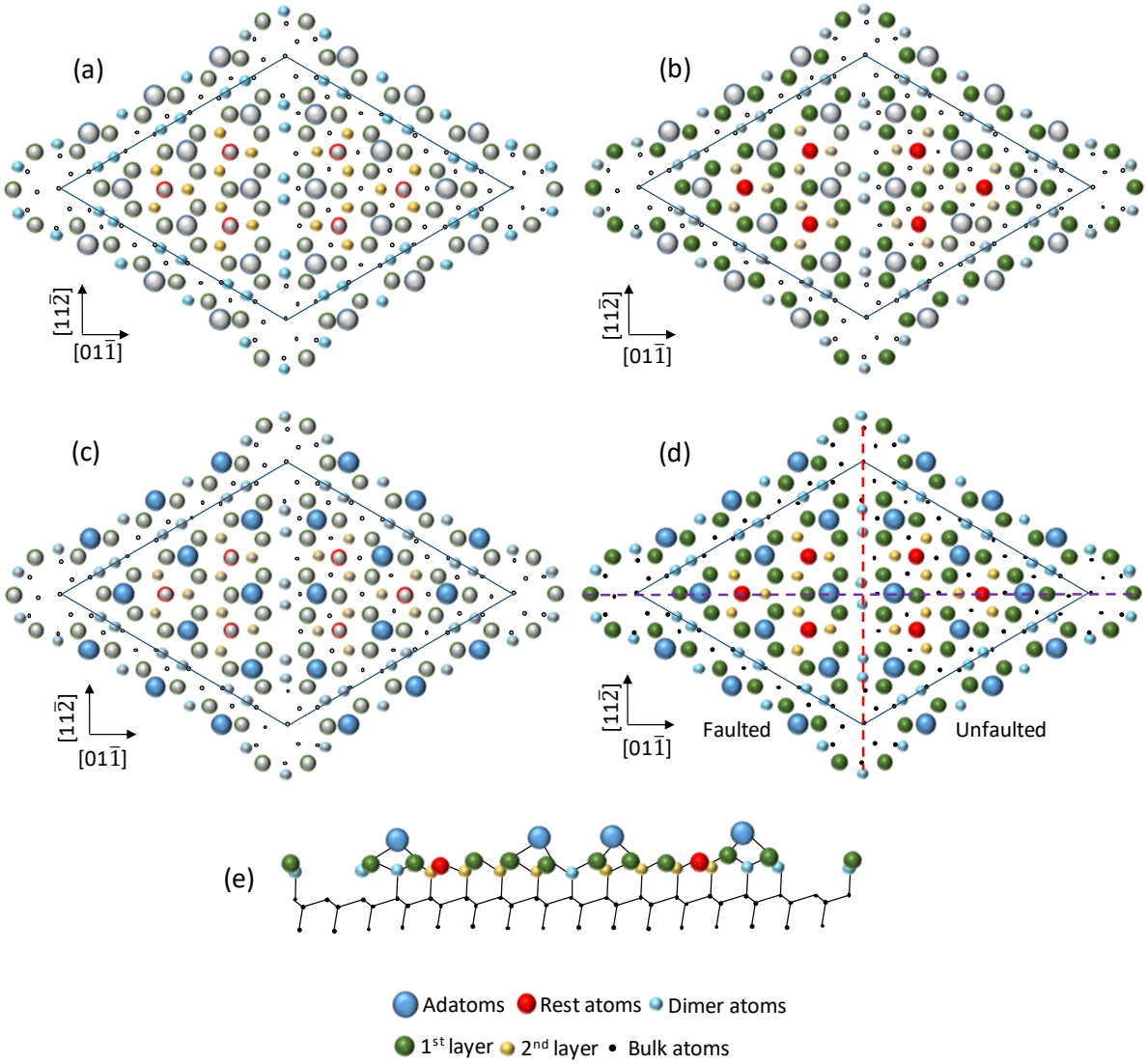

Figure 4.4: The Si atom position in the Si(111)7x7 reconstructed unit cell. The atomic size indicates the position in Z direction. Top view; (a) shows the bottom atomic layer which is closest to the bulk Si(111), consist of 48 Si atoms (indicated as blue dimer atoms and yellow).(b) shows middle atomic layer which has 42 Si atoms (follow atoms color with green and red). (c) shows the top layer consist only of 12 Si adatom in unit cell. (d) shows the all layers combined in top view of Si(111) 7x7 unit cell, which has an extra mirror symmetry line from cutting the cell into two halves (faulted/unfaulted). The mirror line, shown as a dashed red line, cuts the in-plane unit cell area into two triangles, in the in-plane diagram. (e) shows the side view of a unit cell, is a projection along the dashed purple line in (d). This atomic model is based on DAS (dimer, adatoms, stacking fault). Redrawn from[46]

The disordered 1x1 surface is used as a temperature calibration point in this study. As the substrate cools from 975°C, the surface passes through the temperature range conducive to 7x7 reconstruction. Once formed, the 7x7 surface remains stable even during further cooling and has been observed to remain stable in UHV condition for at least one week. The RHEED and ARHEED patterns of the Si(111)-7x7 reconstructed surface, as shown in Figure 4.5, are clearly distinct from those of the Si(111)-1x1 surface. In Figure 4.5, the side view illustrates the rearrangement of several

atomic layers. However, RHEED tends to average the first few monolayers, which accounts for the brighter appearance of the 1x1 reflexes compared to the additional reflexes.

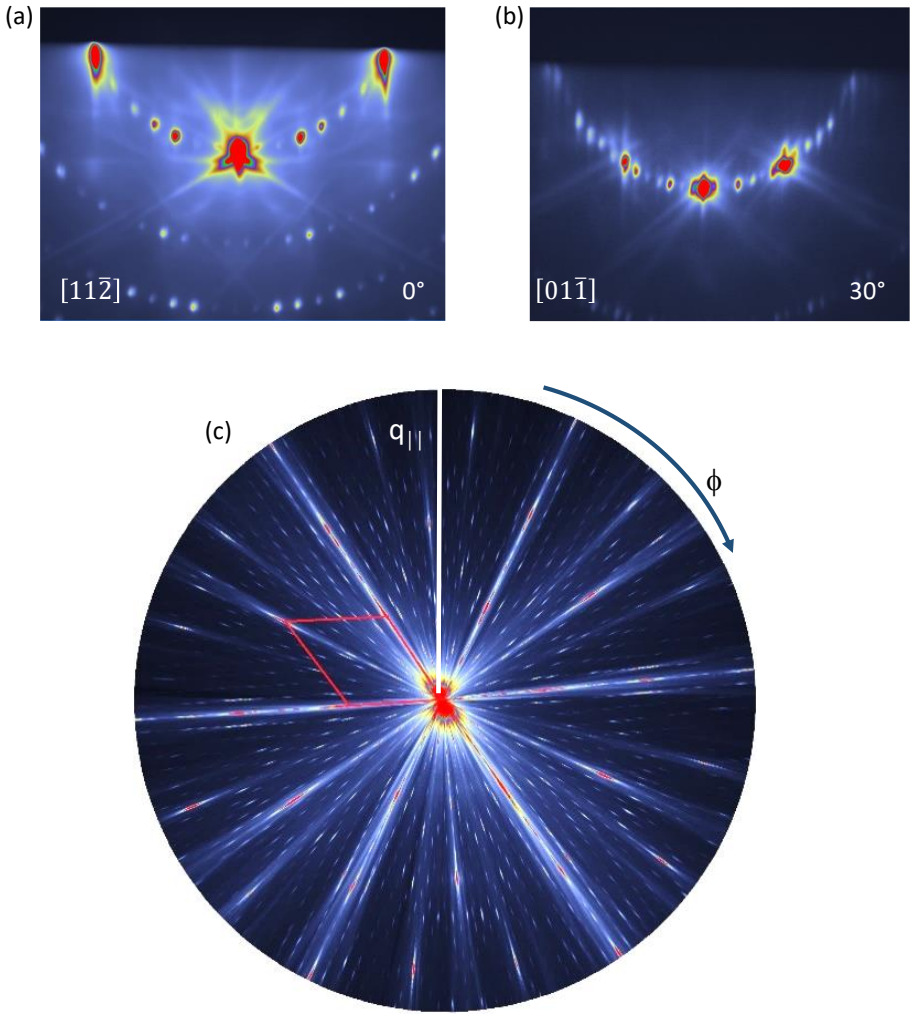

Figure 4.5: RHEED pattern from a Si(111)-7x7 surface measured at a glancing angle of 2.6° using 20 keV electrons. (a) RHEED pattern taken in $[11\bar{2}]$ *direction and (b) RHEED pattern taken in* $[01\bar{1}]$*.(c) ARHEED of Si (111)-7x7 surface and the dashed red line indicates the unit cell of 1x1.*

4.4 Si (111)-(√3×√3)R30°-Sb surface

Surfactant-mediated epitaxy introduces foreign atoms, known as surfactants, to the surface of a growing film to influence the growth process. These foreign atoms, distinct from the growing film and substrate, must remain on the surface without dissolving into the film. Surfactants modify the surface free energy by passivating surface dangling bonds, enabling control over growth kinetics and thermodynamics. This technique allows for manipulation of thin film growth modes, enhancing two-dimensional (2D) layer-by-layer growth while also controlling the growth direction, suppression of twin formation, and preventing inter-diffusion. The general phenomenon of the surfactant in epitaxy is that surfactant atoms saturate the surface dangling bonds and passivate the surface chemically.

Group III, IV, and V elements as surfactant on the Si(111) surface are well-studied, often forming covalent systems with specific adsorption structures.[51] Group V adatoms like Bi and Sb exhibit a "milkstool" model, where both monomer and trimer structures are observed. STM studies reveal that adatom coverage influences these structural formations, and semiconducting properties.[52] There are multiple approaches for passivating silicon surfaces using antimony (Sb). Park et al. has provided a detailed study of the coverage of antimony on Si(111). When Sb is deposited on a Si(111)-7×7 reconstructed surface under specific conditions, various passivated surface terminations, such as (√3×√3)R30°-Sb, (5√3×5√3)R30°-Sb, and 2×2, can be achieved.[53] These surface structures are formed by exposing the Si(111)-7×7 surface to Sb at different substrate temperatures, as illustrated in Figure 4.6. The antimony coverage on the Si(111) surface depends on the surface temperature, with a monolayer forming within the temperature range of 580°C to 720°C. At these temperatures, further growth of Sb is hindered due to the high substrate temperature. The bond length between Sb and Si (2.47 Å) is significantly shorter than that of Sb-Sb (2.92 Å), reflecting the stronger bonding energy of Sb-Si. As a result, the formation of a complete monolayer of Sb is feasible within this temperature range.

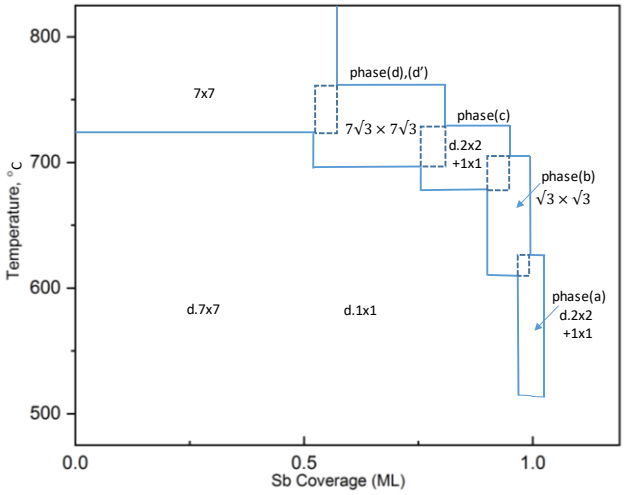

Figure 4.6 Two-dimensional "phase diagram" shows the Antimony coverage on Si substrate with relevant surface temperatures. Two stable Sb terminated surfaces are Si(111-(5√3×5√3)R30°-Sb and Si(111)-((√3 x √3) R30°-Sb. Redrawn from [53]

The temperature profile given in Figure 4.7 is followed to prepare Si(111)-(√3×√3)R30°-Sb surface in the facility module 5 used. After the HF dip, the Si surface is heated to 400° C to desorb the hydrogen passivation and to 850°C for a stable 7x7 reconstruction. It is further heated to 975°C to remove SiC impurities. Until this point, the temperature profile is the same as mentioned for the 7x7 reconstructed surface. While cooing down the sample from 800°C, an antimony flux of 9.6 X 10^{-8} mbar is exposed until the characteristic reflexes of this surface termination appear as shown in Figure 4.8. Typically cooling rate is 0.3°C/s. Temperature profiles remain the same irrespective of the Sb cracker cell or effusion cell used for termination in this work. The RHEED and ARHEED patterns of the Si(111)-(√3 x √3) R30°-Sb terminated surface are shown in Figure 4.8, which reveals a reflex pattern which is significantly different from the Si(111)1x1 and Si(111)7x7 surfaces.

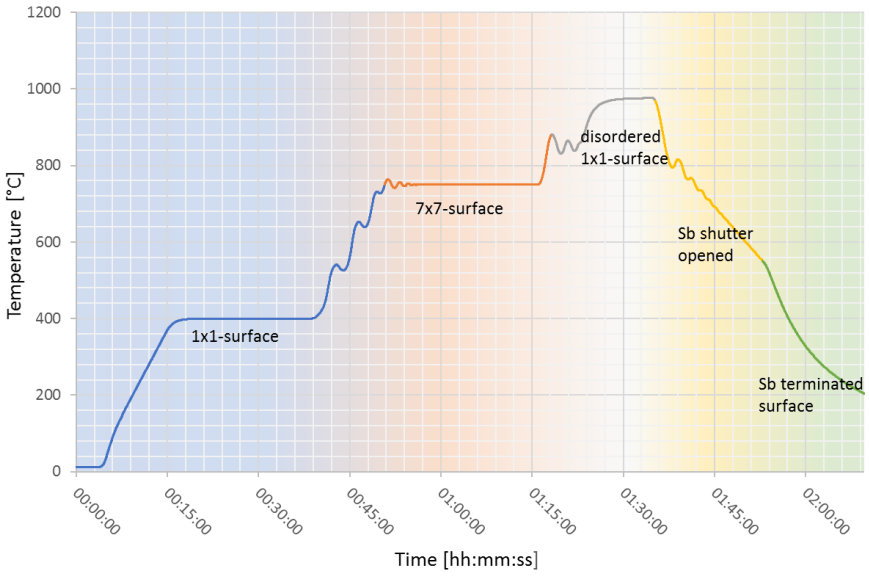

Figure 4.7: Temprature profile of manipulator to obtain passivating Si(111) surface with antimony.

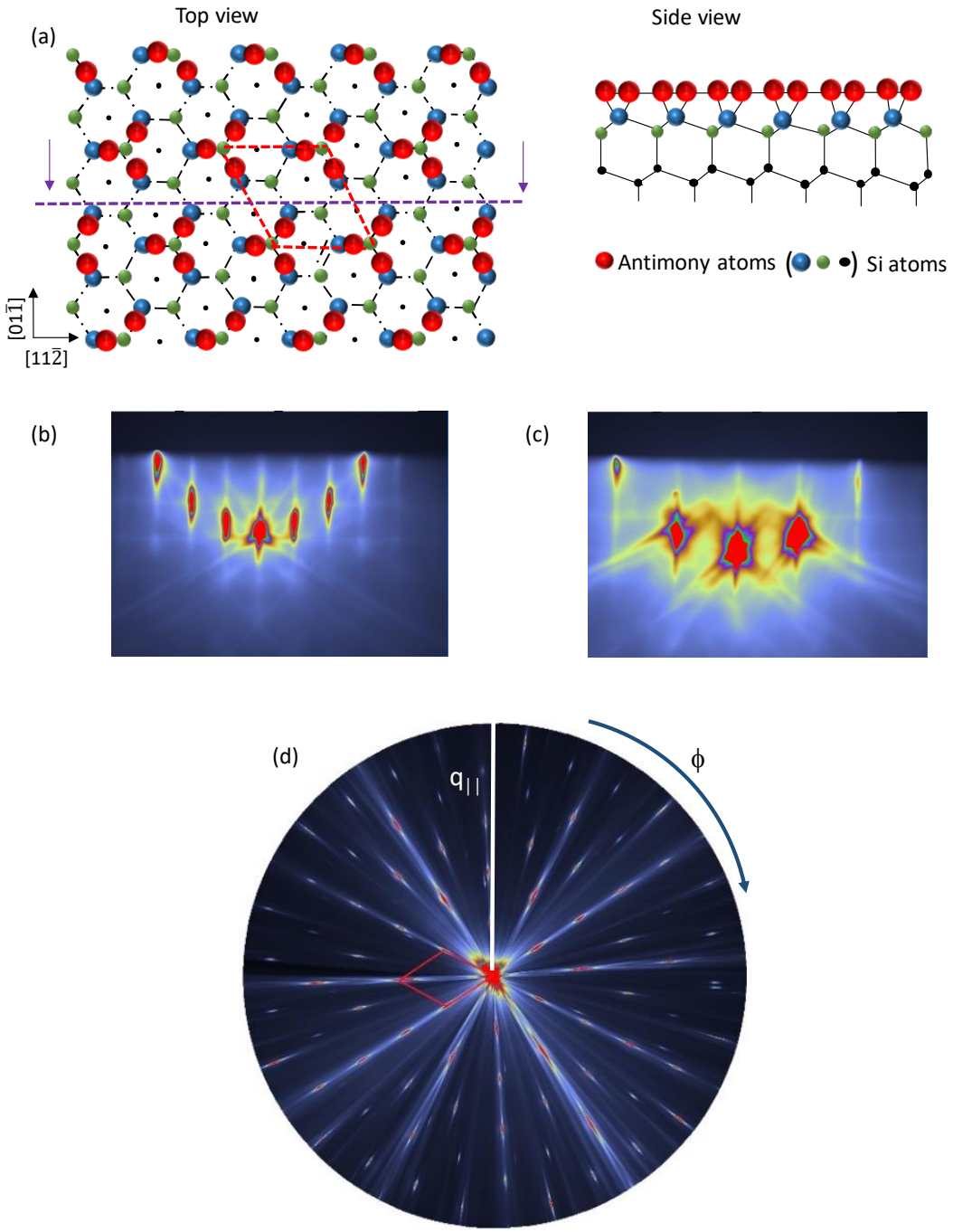

Figure 4.8: (a) shows the top view of the Si(111)-(√3×√3)R30°-Sb surface with the red dashed line indicating the unit cell and cut along the purple dashed line shown as a side view. The size and color indicate the position in the z-direction. Redrawn from *[54]*. RHEED pattern from a Si(111)-(√3×√3)R30°-Sb surface measured at a glancing angle of 2.6° using 20 keV electrons. (b) RHEED pattern taken in $[\bar{2}11]$ direction and (c) RHEED pattern taken in $[\bar{1}10]$. (d) ARHEED image of Si(111)-(√3×√3)R30°-Sb surface, with the unit cell indicated by the red line.

4.5 Si-1x1 Te

A Si(111)-1x1-Te termination is also (rarely) discussed in the literature. F. Lüpke et al. have reported that the tellurium termination can be created on the Si(111)-1x1 surface. It is even possible to suppress twin domains of Bi_2Te_3 in a defined temperature range.[55] However, there are challenges in the preparation of this surface. It is important to note that like the Sb-passivation, Te also dopes the silicon, resulting in a changing conductivity at the surface.[28] It is observed with RHEED that the surface termination is unstable; it requires a constant tellurium flux. Secondly, it is not possible to directly distinguish the RHEED pattern of the pure 1x1 termination and the tellurium terminated surface. Si (111)-1x1 and Si(111)-1x1-Te share the same lattice parameter, and the position of the reflexes are identical. The sample process according to section 2.6 and followed by heating at 350°C to desorb the hydrogen passivation. Prior to growth a Te flux of 1.7 x 10^{-8} mbar is exposed until the characteristic specular spot intensity changes as shown in Figure 4.9.

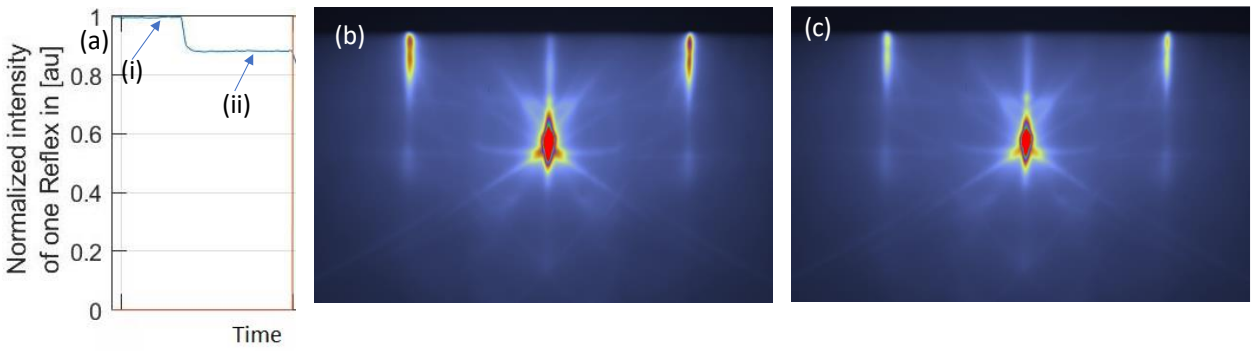

Figure 4.9: The decrease of the intensity by forming a tellurium termination is shown. a) shows the change in intensity of the specular spot. At the beginning the intensity is 100%, which is from 1x1 surface as shown in b) as a RHEED picture in $[\bar{1}10]$ direction. As the shutter of the tellurium cell opens, the intensity drops to approximately 90%, as can be seen in the plot and in c) in the RHEED picture in $[\bar{1}10]$ direction.

5 Thin film growth of IV-VI mono chalcogenides

This chapter presents a detailed investigation into the thin-film growth of chalcogenides, specifically GeTe, SnTe, and SnSe, with a focus on understanding the influence of substrate termination on epitaxial growth. Thin films of GeTe, SnTe, and SnSe were deposited on various Si(111) surfaces, including the 1x1 surface, the 7x7 reconstructed surface, and the (√3×√3)R30°-Sb terminated surface. The growth process was closely monitored and controlled using in-situ RHEED and ARHEED analysis, while further characterization was carried out using X-ray Diffraction (XRD), ϕ-scans, Anomalous RHEED (ARHEED), and Scanning Electron Microscopy (SEM). These techniques provided comprehensive insights into the crystallinity, orientation, and surface morphology of the grown films.

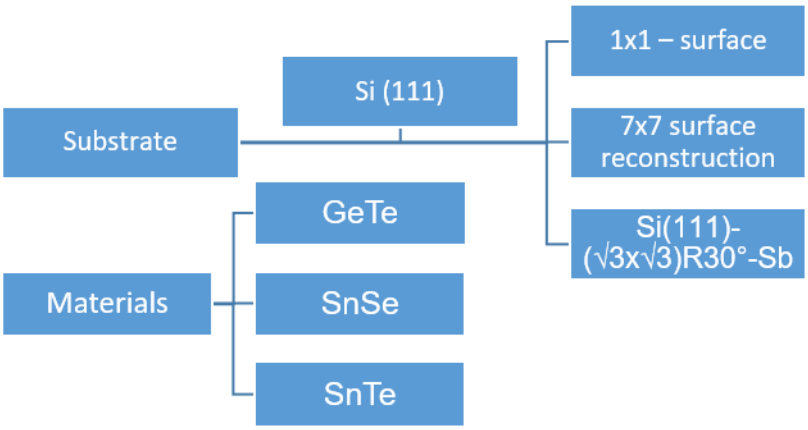

Figure 5.1The flowchart represent materials and surfaces studied in this chapter.

5.1 GeTe

Since the late 1960s, germanium telluride (GeTe) has attracted considerable attention for its fundamental properties and wide range of technological applications, notably as a thermoelectric[56], ferroelectric [57], and phase-change material [2]. The discovery of a pronounced Rashba effect in GeTe has further positioned it as a potential candidate for spintronic devices.[58] The phase transition from amorphous to crystalline GeTe results in a significant change in electrical resistance, with a high crystallization temperature of 170°C and a melting point of 725°C, marking it as a stable phase change material (PCM). [59] While the characteristics of amorphous and crystalline GeTe, including bond length, bonding properties, and electronic structures, have been extensively studied, several key aspects, particularly in thin films, remain unresolved. Wang et al. have investigated GeTe growth on Si(111) surfaces, highlighting that the crystallization behavior is strongly dependent on both the film thickness and the surface treatment of the silicon substrate.[32, 50] Density Functional Theory (DFT) calculations reveal a pronounced shift in bonding in ultrathin GeTe films compared to the bulk phase, with significant differences in dielectric constant ($\varepsilon\infty$)and Born effective charge (Z*), indicating a change in the bonding mechanism.[60] GeTe is part of a family of materials characterized by an unconventional bonding mechanism, involving half-filled p-bands and a delicate balance between electron localization and delocalization. [7] It occupies a position within the metavalent bonding region on the 2D Map of electronic interactions and bonding. Hence, it would be interesting to experimentally investigate the confinement effect; how the crystal structural variations with film thickness influence its positioning on this map, which could provide valuable insights into its properties and bonding characteristics.

5.1.1 Crystal structure of GeTe :

GeTe typically exists in two structural forms: the trigonal (hexagonal) structure and the rock salt (cubic) phase, similar to NaCl. The cubic description with slight distortion is commonly used in literature for GeTe. This thesis examines the α phase of GeTe. The structure of crystalline GeTe can be described by the rhombohedral R3m unit cell as shown in Figure 5.2. GeTe exhibits a temperature-dependent phase transition. The angle between the axes of the unit cell vectors shifts from 88.17° at 295 K to 89.97° at 716 K. At approximately 720 K, the crystal structure transitions from hexagonal (space group: R3m) to cubic (space group: Fm3m). At room temperature, it is observed that GeTe has a simple rhombohedral distorted NaCl-type crystal structure with the space group R3m.[61, 62]. GeTe's rhombohedral structure is a result of a slight Peierls distortion, where the Ge and Te atoms shift along the [111] direction. This causes a variation in bond lengths, creating three shorter and three longer bonds for each Ge-Te pair.

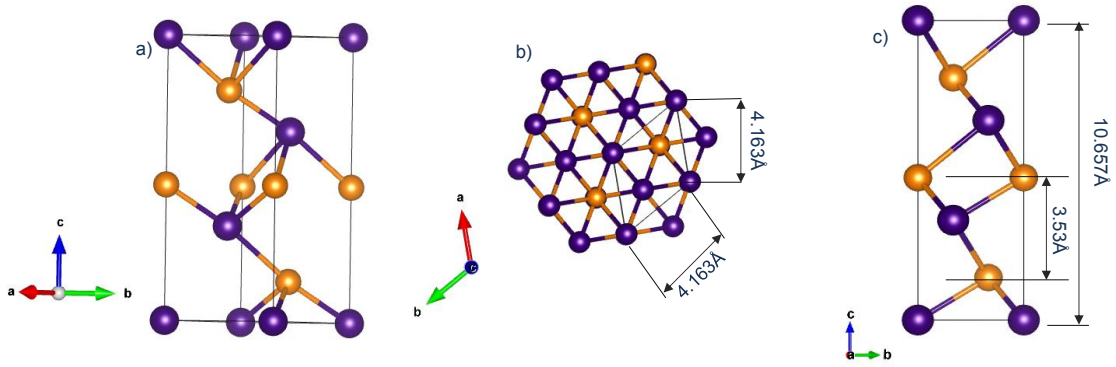

Figure 5.2: Structure of GeTe with hexagonal description is demonstrated. Ge atoms in Yellow and Te in Blue. Structure pictured by VESTA.[63]

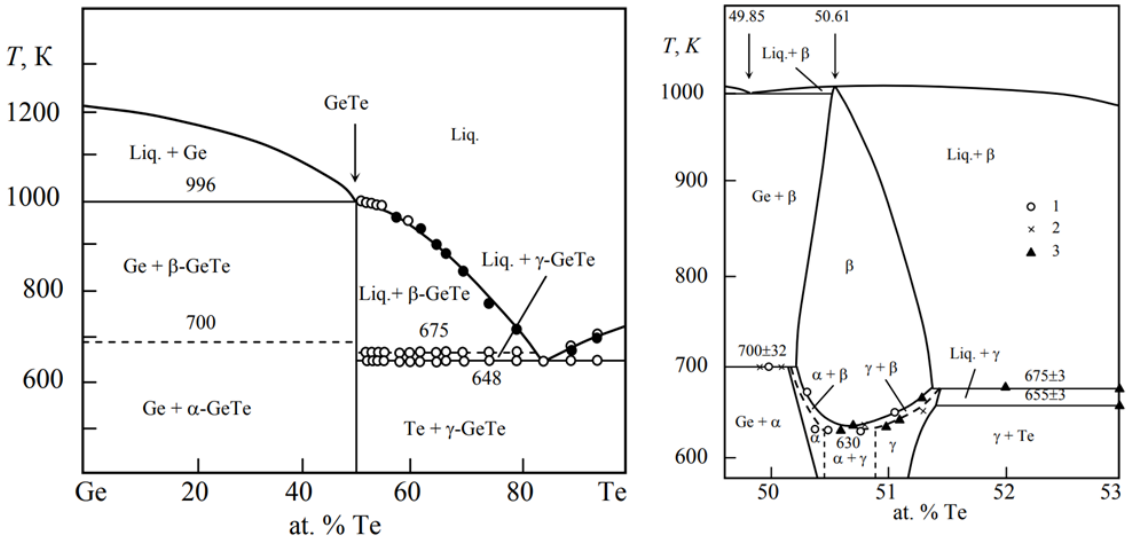

Figure 5.3: Phase diagram of GeTe shows three phases existing at high temperatures. Pure GeTe with a ratio of 50:50 does not exist. Taken from.[64]

5.1.2 Growth of GeTe:

The epitaxial deposition of GeTe on a silicon substrate via MBE has first been reported in 2012 by Giussani et al. [65] They demonstrated epitaxial growth on a reconstructed Si(111)-7x7 substrate. The GeTe thin film was grown in a Te-rich environment, with a flux ratio of nearly 0.4 and growth rates ranging from 3 to 8 pm/s. This condition is in line with the phase diagram which indicates that the Te-rich phase is favorable for GeTe formation (see Figure 5.3). Although, the lattice mismatch is nearly 8.5%, a highly textured crystalline film of GeTe grows in the (0001) direction, aligning its high symmetry in-plane directions with the ones of the Si(111) substrate, α - GeTe $[10\bar{1}0]||[11\bar{2}]$ and α

- GeTe $[10\bar{2}0]||\ [1\bar{1}0]$. They observed a transition from amorphous to crystalline GeTe at the early stage of growth via RHEED. A similar phenomenon was reported by Wang et al in 2017 during the growth GeTe growth on Si(111) 1x1- H passivated surface. However, unlike the Si(111)-7x7 reconstructed surface and the Si(111) 1x1–H surface, the growth of GeTe on the Si(111)-(√3×√3)R30°-Sb terminated surface shows a significant difference.[60] This effect is studied in detail in this work; (Chapter 6). Giussani et al. and Wang et al. further reported that GeTe films grown on Si(111)-7x7 reconstructed surfaces exhibited in-plane twisted domains at ±2.5° and ±7° relative to the central peak. This effect was attributed to domain-matched coincidence lattice formation. In contrast, GeTe films grown on Si(111)-(√3×√3)R30°-Sb terminated surfaces showed significantly reduced twinned and rotational domains, highlighting the importance of surface preparation for optimizing GeTe growth. These observations are crucial to note in order to optimize the growth condition of GeTe on Si(111) surfaces and obtain reproducible thin film study. In this study, the growth conditions of GeTe have been optimized on three surfaces: the Si(111) 7x7 reconstructed surface, the Si(111) 1x1 surface, and the Si(111)-(√3×√3)R30°-Sb terminated surface.

From an experimental setup point of view, the growth temperature can vary between MBE chambers due to differences in thermocouple placement, substrate manipulators, heater configurations, effusion cell distances, and chamber size. However, the relative error or offset remains constant within the same chamber. While absolute temperatures may differ between systems, relative temperature consistency within the same chamber allows for reproducibility across multiple samples. In this study, the temperature profile specific to Module 5 is detailed in Chapter 4. In addition to surface reconstruction, the Ge/Te flux ratio plays a crucial role in the epitaxial growth and reproducibility of GeTe films, as noted by both Giussani et al. and Wang et al. In this study, Ge and Te effusion cells are heated to 1100°C to 1121°C and 240°C to 260°C, respectively, resulting in a growth rate range of 0.03 to 0.08 Å/s with a substrate temperature range of 115°C to 170°C, depending on the surface under study. Well-cleaned Si substrates are used for growth studies, and the substrate preparation process is already covered in Chapter 2. Upon completion of GeTe thin film growth, the samples were immediately capped with an Al_2O_3 layer for ex-situ analysis, without breaking the vacuum. This was achieved using a dedicated oxide-MBE system with a base pressure of 4×10^{-10} mbar. Al_2O_3 was deposited from an electron-beam evaporator at a rate of 0.1 Å/s, with the pressure raised to 2×10^{-7} mbar during evaporation. The sample was rotated at 6 rpm to ensure uniform film deposition.

5.1.3 Analysis of GeTe growth

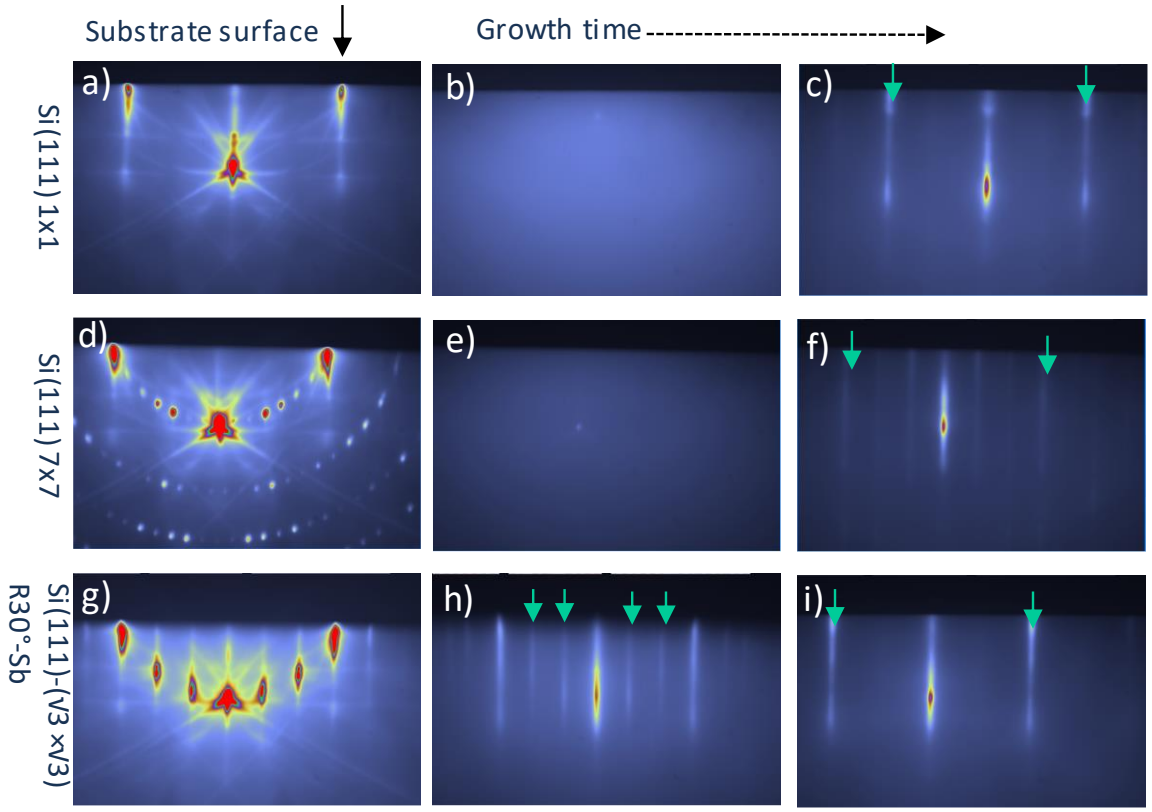

Figure 5.4: RHEED images (a) Si(111)-1x1 surface taken in $[\bar{1}10]$ direction. (d) Si(111)7x7 reconstructed surface and (g) Si(111)-(√3 ×√3)R30°-Sb terminated surface taken in $[\bar{2}11]$ direction. GeTe growth on respective surfaces are shown in images (b,c,e,f,h,i).

The most significant stages of the epitaxial GeTe growth on Si (111) surfaces are captured by sequential in-situ RHEED images shown in Figure 5.4. The RHEED image (Figure 5.4 (a)) shows the Si(111) 1x1 surface prior to the growth in the $[\bar{1}10]$ direction. As growth proceeds, atoms start attaching to the surface which leads to fading out of the substrate reflexes, and only the diffusively scattered intensity of the specular spot remains, as shown in Figure 5.4 (b). No reflexes are observed on the RHEED screen for nearly 1.4 nm deposition. This RHEED pattern resembles an amorphous phase diffraction pattern described in the literature.[60] It is clear that no crystalline GeTe is formed up to this point, the surface is covered by an amorphous material instead. Above a critical thickness, new reflex streaks appear instantly, which correspond to the GeTe (0001) (See Figure 5.4 (c)). The nearly 8.5% lattice mismatch between GeTe and Si allows the RHEED reflections from both materials to be easily distinguished. The sharp streak indicates crystalline growth with a flat surface. This observation is consistent with the findings of Wang et al. In this study, the thickness-dependent amorphous to the crystalline phase transition is referred to as "Blackout". In addition, the critical thickness of blackout is affected by surface temperature, as explained further in Chapter 6.

Similarly, an intermediate amorphous phase is observed on the Si(111)-7x7 reconstructed surface (see Figure 5.4 (e)). The reflexes of the Si(111)-7x7 surface, recorded in the $[\bar{2}11]$ direction prior to GeTe deposition, are shown in Figure (d). During the early stages of GeTe deposition, the material

initially deposits in an amorphous phase. Upon reaching a critical thickness of nearly 2 nm, a rapid phase transition to a crystalline state is observed. This phase transition is marked by the immediate appearance of reflexes on the RHEED screen, as illustrated in Figure (f). The inner two streaks are indicative of the presence of rotational domains. This observation is in agreement with the results of Giussani et al. [65] The deposition on the Si (111) -(√3 ×√3)R30°-Sb surface shows immediate crystalline growth of GeTe, which significantly differs from the growth on the Si(111)-1x1 surface and the Si(111)-7x7 reconstructed surfaces. Figure (g) shows the RHEED image of the Si (111) -(√3 ×√3)R30°-Sb surface prior to the growth in the $[\bar{2}11]$ direction. As growth proceeds on this surface, immediate reflexes of GeTe appear (see Figure h). It is interesting to note that the additional streaks are visible till a film thickness of 2.2 nm, which in literature is explained as consequence of the GeTe(0001)-(√3 ×√3)R30° reconstruction. After deposition of 2.2 nm of film thickness, no additional reflexes are observed and reflexes remains stable till the end of the growth Figure (i). The sharp streaks observed in the RHEED patterns confirm the formation of a smooth, well-ordered GeTe film on all three silicon surfaces.

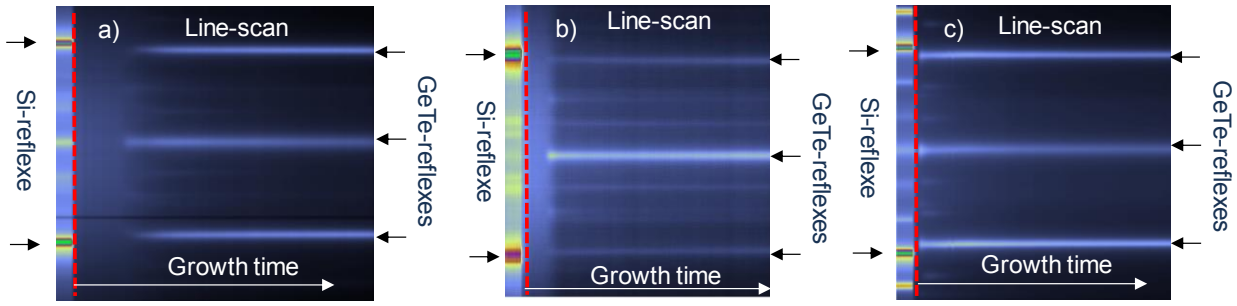

Figure 5.5: RHEED line scans of GeTe growth on (a) Si(111)-1x1 surface, (b) Si(111)7x7 reconstructed surface, (c) Si(111)-(√3 ×√3)R30°-Sb terminated surface are taken in $[\bar{1}10]$ *direction.*

Further, the interface of the substrate and GeTe film surface is shown with the dashed red line in line scan Figure 5.5. The interface of Si(111)-1x1 surface and Si(111)7x7 reconstructed surface shows initial blackout and after critical thickness of film, the growth mode remains unchanged. It is clearly visible that multiple streaks start to appear right from the amorphous-to crystalline transition on the 7x7 reconstructed surface and remain constant throughout the growth shown in Figure 5.5 (b). However, additional inner streaks are also present in film growth on Si(111)-1x1 surface (see Figure 5.5(a)) and on Si(111)-(√3×√3)R30°-Sb terminated surface (see Figure 5.5(c)), which are changing with film thicknesses, indicating changes in epilayer alignment.

XRD and SEM measurements are taken for thicker films to understand the film quality. For GeTe samples, measurements are performed in collaboration with RWTH Aachen team members Dr. Marc Pohlmann and M.Sc. Peter Kerres. It is confirmed through XRD θ-2θ scans that the highly textured GeTe growth in (000L) direction is achieved on Si(111) surfaces. XRD θ-2θ scan is shown in Chapter 6. More details on techniques can be found in collaborative dissertation of M.Sc. Peter Kerres. To understand the presence of domains in the film ARHEED and Phi scans are performed.

To investigate the in plane alignment of rotational domains, the GeTe $(01\bar{1}2)$ peak was investigated using a ϕ Scan. Figure 5.6 presents the ϕ scan measurements, which confirm that GeTe films maintain epitaxial relation on all three surfaces studied. The growth on each surface reveals two distinct rotational domains, which can be explained by the trigonal symmetry of the crystal. These two domains form a Σ3 grain boundary and are commonly referred to as twins. For GeTe films grown on both the Si(111)1x1 and Si(111)-(√3 × √3)R30°-Sb surfaces, one of these domains aligns perfectly with the Si(111) planes, while the other is rotated by 60° in-plane. The intensity of the peak can be considered proportional to the area occupied by the respective domain in the film. In the linearly scaled plot, the intensity ratio of twin domains indicates the suppression of the one domain. In the case of GeTe grown on a Si(111)1x1 surface, the twinned domain contribution is 14%, while on the Si(111)-(√3 ×√3)R30°-Sb surface, twinned domains contribute only 9%, which means that the twinning is strongly suppressed on the Si(111)-(√3 ×√3)R30°-Sb surface. In the case of GeTe growth on the 7x7-reconstructed substrate, a part of twin domains, the additional twisted domains are observed at ±2.4° and ±7.3° relative to the central peak. It is important to note that central domain is aligned with the Si substrate (111) planes The large lattice mismatch between the epilayer and substrate, along with the differences in an in-plane mirror symmetry, likely contributes to the formation of these additional rotational domains, a phenomenon related to domain-matching epitaxy.[32] Concerning the in-plane alignment, GeTe growth on all three surfaces is consistent with literature.[32, 65, 66]

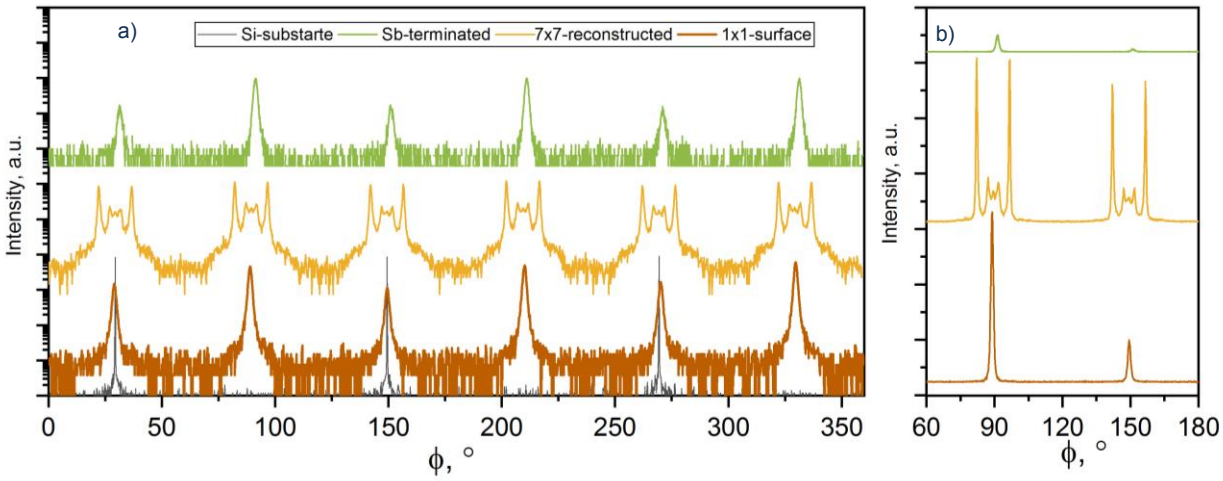

Figure 5.6: The plots show ϕ- scans of GeTe. The Green, Yellow and Brown line show the $(01\bar{1}2)$ peaks of GeTe, deposited onto a Si(111)-(√3x√3) R30°- Sb terminated, 1x1-surface and 7x7-reconstructed substrates respectively. The black line shows (111) peaks of Si. The measurements are shown on a logarithmic scale (a) to emphasize smaller domains and to pronounce the intensity ratios between the different domains plotted in normalized linear scale (b).

It is clear from the ϕ scan that the twin domains are present for all three surfaces. To investigate the domains further, ARHEED scans are performed at the end of each film growth, when the substrate temperature was ramped down to room temperature. The ARHEED pattern of a GeTe film grown on the Si(111)-1x1 surface and on the Si(111)-(√3x√3) R30°- Sb terminated surface shows the six reflexes, each being rotated by 60° in Figure 5.6. These six reflexes are corresponding to the two domains formation on both the surfaces, or also can be seen as hexagonal surface. It is evident that

the GeTe film aligns its high symmetry in-plane directions with the high-symmetry directions of the substrate, namely: GeTe$[\bar{1}10]||$Si$[\bar{1}10]$and GeTe$[11\bar{2}]||$Si$[11\bar{2}]$. The two high symmetry directions $[11\bar{2}]$and $[\bar{1}10]$ of deposited GeTe film on Si(111) surfaces are indicated with arrow in Figure 5.7 (a) and (b). The GeTe growth on Si(111)1x1 surface and Si(111)-(√3×√3)R30°-Sb surface, a 1× reconstruction along $[11\bar{2}]$direction and 1× reconstruction along the $[\bar{1}10]$ direction are present in thicker films (~30 nm). Nevertheless, it is observed that these surface reconstructions are dependent on film thickness as well as substrate temperature.

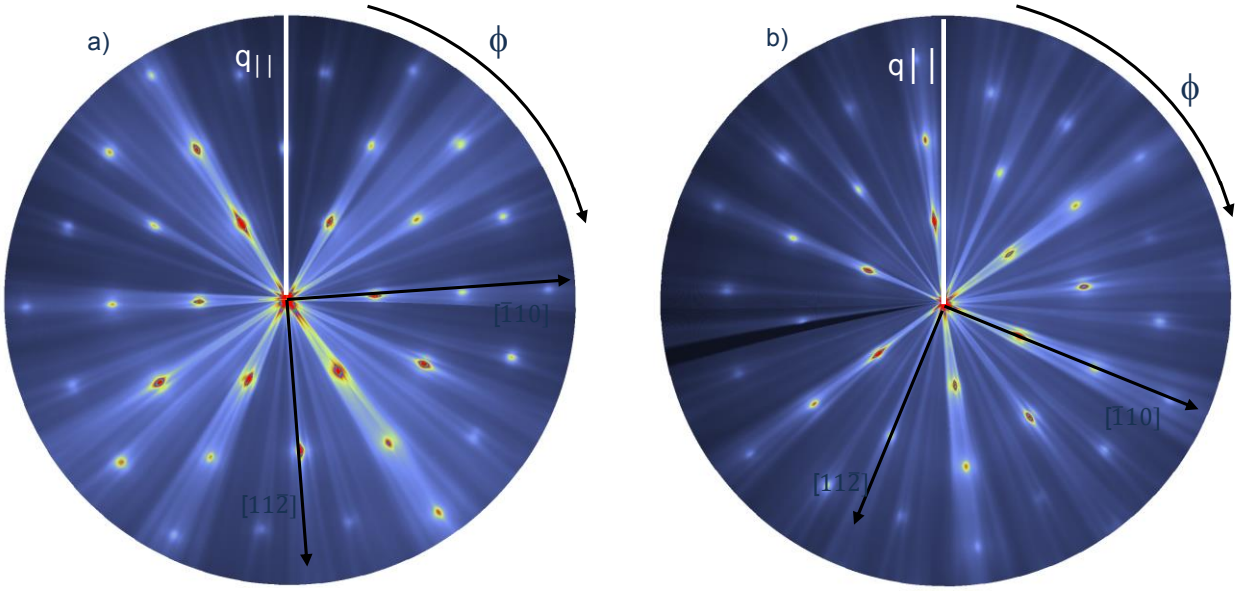

Figure 5.7: ARHEED scans taken at the end of the GeTe film growth on (a) Si(111)1x1 surface and (b) Si(111)-(√3 ×√3)R30° Sb terminated surfaces.

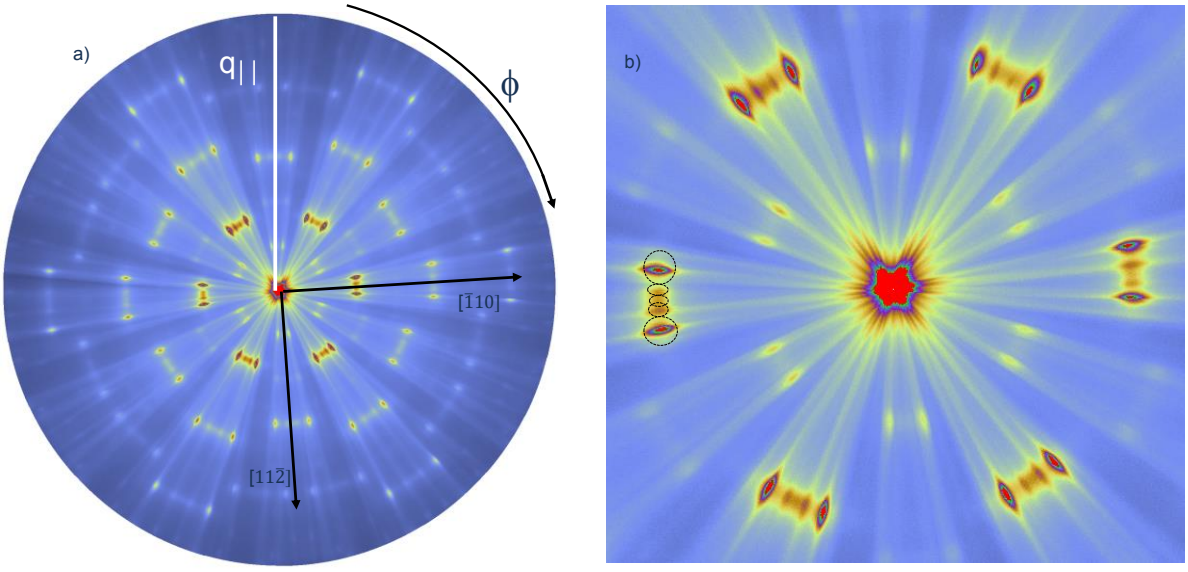

Figure 5.8: ARHEED scans for GeTe growth (a) on Si(111) 7x7 reconstructed surface and (b) zoomed view of the inner circle reflexes which shows rotational domains with 5 prominent spots.

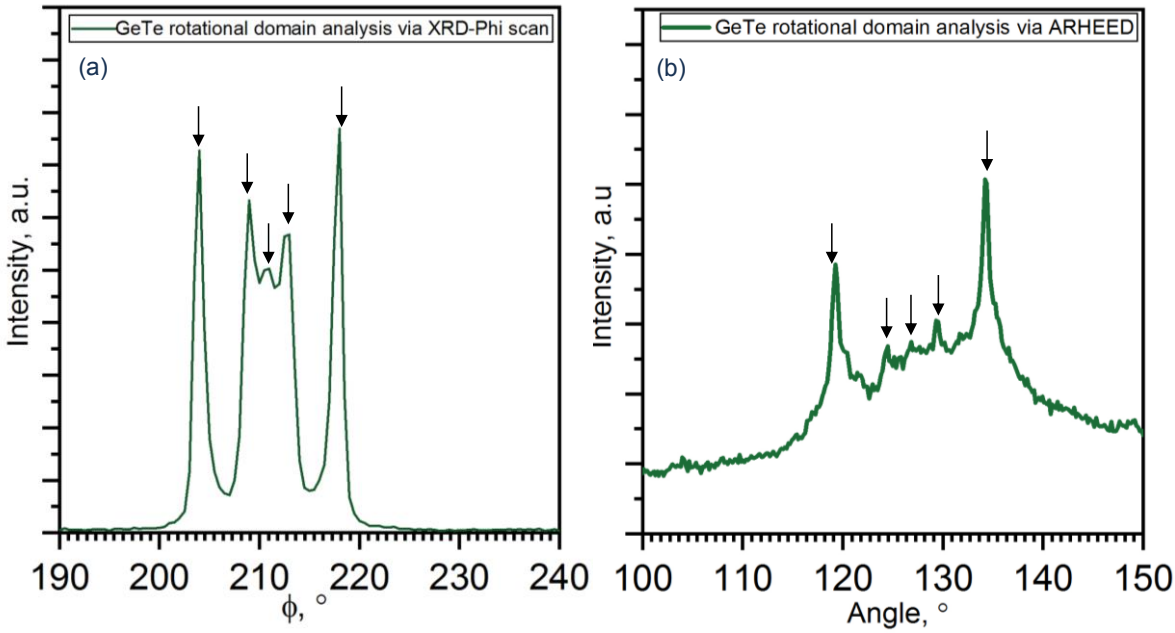

Figure 5.9: Shows the compression between (a)ϕ- scan and (b) ARHEED intensity analysis for GeTe growth on Si(111) 7x7 reconstructed surface, both show the presence of the rotational domains in the film.

ARHEED pattern indicates the presence of six fold symmetry in the GeTe film grown on the Si(111)-7x7 reconstructed surface given in Figure 5.8 (a). Each reflex spot pattern is composed of five distinct features, which are more clearly shown in the zoomed view in Figure 5.8 (b). It is interesting to examine the intensity of these features, as this highlights the sensitivity of the ARHEED scan and allows for comparison with the previously presented ϕ scan results. The ARHEED intensity plot shows these five separate peaks with a maximum angular separation of about ~7° from the central spot in Figure 5.9 (b). It is consistence with ϕ- scans results shown in Figure 5.9 (a). The presence of rotational domains affects the determination of the surface reconstruction. However, the ARHEED scan shows a 3 × reconstruction along $[11\bar{2}]$ direction and a 1 × reconstruction along the $[\bar{1}10]$ direction. Importantly, it is observed that the surface reconstruction remains unchanged across different film thicknesses.

The growth of GeTe thin films on a Si(111)-(√3 × √3)R30°-Sb surface reveals notable changes in surface reconstruction with increasing film thickness (Figure 5.5 (c)). Wang et al. reported the coexistence of GeTe(0001)-(√3 ×√3)R30° and GeTe(0001)-(1 × 1) reconstructions during the early stages of GeTe film growth on Si(111)-(√3 × √3)R30°-Sb.[32] Interestingly, such a change in film surface reconstructions is observed during the GeTe growth on Si (111) 1x1 surfaces. During the optimization of GeTe growth on the Si(111)-1×1 surface, it was observed that the film reconstructions exhibit a clear dependence on both film thickness and substrate temperature. The changes in the film's reconstruction with increasing thickness were previously depicted in the line scan (see Figure 5.5) for growth performed at a surface temperature 110°C. Further, the effect of substrate temperature has been studied in detail for GeTe growth on Si(111) 1x1 surface with ARHEED and ϕ- scans given in Figure 5.10. ARHEED and ϕ-scans at the end of growth show distinct reconstructions: films grown at 100°C and 110°C exhibit a 1× reconstruction along the $[11\bar{2}]$

direction and $[\bar{1}10]$ direction, while film grown at comparably higher substrate temperature, 120°C and 130°C, demonstrates a 3 × reconstruction along $[11\bar{2}]$ direction and 1 × along the $[\bar{1}10]$.

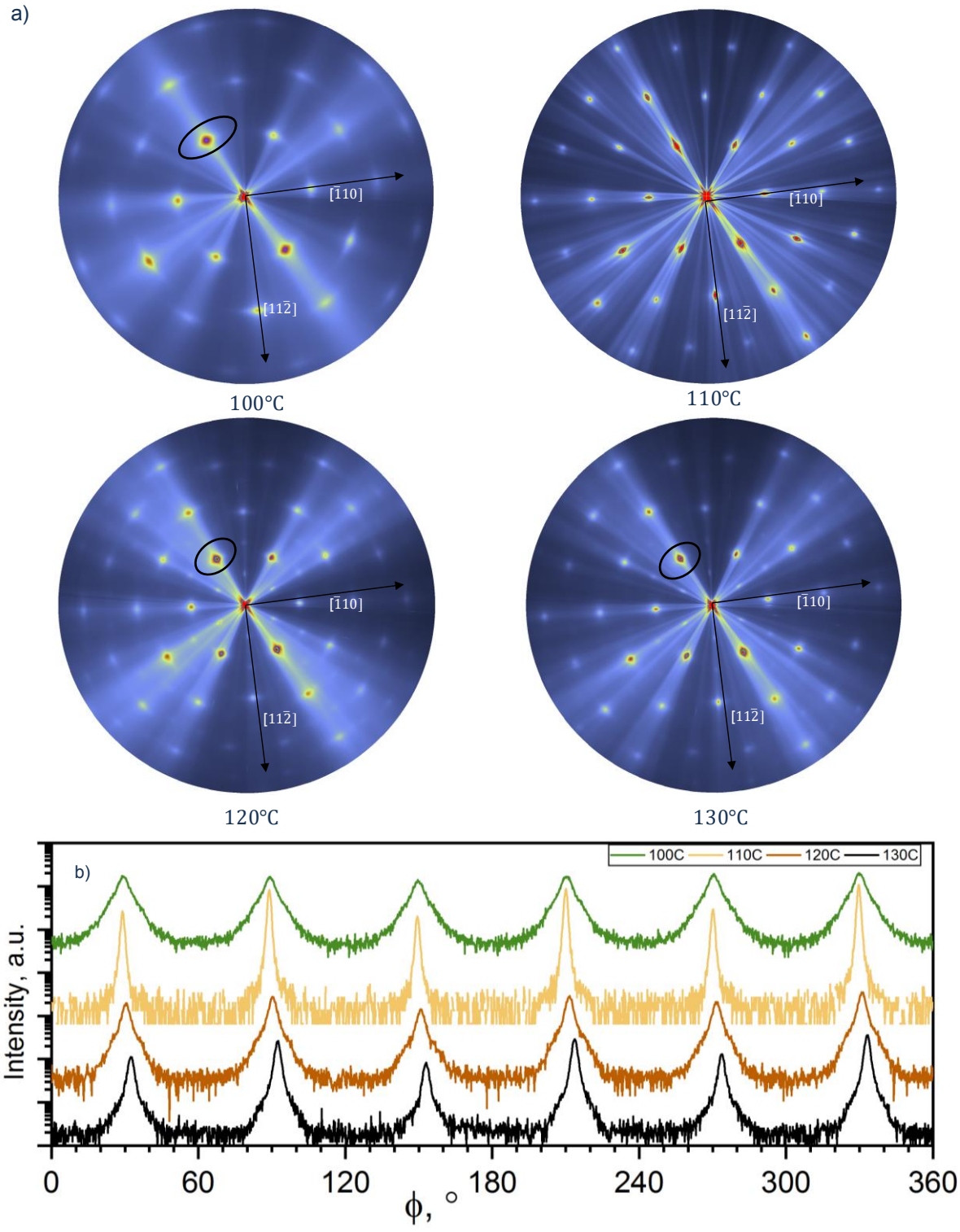

Figure 5.10: GeTe growth on Si(111) 1x1 surface: (a) ARHEED scans of film grown at various substrate temperatures reveals the surface reconstructions (b) ϕ- scans of GeTe films grown at various temperatures are taken to compare the in-plane texture.

Broader reflexes in ARHEED for films grown at 100°C, 120°C, and 130°C (see black circle) suggest the planar combination of rotational domains. The ϕ-scans for these films similarly exhibit peak broadening, indicative of multiple peaks (see Figure 5.10 (b)). In contrast, the film grown at 110°C exhibits sharp reflexes of the GeTe (0001)-(1 × 1) surface in the ARHEED patterns, while the ϕ-scan reveals relatively narrow peaks, indicating an improvement in film quality. The underlying mechanism responsible for the observed changes in surface reconstructions remains subject of further investigation.

In this section, it was demonstrated that GeTe thin films growth on Si(111)-(7x7) reconstructed, Si(111)-(√3 ×√3)R30°-Sb terminated , and Si(111)-1x1 surfaces are comparable to results presented before in the literature. The sharp streak pattern of RHEED on all three surfaces are ensuring the flat surface. The amorphous to crystalline transition (blackout) is also observed on Si(111)-1x1 and Si(111)-(7x7) reconstructed surfaces and highlighted the importance of line scans for intermediate stages of film growth which is a crucial observation not yet previously reported. The detailed comparison of domain formation on all three surfaces has been investigated with ARHEED and XRD ϕ- scans. The GeTe growth on Si(111)-(7x7) reconstructed surface exhibits the twisted domains at ±2.4° and ±7.3° along the rotational domains. To understand the correlation between the critical blackout thickness and substrate temperature, GeTe growth on the Si(111)-1x1 surface is selected for further study in Chapter 6. It is essential to note that the Si(111)-(√3 ×√3)R30°-Sb termination alters surface conductivity, making it less suitable for investigating the electrical transport properties of ultra-thin films. As a result, further investigations into the properties of GeTe ultra-thin films will be conducted on the Si(111)-(7x7) reconstructed surfaces, as detailed in Chapter 6.

5.2 SnTe:

SnTe is of great interest across various fields of study, particularly for its thermoelectric properties and its potential as a topological crystalline insulator, which has recently brought SnTe into the research spotlight. Theoretical work by Hsieh et al. in 2012 introduced the concept of SnTe as a possible topological crystalline insulator, and Tanaka et al. provided the first experimental results supporting this hypothesis.[67, 68] Research on crystalline bulk SnTe has since yielded valuable data on its band structure [69, 70], ferroelectricity [71], superconductivity [72], and Fermi surface topology [73]. More recent studies on epitaxially grown SnTe thin films have offered new insights into its electrical properties, with further support from ARPES and STM measurements.[74–76] The ferroelectric distortion in bulk SnTe, where the rhombohedral α-phase transitions to the β-phase at temperatures below 100 K, continues to be of significant interest.[72, 77] Recent DFT simulations by Plekhanov et al. [78] have explored this phase transition, while Aggarwal et al. [79] proposed the existence of local ferroelectricity at room temperature based on PFM data. This hypothesis is supported by STM measurements from Chang et al.,[77] which examined very thin (2–4 monolayers) SnTe(001) films, providing further evidence of room-temperature ferroelectric behavior. Like GeTe, SnTe is part of the main-group chalcogenides and is noted for exhibiting metavalent bonding. This makes SnTe particularly worth investigating for its ultra-thin film properties.

5.2.1 Crystal structure of SnTe :

The three phases of SnTe are illustrated in Figure 5.11. The β-SnTe phase, with a rock-salt cubic structure (lattice parameters a = 6.3268 Å, α = 90°, space group Fm-3m), is the most extensively studied phase due to its stability at room temperature and atmospheric pressure. At low temperatures (<100 K), β-SnTe undergoes a distortion along the [111] direction, transitioning into the rhombohedral α-SnTe phase (lattice parameters a = 6.325 Å, α = 89.895°, space group R3m), it has a carrier concentration of less than p=1.5·$10^{20} cm^{-3}$. Under high pressure conditions (>18 kbar), β-SnTe transforms into the orthorhombic γ-SnTe phase (lattice parameters a = 11.95 Å, b = 4.37 Å, c = 4.48 Å, space group Pnma). Since α-SnTe exists only at very low temperatures and γ-SnTe forms under extreme pressures, β-SnTe remains the most widely investigated phase.[80]

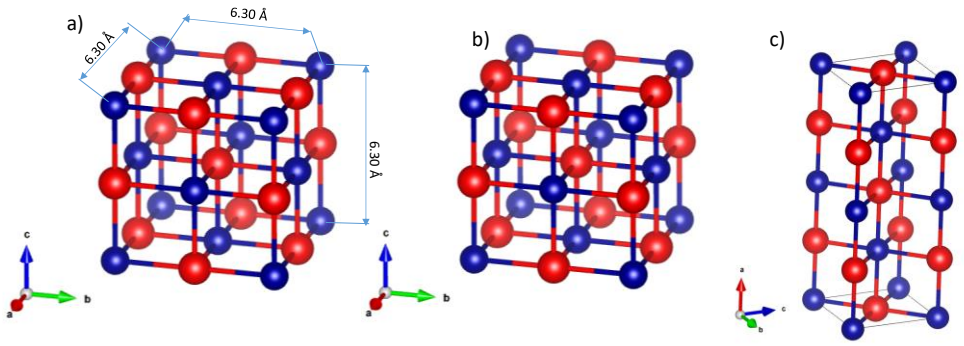

Figure 5.11: Structure of SnTe. a) gives an overview of β-SnTe unit cell, lattice parameters a = 6.3268 Å, α = 90°, b) shows the structure of α- SnTe with lattice parameters a = 6.325 Å, α = 89.895°, and c) shows the structure of γ-SnTe. Sn atoms are shown in blue and Te atoms in Red. Structure pictured by VESTA.[63]

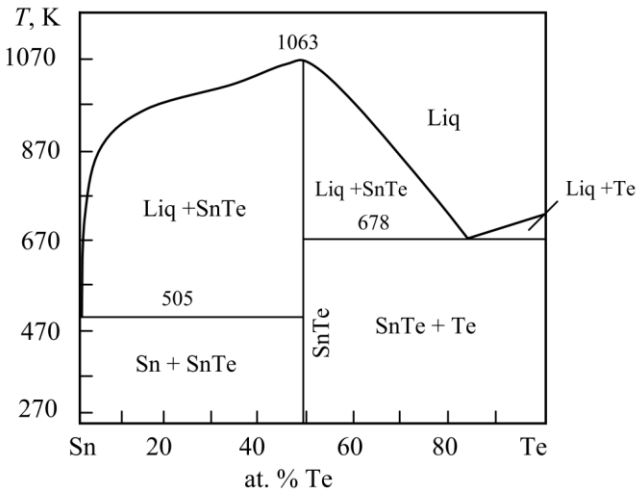

Figure 5.12: Phase diagram of SnTe showing the only possible compound stoichiometry is SnTe during growth. Taken from. [64]

5.2.2 Growth of SnTe:

The first report on the epitaxial growth of SnTe films on heated alkali-halide substrates dates back to the 1960s.[81] Since then, epitaxial SnTe films have been grown on various substrates, including CdTe(111) [82], CdTe(110) [83], KCl [84], Sapphire with a Bi_2Te_3 buffer layer [85], and galvanized SiC [86]. In 2014, Yan et al. reported the growth of SnTe via MBE on a Si(111)-7x7 reconstructed surface. [76] The growth direction was observed to be SnTe (001) on Si(111). This happenes due to the difference in their lattice symmetries. The lattice mismatch for SnTe(111) on Si(111) is 16.1%, while SnTe(001) shows an even larger mismatch of 17.9%. However, the epitaxial growth can be understood using the domain match epitaxy concept, where a 6/5 matching of major planes across the film/substrate interface minimizes residual strain. Yan et al. also reported a blackout effect in

RHEED during SnTe growth, which was attributed to strain from the large lattice misfit. Although this blackout occurred at a substrate temperature of 240°C in their work, this value varies in other studies. Notably, Kaminski [36] studied this blackout effect at significantly lower temperatures, around 100°C. A detailed investigation of the correlation between substrate temperature and critical thickness revealed that the critical thickness is inversely proportional to substrate temperature. This trend is consistent with GeTe growth, more details in Chapter 6.

In this study, SnTe is deposited using separate effusion cells for Sn and Te in their elemental forms. Highly textured crystalline SnTe films are grown under Te-rich conditions to ensure uniform thin films, a method similar to that used for GeTe deposition. The Te-rich phase is optimal for SnTe formation (Figure 5.12). A detailed investigation of Sn-rich and Sn-poor growth conditions has been conducted by team members using the same experimental setup [45, 87]. In this work, SnTe growth on the Si(111)-1x1 surface is first investigated, followed by a comparative study of its growth on the Si(111)-(√3 ×√3)R30°-Sb terminated surface and the Si(111)-7x7 reconstructed surface. Well-cleaned Si substrates were used for the growth studies, and the substrate preparation process is discussed in Chapter 2. In this work, the effusion cells of Sn and Te are heated in the range of 1030°C-1050°C and 240°C -260°C, respectively. The Sn/Te flux ratio is maintained at approximately 0.5, with growth rates ranging from 15 pm/s to 20 pm/s. The substrate temperature is varied between 150°C and 230°C, depending on the surface under study. Upon completion of SnTe thin film growth, each sample was immediately capped with an Al_2O_3 layer for ex-situ analysis, without breaking vacuum. This was accomplished using a dedicated oxide-MBE system with a base pressure of 4×10^{-10} mbar. Al_2O_3 was deposited from an electron-beam evaporator at a rate of 0.1 Å/s, with the pressure raised to 2×10^{-7} mbar during evaporation. To ensure uniform film deposition, the sample was rotated at 6 rpm.

5.2.3 Analysis of SnTe growth

The most significant stages of the epitaxial SnTe growth on Si(111) surfaces are captured by sequential in-situ RHEED images, shown in Figure 5.13. The RHEED image in Figure 5.13 (a) shows the Si(111) 1x1 surface before the growth in $[\bar{1}10]$ direction. At the initial stage of growth, substrate reflexes fade out as atoms are attaching on the surface and immediately new sharp streaks appear, which correspond to the SnTe, as shown in Figure 5.13 (b) and indicated by the white arrow mark. The sharp streaks along with a clear spot pattern confirms the flat crystalline surface. The growth mode remains the same throughout the entire growth process, confirmed by the line scan in (c). Moreover, the interface (indicated with a red dash line) is sharp, which represents the immediate coverage of the substrate's surface as the growth proceeds. Similarly, the growth of SnTe on Si(111)7x7 reconstructed surface (Figure 5.13 e) and Si(111)-(√3 ×√3)R30°-Sb (Figure 5.13 h) shows intense reflexes similar to the substrate intensity. This kind of reflex pattern indicates the high quality of crystal growth. However, the initial growth on both surfaces indicates the presence of substrate reflexes till 3 to 4 nm of film growth. Hence, the interface in the line scan shows the diffuse intensity of substrate reflexes (see Figure 5.13 f,i). This means the film is not fully covering the surface till 3 to 4 nm growth on these surfaces. Hence, the growth on these surfaces are not suitable to investigating ultra-thin films properties, especially electric transport properties.

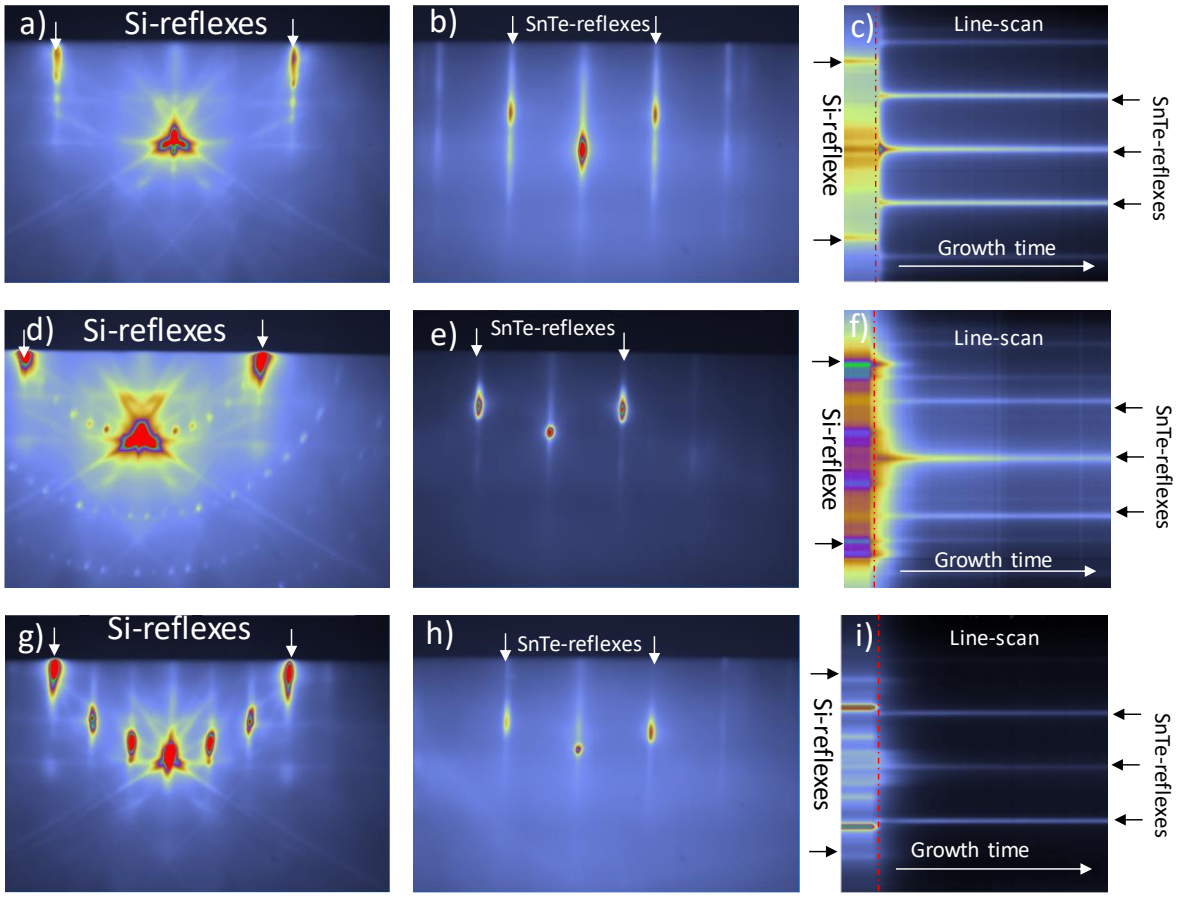

Figure 5.13: RHEED images of (a) a Si(111)-1x1 surface taken in $[\bar{1}10]$ direction, (d) a Si(111)7x7 reconstructed surface, (g) a Si(111)-(√3 ×√3)R30°-Sb terminated surface are taken in $[11\bar{2}]$ direction. SnTe growth on respective surfaces are shown in (b,e,h). Image (c, f, i) represent the line scan of SnTe growth.

Further, XRD measurements are taken for thicker films to understand the film quality on all three Si(111) surfaces. Measurements are performed in collaboration with team members from RWTH Aachen, XRD parameters are further explained in [45].

To characterize the biaxial texture of SnTe films on all three Si(111) surfaces, θ-2θ scans are performed as shown in Figure 5.14 (a). θ-2θ scans show that the SnTe films deposited on all three Si surfaces are strongly oriented in the cubic (001) direction. The (002) family peaks are accompanied by Laue oscillations, which indicates a very uniform layer thickness. Figure 5.14 (b, c) shows a zoom of the specular rod close to the Si(111) and Si(222) reflection. Laue oscillations are observed indicative for the high-crystalline quality of the film. The (002) reflexes yield a cubic lattice constant of 6.32 Å. Additionally, low intensity and broad peaks at about 1, 3 and 5 $Å^{-1}$ are observed in the SnTe film grown on the Si(111)-(√3 x √3) R30°- Sb terminated surface shown in Figure 5.14 (a). However, its origin has not been identified yet. Perhaps, these low intensity peaks might be induced due to the interaction of Sb atoms from Si(111)-(√3 x √3) R30°- Sb reconstruction with the initial SnTe growth.

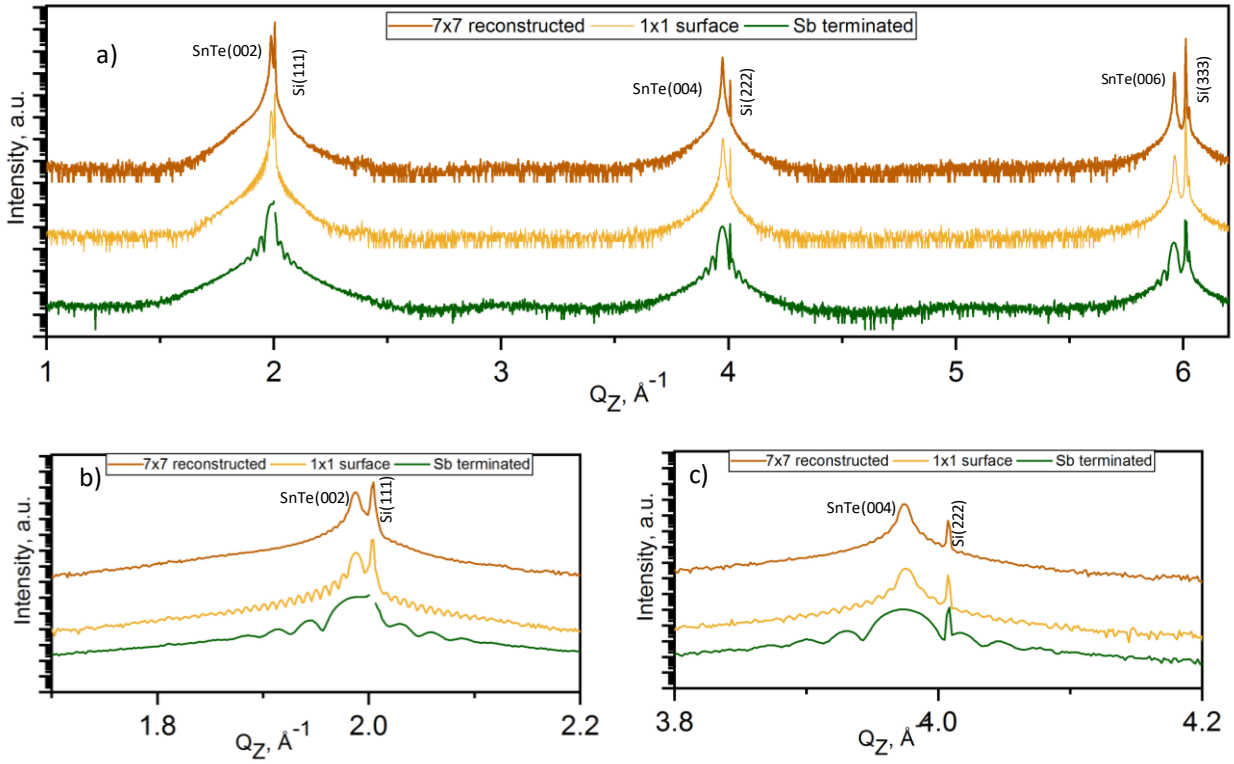

Figure 5.14: X-ray diffraction measurements of crystalline SnTe films grown over Si(111) surfaces: a) $\theta - 2\theta$ measurements of the films, which are textured in (001) direction and show Laue fringes besides the main diffraction peaks. b–c) close ups of the (002) and (004) peaks for the thicker films.

Moreover, ARHEED and ϕ scans (Phi scan) are performed on all samples to understand the presence of rotational domains. From the theoretical prospective, by considering the symmetries of substrate and epilayer, the expected minimum number of rotational domains would be three. This is due to fact that the interface of the substrate exhibits three-fold symmetry, whereas the SnTe grows with a cubic (001) texture which introduces a fourfold symmetry. Hence, the epilayer of SnTe has three equivalent possibilities to align on the Si substrate.

The ARHEED pattern of SnTe on the Si(111)-1x1 surface and on the Si(111)-(√3 x √3) R30°- Sb terminated surface shows the twelve reflexes, each being rotated by 30° (see the white circle in Figure 5.15(a,c)). These twelve reflexes correspond to the three different domains forming on both surfaces. (see Figure 5.15 b,d). Taking the intensities of the ARHEED reflexes into account, all twelve reflexes have the same intensities for SnTe growth on 1x1 surface which can be seen as evidence for the same contribution of all three domains in the film. Also, on the Si(111)- Sb terminated surface, a bright reflex is followed by two lower intense reflexes, as can distinctly be seen in black circle in Figure 5.15 (c). For further confirmation of the domain contribution in the films, phi-scan technique is used as shown in Figure 5.17.

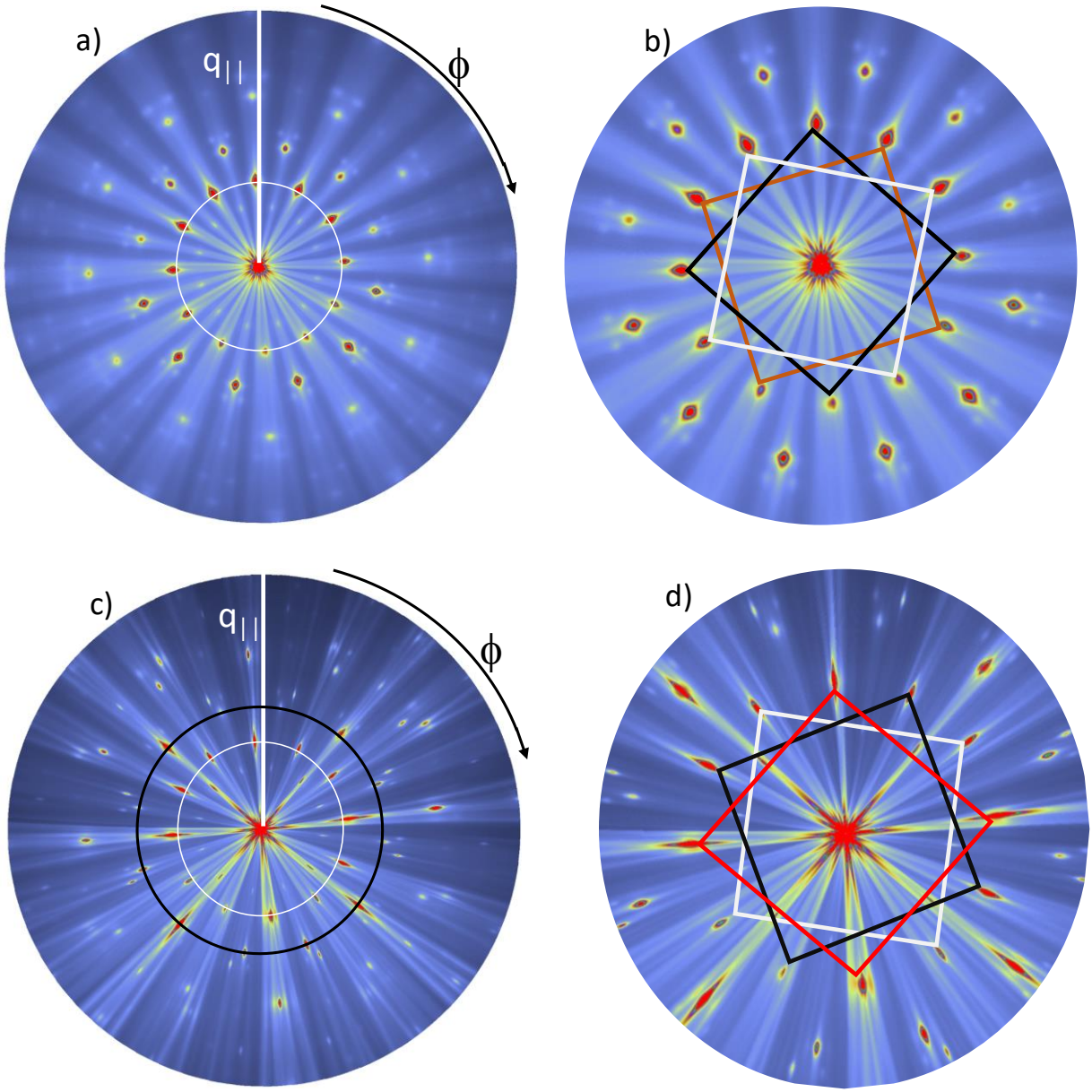

Figure 5.15: (a) and (c) are ARHEED images of SnTe growth on Si(111)-1x1 surface and Si(111)-(√3 x √3) R30°-Sb reconstructed surface respectively. Image (b), (d) represents the three possible domain formations on respective surfaces.

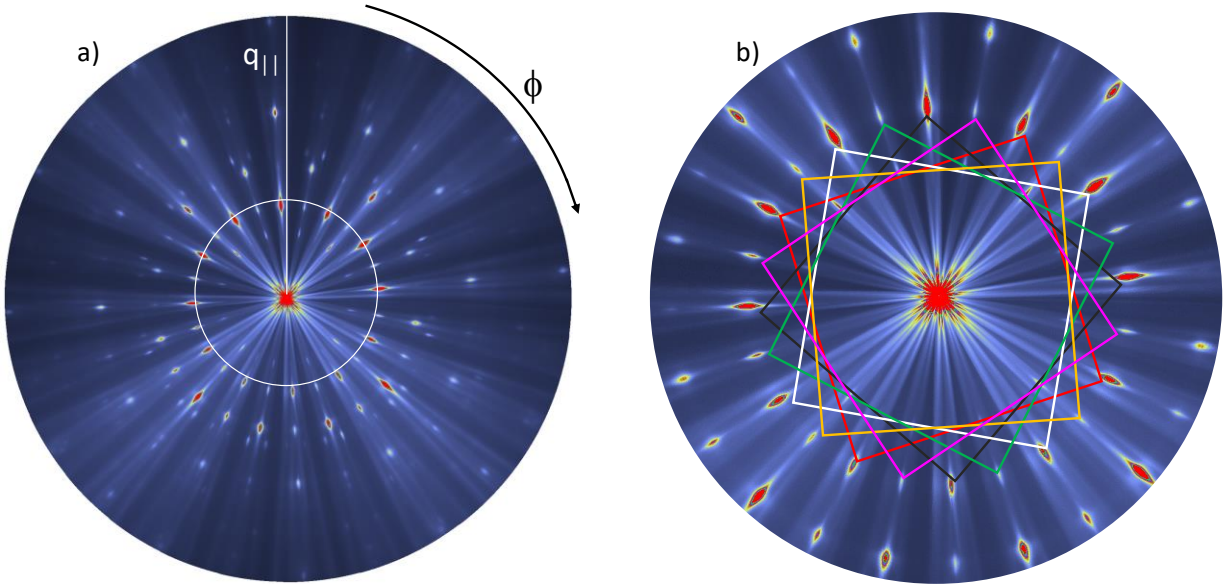

Figure 5.16: ARHEED image of SnTe growth on Si(111)-7x7 reconstructed surface(a) and (b) represents the six possible domains formation.

In contrast to the ARHEED pattern of SnTe on Si(111)-1x1 surface and on the Si(111)- Sb terminated surface, the 7x7 reconstructed surface exhibites 24 reflexes, occuring every 15°.(see the white circle in Figure 5.16 (a)). This shows that as the number of domains is doubling on the 7x7 reconstructed surface and can be represented as shown in Figure 5.16 (b). Taking the intensities of the ARHEED into account, a reflex is observed but with alternating intensities; after each bright reflex, a less intense one is observed. The 24 reflexes form two sets (Set A and B) of 12 reflexes each, where one set is more intense, presumably due to the area coverage by the corresponding domains. Nevetheless, it is important to the study ϕ scan for confirmation.

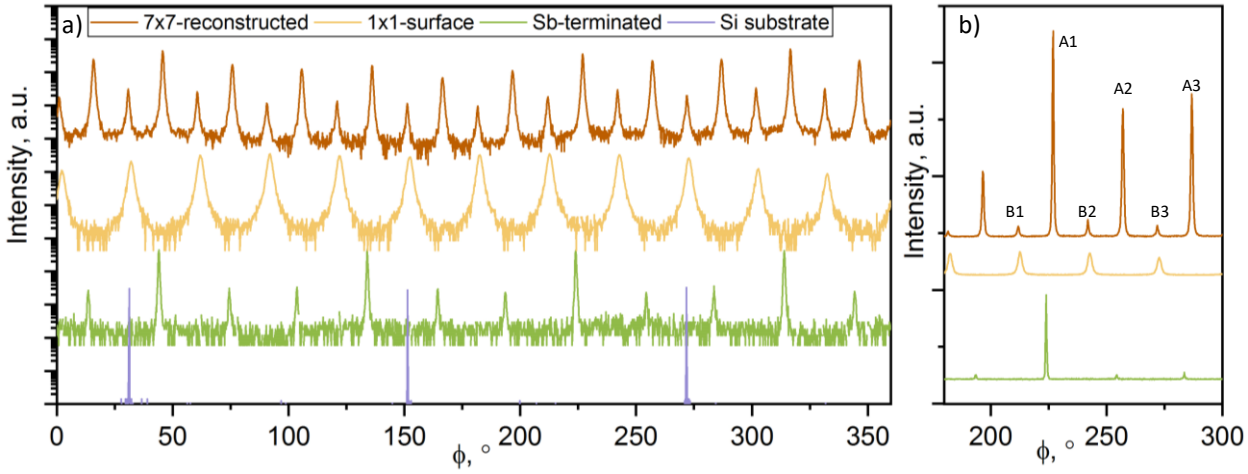

Figure 5.17: The plots show ϕ- scans of SnTe. The green, yellow and brown line show the (2 2 2) peaks of SnTe, deposited onto a Si(111)-(√3 x √3) R30°- Sb terminated, 1x1-surface 7x7-reconstructed substrates respectively. The blue line shows (1 1 1)-peaks of Si. The measurements are shown on a logarithmic scale (a) to emphasize smaller domains and to pronounce the intensity ratios between the different domains plotted in normalized linear scale (b).

To understand the presence of rotational domains in all three films, the SnTe(222) peak was investigated with a ϕ Scan as shown in Figure 5.17. The resulting pattern consists of twelve peaks, with each one rotated by 30°, for the films deposited onto Si(111)-(√3 x √3) R30°- Sb terminated surface (green line) and Si(111) 1x1-surface (yellow line). However, the number of peaks is doubled on the Si(111) 7x7-reconstructed surface (brown line), which is in agreement with the literature. As previously discussed in section 5.1.3, GeTe growth on the Si(111) 7x7-reconstructed surface also shows the additional twisted domains, apart from the twin domains, which are attributed to the misalignment of the mirror plane symmetry between substrate and film. Based on the intensity on a linear scale (as shown in Figure 5.17 (b)), these 24 peaks can be distinguished into two sets. The three rotational domains of set A show relatively higher intensity than the three domains of set B, which means the contribution of set A domains are larger in the film. Since the intensity is directly related to the volume probed, it can be seen as proportional to the occupied area of the respective domain. By judging the peaks intensity of a 1x1 –surface (yellow line) one can already conclude that the 3 domains have almost the same contribution on the film. Furthermore, the results from the Si(111)-(√3 x √3) R30°- Sb terminated surface (green line) indicates the presence of three domains. Nevertheless, the peaks are not equally intense in the linearly scaled plot. The intensity ratio between the three domains becomes clearly visible, indicating that two of them are severely suppressed. Judging from the surface symmetry, there should be no mechanism that suppresses two of the domains. Nevertheless, θ-2θ scans also indicates the additional broad peaks like features at about 1, 3 and 5 $Å^{-1}$ in this film, which indicates the further investigation is required to understand the role of Sb- passivation.

In this section, the growth of SnTe(001) thin films on Si(111)-(7x7) reconstructed, Si(111)-(√3 ×√3)R30°-Sb terminated, and Si(111)-1x1 surfaces was demonstrated. RHEED patterns for all three surfaces exhibited sharp streaks, indicating smooth, flat surfaces. Detailed RHEED analysis revealed that the growth on the Si(111)-1x1 surface is most suitable for ultra-thin film studies, as it showed immediate coverage of the substrate. In contrast, thin films grown on Si(111)-(7x7) reconstructed and Si(111)-(√3 ×√3)R30°-Sb terminated surfaces exhibited substrate reflexes up to 3 to 4 nm of thickness, indicating incomplete film coalescence. A comparative analysis of domain formation on all three surfaces was performed using ARHEED and XRD φ-scans. The SnTe growth on the Si(111)-(7x7) reconstructed surface displayed twice the domain count compared to the Si(111)-1x1 and Si(111)-(√3 ×√3)R30°-Sb terminated surfaces. Due to the alteration of surface conductivity by the Si(111)-(√3 ×√3)R30°-Sb termination, it is unsuitable for studying the electrical transport properties of ultra-thin films. Consequently, further investigations of SnTe ultra-thin films are conducted on Si(111)-1x1 surfaces, as discussed in Chapter 6.

5.3 SnSe

IV-VI semiconductor materials are a key area of research for next-generation technologies, including thermoelectric, optoelectronic, memory-switching, and photovoltaic devices. Within this material family, tin selenide (SnSe) stands out due to its versatile properties and broad range of applications, such as in solar cells, photocatalysis [88], photodetectors [89], phase-change memory [90], gas sensors [91], batteries [92], supercapacitors [93], topological insulators [94], and thermoelectric devices [95]. The synthesis and deposition techniques play a crucial role in determining the phase and structure of SnSe. Solution-phase methods like solvothermal [96], hot injection [97], and one-pot [98] techniques have been employed to synthesize SnSe in various forms, from bulk crystals to colloidal nanosheets and nanowires. In contrast, SnSe thin films have been fabricated using techniques such as flash evaporation, thermal evaporation, and spray pyrolysis, predominantly on glass substrates to investigate their crystal orientation and electrical properties. However, there is limited research on the fabrication of epitaxial SnSe films. Teghil et al. reported SnSe epitaxial growth on (001)-oriented MgO and $SrTiO_3$ substrates using pulsed laser deposition, although a detailed characterization was lacking. The epitaxial growth of SnSe on silicon surfaces via MBE remains underexplored in the literature.

SnSe exists in two primary crystal structures: a layered orthorhombic phase and a rocksalt structure. The orthorhombic phase undergoes a temperature-induced phase transition from Pnma to Cmcm, as shown in Figure 5.19. The low-temperature orthorhombic Pnma phase, which has distinct lattice constants ($a \neq c \neq b$) and typical Peierls distortions, transforms into the high-temperature Cmcm phase, characterized by higher symmetry ($a \neq b = c$) and strong anharmonicity, which significantly reduces thermal conductivity. Recently, SnSe has demonstrated an outstanding thermoelectric figure of merit (ZT) of approximately 2.6 at 923 K along the b-axis, with the crystal in the high-temperature Cmcm phase, setting a new benchmark for thermoelectric efficiency.[99] Yadong et al. studied ultrafast carrier and phonon dynamics in SnSe, revealing that optical excitations can transiently switch the crystal symmetry from Pnma to Cmcm at room temperature within a few hundred femtoseconds, with a low excitation threshold. [100] Their findings indicate that the transition to the nonequilibrium Cmcm phase is driven by the displacive generation of coherent Ag phonons, which softens the lattice. This process involves an anti-Peierls distortion, where electronic excitation modifies the potential energy surface from a double-well to a single-well configuration.

So far, the Cmcm phase has primarily been achieved through thermal equilibrium methods, such as heating or applying external pressure. A key challenge remains in finding a method to stabilize this high-temperature Cmcm phase at ambient conditions. Furthermore, on the electronic bonding mechanism map, Pnma phase being covalent in nature. This suggests that the two phases possess distinct properties, making SnSe an attractive candidate for further exploration, particularly in the context of ultra-thin film properties and confinement effects.

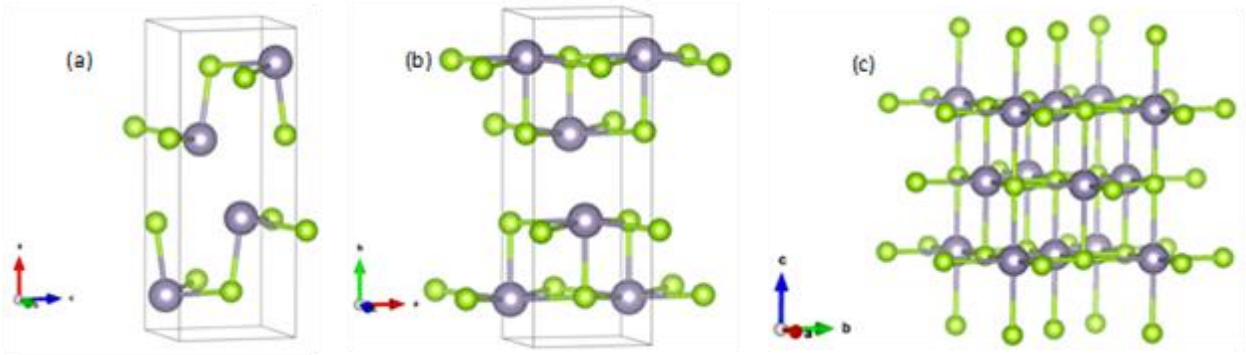

Figure 5.18: Representative structures of SnSe phases (a) Pnma, (b) Cmcm, (c) rocksalt. The images are produced using the VESTA software.

SnSe bulk structure demonstrates a layered orthorhombic structure having space group Pnma with lattice constant: a = 11.49 Å, b = 4.440 Å, c = 4.15 Å at room temperature shown in Figure 5.18 (a).[99, 101] It undergoes a second-order displacive type phase transition at temperatures above 750 K, from lower symmetric SnSe (space group Pnma) to higher symmetric SnSe (space group Cmcm) phase. The lattice constant of Cmcm phase is a = 11.713 Å, b = c = 4.31 Å shown in Figure 5.18 (b).[99] The rocksalt phase of SnSe is having lattice parameters a=b=c= 6.02 Å and the unit cell belongs to the Fm-3m space group.[102] From the Sn–Se binary phase diagram, there are two possible stable phases for pure SnSe: low-temperature orthorhombic α SnSe (<800K) and high temperature orthorhombic β-SnSe (>800 K).

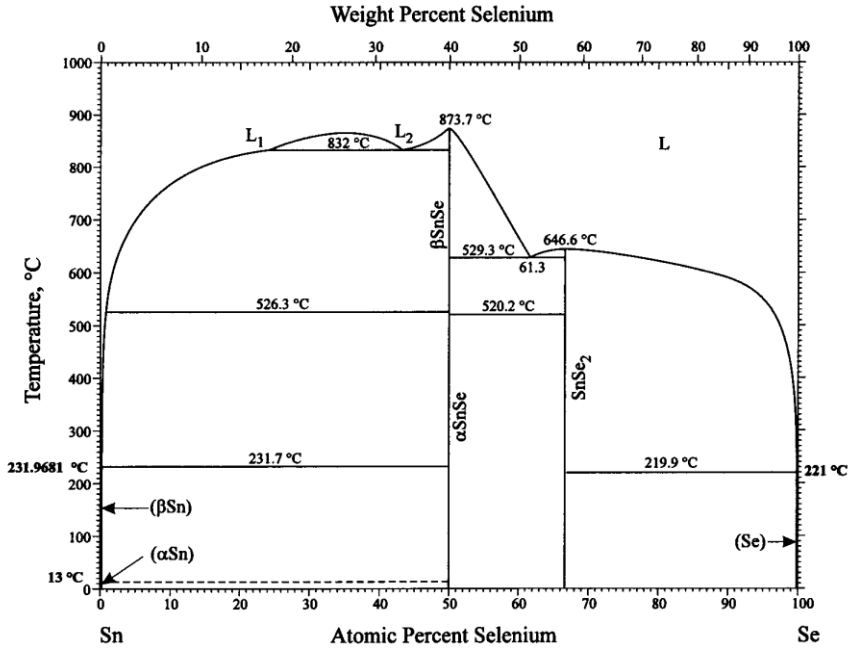

Figure 5.19: Binary phase diagram of Sn-Se depicting the two predominant compounds, SnSe and $SnSe_2$. The focus of this study lies on SnSe, particularly relevant for molecular beam epitaxy (MBE) applications. Taken from[103].

5.3.1 Epitaxial growth of SnSe

Tin selenide-based compounds have so far received limited attention regarding deposition via molecular beam epitaxy compared to other 2D chalcogenides. In a seminal study by Brian et al. in 2016, the growth of $SnSe_2$ via MBE on GaAs substrates was reported. [104] The researchers established the baseline growth parameters by precisely controlling the Sn/Se flux ratio, investigating various Se ratios, such as 10:1 and 40:1, to achieve pure $SnSe_2$ deposition. Their findings also revealed that selenium-deficient conditions could result in mixed-phase growth, where both SnSe and $SnSe_2$ coexist. Given the coexistence of both $SnSe_2$ and SnSe phases in the phase diagram (see Figure 5.19), precise control of Se flux is crucial for obtaining the desired phase. A similar study conducted by Nguyen et al. investigated the impact of the Se/Sn flux ratio on the epitaxial growth of SnSe thin films on MgO(100) substrates.[101]

Furthermore, the choice of the selenium evaporation source can significantly influence the deposited phase. It is well-known that selenium typically evaporates as Se_8^+ molecules using conventional effusion cells. Therefore, the use of a cracker cell becomes necessary to fragment selenium molecules (e.g., Se_8^+, Se_7^+, and Se_6^+) into smaller fragments, such as Se_2^+ and Se^+ which enhance the reactivity of Se and hence, influences the growth mechanism.[24] This study presents the first successful growth of highly textured SnSe films on three different Si(111) surfaces: Si(111) 1x1, Si(111) 7x7 reconstructed, and Si(111)-(√3 × √3)R30°-Sb terminated surfaces. The lattice constants for the Pnma phase are b = 4.440 Å and c = 4.135 Å and corresponding lattice mismatches are 15.62% along the b-axis and 7.68 % along the c-axis. The experiments were performed using a selenium cracker cell and a high-temperature tin effusion cell. A series of experiments have been performed to establish the optimal growth condition to achieve highly textured SnSe thin films on Si(111) surfaces. One of the important parameters is to reach this goal the Sn/Se flux ratio. Our observations combining XRD and RHEED data suggest that Sn/Se flux ratio near to 0.3 and a growth rate of around 0.16 Å/s are the optimal conditions.

Well-cleaned Si(111) substrates were used for the growth studies. The necessary substrate preparation process has been discussed in Chapter 2. The growth temperature ranges for Si(111) 1x1 surface from 190°C to 205°C, the optimal substrate temperature is 197°C. While for growth on the Si(111) 7x7 reconstructed and Si(111)-(√3 x √3) R30°- Sb terminated surfaces, the temperature ranges from 195°C to 210°C. The optimal growth temperature on the Si (111) 7x7 reconstructed surface is 200°C and on Si(111)-(√3 x √3) R30°- Sb terminated surfaces is 206°C. Moreover, experimental observations suggest that single-side polished silicon samples exhibited growth temperature profiles roughly 20°C lower than their double-side polished, possibly due to reflective heating effects. The detailed substrate temperature profile for the SnSe deposition on Si (111) 1x1 surface is provided in Figure 5.20. This temperature was chosen based on real-time RHEED observations, desired film thickness, and crystalline quality confirmed via X-ray diffraction analysis. At the end of the growth of the SnSe thin film, for further ex-situ investigations, the SnSe films are immediately capped with Al_2O_3 without breaking the vacuum in a dedicated oxide-MBE system. This was done using a dedicated oxide-MBE system with a base pressure of 4×10^{-10} mbar. Al_2O_3 was deposited via electron-beam evaporation at a rate of 0.1 Å/s, with the pressure rising to 2×10^{-7}

mbar during deposition. To ensure uniform film thickness, the sample was rotated at 6 rpm during deposition.

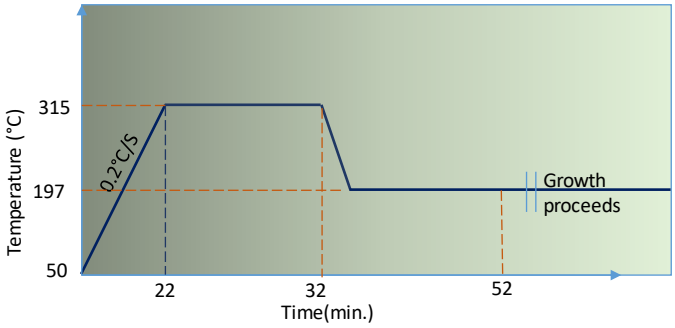

Figure 5.20: Substrate (Manipulator) temperature profile for SnSe growth on Si(111)1x1 surface.

5.3.2 Analysis of SnSe growth

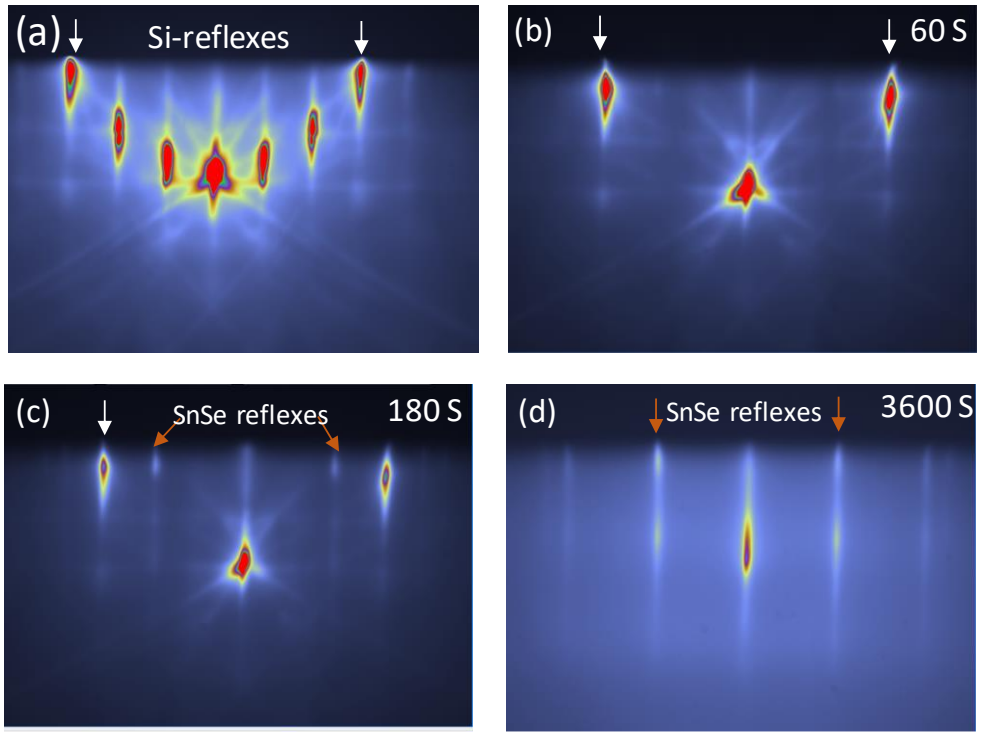

Figure 5.21: RHEED images (a) Si(111)-(√3 ×√3)R30°-Sb terminated surface taken in $[\bar{2}11]$ direction. (b) taken after 60 seconds of initial deposition; reflexes are similar to the 1x1 surface of Si(111). (c) As growth proceeds, SnSe reflexes arise around 180 seconds of deposition. (d) The image taken at the end of the growth shows SnSe reflexes.

The epitaxial growth of SnSe on a Si(111)-(√3×√3)R30°-Sb terminated surface is characterized using sequential in-situ RHEED images, capturing significant growth stages in the$[\bar{2}11]$ direction (as shown in Figure 5.21). Prior to the growth, the RHEED image reveals the characteristic reflex pattern of the Si(111)-(√3×√3)R30°-Sb surface. Upon the opening of the Sn and Se effusion cells, a noticeable shift in the surface reflex pattern occurs, with the internal reflexes of the Sb-terminated surface fading during the first 60 seconds of deposition. The remaining outer reflexes resemble the Si(111) 1x1 surface (Figure 5.21 (b)), with no new reflexes observed. This persistence of the 1x1-like pattern complicates the understanding of its origin. A possible hypothesis is that Se atoms further saturate the Sb-terminated surface, forming a distorted 1x1 phase. However, to confirm this hypothesis; further investigation such as X-ray photoelectron spectroscopy, is needed to confirm the atomic composition and bonding on the surface. As deposition continues, new reflexes appear after approximately 180 seconds (Figure 5.21 (c)), indicating the onset of crystallization, while the 1x1-like reflexes diminish (marked by a white arrow). The sharp streak pattern corresponding to SnSe remains consistent throughout the growth, signifying the formation of a flat crystalline surface (Figure 5.21(d)).

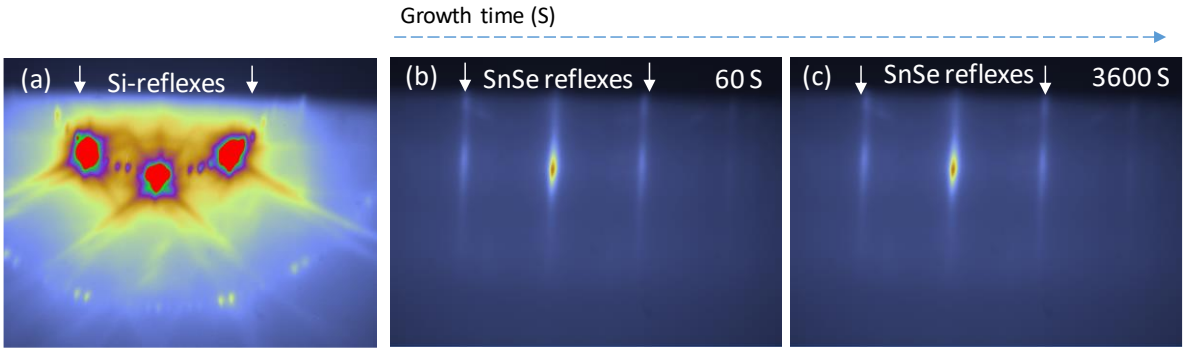

Figure 5.22: RHEED images (a) Si(111)7x7 reconstructed surface taken in $[\bar{1}10]$ *direction before growth. (b) taken after 60 seconds of initial deposition (c) final image taken at the end of, reflexes pattern indicates the deposition of smooth crystalline film is achieved.*

Similarly, the growth of SnSe is investigated on the Si(111) 7x7 reconstructed surface. Figure 5.22 (a) presents a RHEED image captured on the Si(111) 7x7 reconstructed surface in the $[\bar{1}10]$ direction prior to the growth. Upon the commencement of growth, the substrate reflexes immediately diminish as atoms starts attaching to the surface, and at the same time new reflexes start to appear on the RHEED screen, indicative of SnSe formation, as illustrated in Figure 5.22(b). These sharp streaks signify a flat crystalline surface. These streak patterns remain unchanged till the end of the deposition as shown in Figure 5.22 (c). Similarly, SnSe growth on the Si(111) 1x1 surface also showed the immediate appearance of sharp streaks in the RHEED pattern as soon as deposition starts, suggesting a crystalline film with a smooth surface shown in Figure 5.23. Prior to growth, RHEED images of the Si(111) 1x1 surface were captured along two high-symmetry directions, $[\bar{2}11]$ and $[\bar{1}10]$, shown in Figure 5.23 (a) and (c), respectively. and The RHEED images in Figure 5.23 (b) and (d) show the sharp streak reflex pattern from the deposited SnSe in the corresponding directions, confirming the film's crystalline nature.

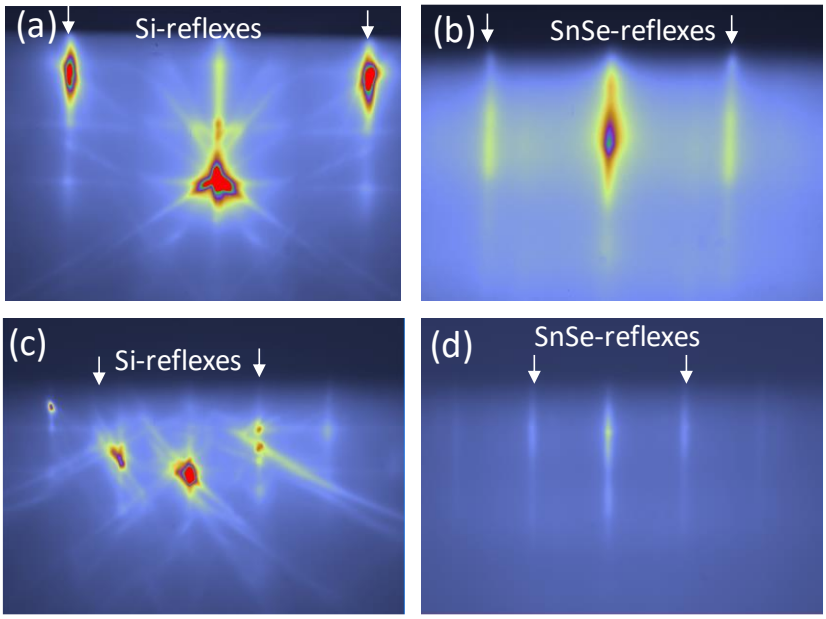

Figure 5.23: RHEED images (a) Si(111) 1x1 surface taken in $[\bar{1}10]$ *direction and (c) taken in* $[\bar{2}11]$ *direction before growth. (b) and (d) RHEED Images are taken at the end of the growth in respective directions.*

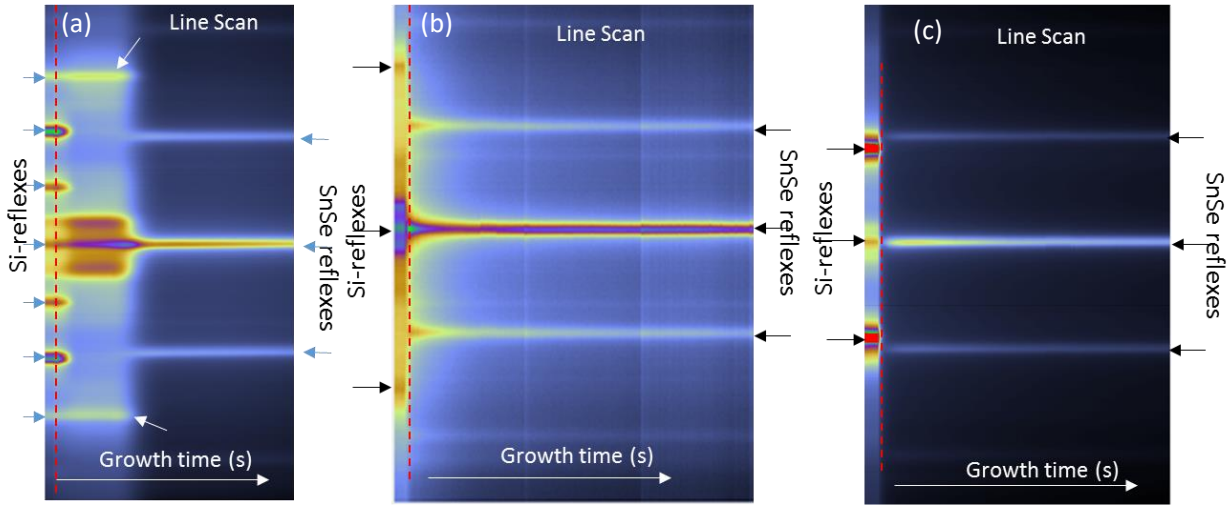

Figure 5.24: RHEED line scans of SnSe growth on (a) Si(111)-(√3 ×√3)R30°-Sb terminated surface is taken in $[11\bar{2}]$ *direction, (b) Si(111) 1x1 surface taken in* $[\bar{1}10]$ *direction (c) Si(111)7x7 reconstructed surface is taken in* $[11\bar{2}]$ *direction.*

To better understand the interface between the substrate and the SnSe film, RHEED line scans were performed on SnSe grown on three different Si(111) surfaces: (√3×√3)R30°-Sb-terminated, 1x1, and 7x7 reconstructed. The interface of substrate and SnSe film is represented with the dashed red line in Figure 5.24. The interface SnSe film on Si(111)-1x1 surface and Si(111)7x7 reconstructed surface shows emergence of immediate reflexes corresponding to SnSe, remaining unchanged throughout the growth shown in Figure 5.24 (b, c). Also, the interface is sharp, which represents the immediate coverage of the substrate's surface as the growth proceeds. The interface between SnSe film and Si(111)-(√3×√3)R30°-Sb terminated surface is complex. At the beginning of growth on the Si(111)-(√3×√3)R30°-Sb terminated surface, changes to Si(111) 1x1 surface-like reflexe patterns indicated

with white marks in Figure 5.24 (a), imply that the substrate rearranges. These patterns remain unchanged till 180s of deposition. Later, the reflexes corresponding to SnSe appear and remain unchanged until the end of the growth.

To further investigate the texture and quality of the SnSe films, comprehensive XRD measurements were performed on thicker films deposited on Si(111) 1x1, Si(111) 7x7 reconstructed, and Si(111)-(√3×√3)R30°-Sb terminated surfaces. This analysis aimed to compare the structural properties of SnSe grown on three distinct Si(111) surfaces. The study was conducted in collaboration with Dr. Jalil Abdur Rehman, whose expertise in materials characterization significantly contributed to the work.

The characterization techniques employed included θ-2θ scans, X-ray reflectivity (XRR), phi scans, pole scans, and reciprocal space mapping (RSM). These methods provided detailed insights into the crystallographic orientation and structural alignment of the SnSe films. Further analysis of these results is presented in Chapter 6.

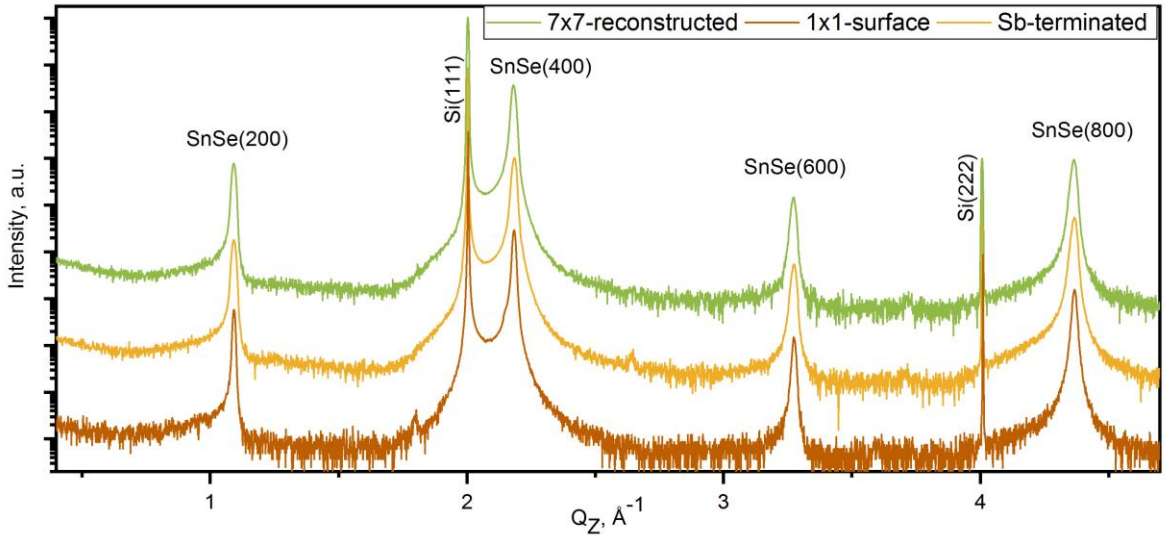

Figure 5.25: The plots show $\theta - 2\theta$ scan of SnSe grown on Si (111) -(√3 ×√3) R30°-Sb terminated surface (yellow line), Si (111) 1x1 surface (brown line), and Si (111) 7x7 reconstructed surface (green line). On all three surfaces, films are grown in (200) direction, a - axis-oriented.

To determine the out-of-plane orientation and structure of the SnSe epitaxial films, θ-2θ scans were performed on approximately 30 nm thick samples (measured by XRR) grown on Si(111) 1x1, Si(111) 7x7 reconstructed, and Si(111)-(√3×√3)R30°-Sb terminated surfaces. Figure 5.25 shows the θ-2θ scans, revealing a strong alignment of the SnSe films along the (h00) direction on all three Si(111) surfaces. The observed peaks positions are aligned with the SnSe Pnma phase, as indicated by the ICSD: 50561 data files. Sharp reflections at Qz = 2.000 $Å^{-1}$and 4.002 $Å^{-1}$ correspond to the Si (111) and (222) substrate reflections, respectively, while the remaining four peaks represent the SnSe (200) family peaks. No additional peaks are observed, indicating a unique out-of-plane crystal orientation on all three surfaces. The calculated out-of-plane lattice constant from the (200) peak, along the 'a' axis, is 11.509 ± 0.002 Å, consistent with reported bulk values for the Pnma phase. [89]

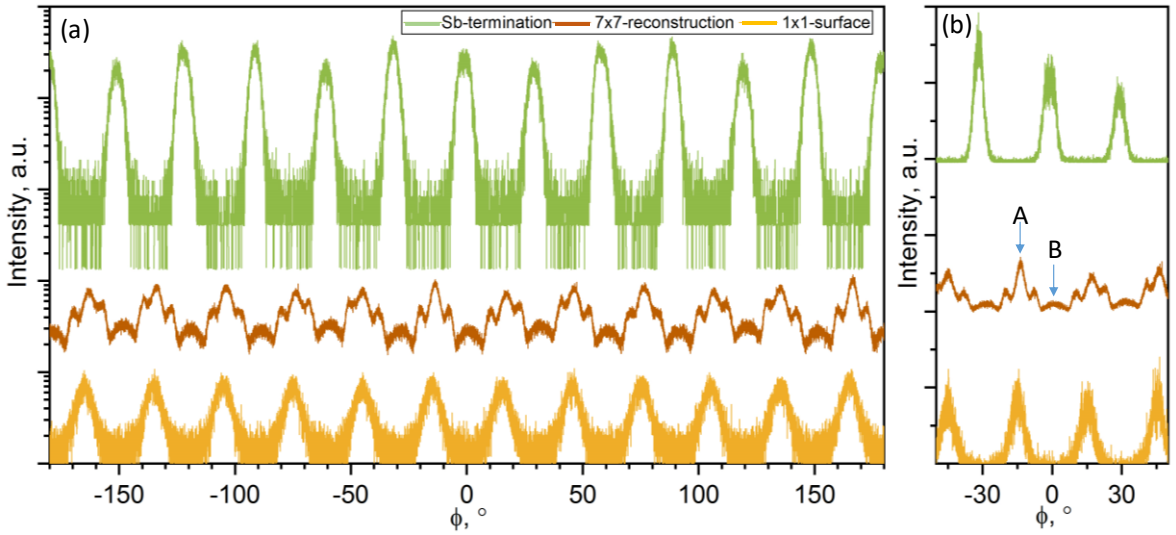

Figure 5.26: Schematic illustration of ϕ-scans measurement along (111) plane of orthorhombic SnSe films grown on Si(111)-(√3x√3) R30°- Sb terminated surface (green line), Si(111) 1x1-surface (yellow line) and Si(111) 7x7-reconstructed surface (brown line). (b) The measurements are shown on a normalized linear scale to pronounce the intensity ratios between the different domains.

The SnSe (111) peak has been analyzed using a ϕ-scan to study the in-plane domains present in all three films. Based on the surface symmetries of both the substrate and the epilayer, a minimum of three rotational domains is expected, analogous to the SnTe (001) growth on Si(111) surfaces, as discussed in previous Section 5.2.3. This can be attributed to the trigonal symmetry of the Si(111) substrate and the orthorhombic Pnma (100) texture of the SnSe films, which exhibits near-fourfold symmetry. Consequently, the SnSe epilayer can align in three equivalent orientations on the Si substrate. Due to the small variation in the in-plane lattice parameters of the Pnma phase b = 4.440 Å, c = 4.15 Å, the system is effectively treated as a pseudo-fourfold system in this study.

In the Figure 5.26 (a), the ϕ-scans reveal a pattern consisting of twelve peaks, each separated by 30°, for both the SnSe film deposited on the Si(111)-(√3 × √3) R30°-Sb terminated surface (green line) and the Si(111) 1x1 surface (yellow line). These twelve peaks correspond to three distinct rotational domains. A quantitative analysis of the intensity ratios on the normalized linear scale, as shown in Figure 5.26 (b). It is observed that the SnSe film grown over the Si(111) 1x1 surface exhibit an equal contribution from all three rotational domains, the intensity ratio is 1:1:1. Since, the intensity is directly related to the volume probed, it can be seen as being proportional to the occupied area of the respective domain in the film. In contrast, the SnSe growth on Si(111)-(√3 x √3) R30°-Sb terminated surface shows a different contribution of these rotational domains in the film.

The rotational domains in the SnSe film grown on the Si(111) 7x7 reconstructed surface exhibit a more complex structure. As shown in Figure 5.26 (follow brown line) (a) multiple distinguishable (48) peaks are present. To better understand this complexity, the peaks can be categorized based on their intensity into two sets, labeled A and B, as illustrated in Figure 5.26 (b). Each set consists of 12 peaks, separated by 30°, indicating three rotational domains within each set. Considering the peak intensity, 12 peaks of set A belong to major three rotational domains contributing to the film. Further, with each rotational domain of set A, additional twisted domains at~ ± 6° to the central

peak are present. In total 12 domains are contributing to the film. Mechanism behind the origin of such a large number of domains is not understood and requires further investigations. However, one of the potential origin of these additional domains could be misalignment of substrate and film mirror symmetry.[32] Interestingly, the similar twisted domains are also observed in the case of GeTe and SnTe films grown over Si (111) 7x7 reconstructed surface (section 5.2.3 and section 5.1.3). Based on observations from RHEED and ϕ-scans, further studies have been conducted to explore the growth of SnSe films on Si(111) 1x1 surfaces.

The in-plane orientation of the SnSe film grown on the Si(111) 1x1 surface was further investigated using ARHEED and XRD pole figure measurements. XRD pole figure of (420) plane (2θ = 58.5°) SnSe film grown over Si(111) 1x1 surface reveals twelve symmetrical poles, each separated by 30° (ϕ) at χ = 56.8° (blue circles), in Figure 5.27. These twelve poles suggest the presence of 3 rotational domains. This observation agrees with results obtained from ϕ-scans. Additionally, six poles belong to the Si substrate (13-1) plane (2θ = 56.12°) at χ = 58.5°are visible in the pole figure. The presence of the three rotational domains is further analyzed by ARHEED measurements, as shown in Figure 5.28 (a). The ARHEED data reveal 12 reflexes, each separated by 30°, indicating that each rotational domain is rotated by 30° in-plane. This observation is consistent with the results from the pole figure analysis. The alignment of these rotational domains is depicted schematically in Figure 5.28 (b). An additional pole figure is provided in the Appendix Figure 0.1 , illustrating the investigation of the SnSe (111) peak (2θ = 30.44°) at χ = 75.21°. Due to instrumental limitations, the SnSe reflections are only partially visible.

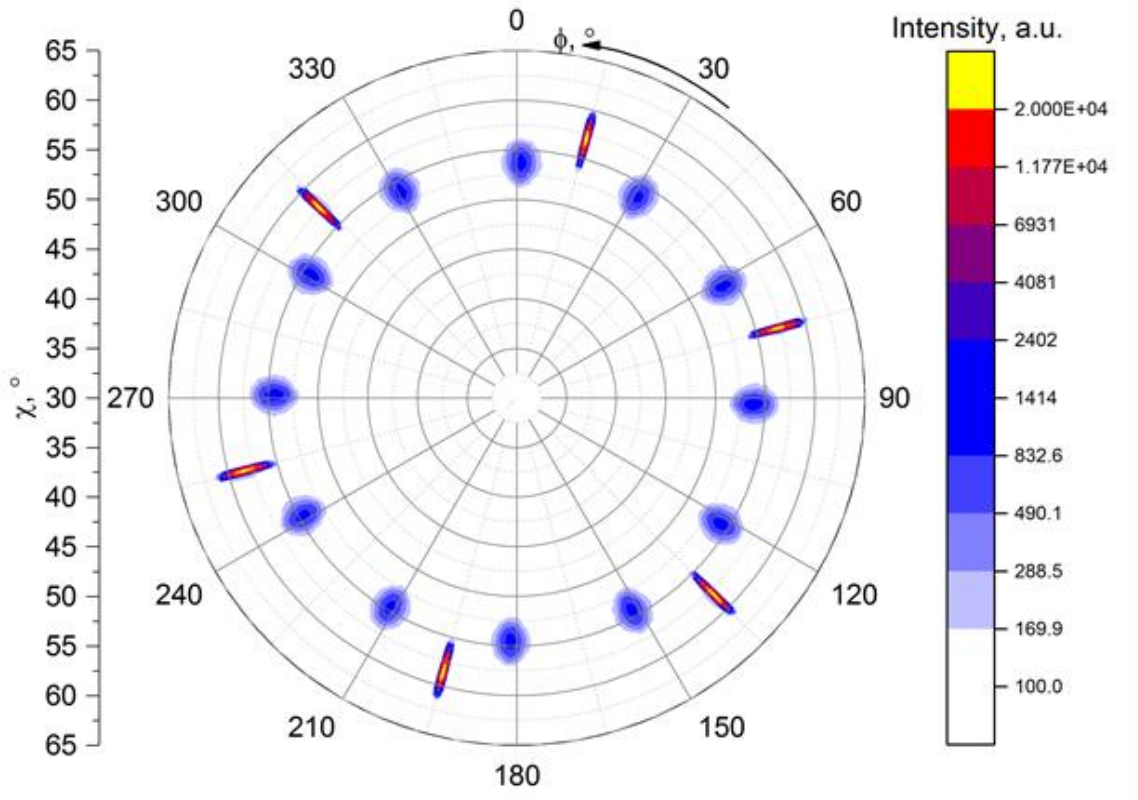

Figure 5.27: Pole figure of (420) plane (2ϑ = 58.5°) SnSe film grown over Si(111) 1x1 surface showing twelve poles (blue circles) corresponding to 3 domains. Additionally, six poles belong to Si substrate (13-1) plane (2ϑ = 56.12°).

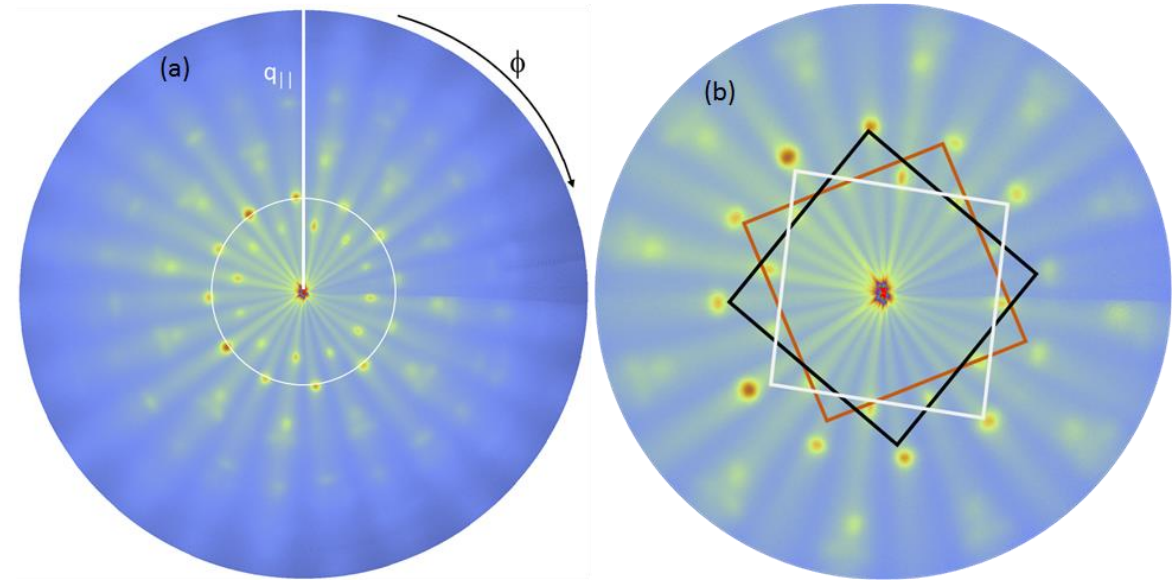

Figure 5.28: ARHEED scans of (a) SnSe film deposited over Si(111) 1x1 surface and (b) zoom image of the inner circle reflexes represents the three possible rotational domains.

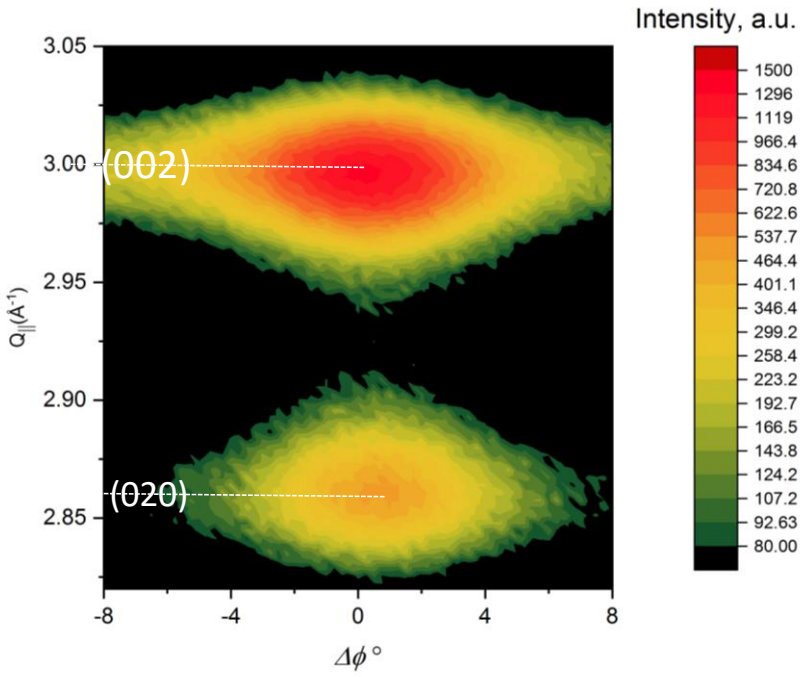

Figure 5.29: Reciprocal space mapping shows the reflexes of (002) and (020) to determine the in-plane lattice constant.

To determine the in-plane lattice parameters, RSM is performed on 30nm SnSe film grown on the Si(111) 1x1 surface. The measurements are conducted for (020) and (002) peaks shown in Figure 5.29. The calculated in-plane lattice parameters from the RSM are b=4.395 ± 0.02 Å and c = 4.194 ± 0.02 Å, which exhibit minor deviations from the previously reported values of b= 4.44 Å and c= 4.15 Å.[99] Additionally, from the in-plane and out of plane lattice parameters of the film, the calculated SnSe unit cell volume is 212.14 $Å^3$, which is in good agreement to the theoretical calculated value 212.29 $Å^3$.

In conclusion, the epitaxial growth of SnSe on Si(111) surfaces, including Si(111)-(√3×√3)R30°-Sb terminated, Si(111) 1x1, and Si(111) 7x7 reconstructed surfaces, was systematically studied using in-situ RHEED, XRD, ARHEED, XRR techniques. The RHEED images captured during growth reveal key insights into the crystallization process and surface structure. SnSe growth on the Sb-terminated surface is notably complex, with initial 1x1-like patterns transitioning to crystalline SnSe after a delay, while on both the Si(111) 1x1 and 7x7 surfaces, SnSe reflexes appear immediately, indicating rapid surface coverage and crystalline formation. XRD analysis demonstrates that SnSe films exhibit strong (100) out-of-plane orientation across all three Si(111) surfaces, with lattice constants and unit cell volumes consistent with bulk SnSe. In-plane domain structures were further explored through ϕ-scans and ARHEED measurements, revealing three rotational domains for SnSe films on the Si(111) 1x1 and Sb-terminated surfaces, while the 7x7 surface showed more complex domain behavior, with additional twisted domains. Notably, based on the XRD and RHEED data, the SnSe(100) film grown on the Si(111) 1x1 surface exhibits the highest quality of crystalline film structure among all the

studied surfaces. As a result, further investigations of the confinement effect are conducted on films grown on the Si (111) 1x1 surface, as detailed in Chapter 6.

6 Thin film effects

6.1 Impact of substrate temperature on the critical thickness of blackout in GeTe films

The growth of GeTe was discussed in Chapter 5, where it was observed that the deposition of GeTe on both Si(111)-1x1 and Si(111)-7x7 surfaces begins in an amorphous phase. Wang et al. attribute this to the initial inability of electrons to delocalize, resulting in the material remaining amorphous. Upon reaching a critical thickness, the bonding mechanism changes, allowing the GeTe films to crystallize. It is hypothesized that the critical thickness required for the amorphous-to-crystalline phase transition in GeTe films is primarily influenced by substrate temperature. This hypothesis is based on the idea that overcoming an energy barrier is necessary for the transition, which can be facilitated either by increasing film thickness or by raising the substrate temperature. Therefore, it is expected that higher substrate temperatures will reduce the critical thickness needed for crystallization. Similar temperature-dependent behavior has been observed in SnTe films, where the critical thickness was found to be more influenced by substrate temperature than by the deposition rate.[36] This study aims to test this hypothesis for GeTe films by examining the critical thickness under different temperature conditions.

GeTe film growth exhibits a transition from amorphous to crystalline phases (blackout) on both Si(111)-1x1 and Si(111)-7x7 surfaces. However, the Si(111)-1x1 surface is selected as the preferred substrate for this study due to its broader accessible deposition temperature range of up to 50°C, in contrast to the more restricted 20°C range of the Si(111)-7x7 surface. These observations were supported by in-situ growth monitoring via RHEED. To systematically investigate the temperature dependence of the amorphous-to-crystalline transition in GeTe films, experimental reproducibility was ensured by maintaining a constant growth rate of 0.08 Å/s while varying the substrate temperature. Detailed growth parameters for GeTe are outlined in Chapter 5. It was found that substrate temperatures below 95°C result in an amorphous growth zone, while temperatures above 150°C are too high to enable film growth. Series of experiments were conducted at different substrate temperatures, and RHEED analysis confirmed the preservation of epitaxial relationships

throughout the growth process. RHEED images supporting these observations are presented in the Appendix Figure 0.2.

Figure 6.1 (a) shows RHEED images captured during the growth of GeTe on a Si(111)-1x1 surface. Image (i) shows the highly crystalline substrate surface before deposition. As growth proceeds, the film begins in an amorphous phase, as seen in image (ii). Upon reaching the critical thickness, a phase transition to a crystalline structure is observed, with the appearance of GeTe reflexes as shown in image (iii). To quantitatively determine the critical thickness, the intensity of the specular RHEED spot was measured as a function of growth time. Figure 6.1(b) illustrates that, for a specific temperature, the initial intensity is at a maximum due to the highly crystalline nature of the substrate. As the amorphous layer forms, the intensity gradually decreases. Once the film transitions to the crystalline phase, the specular spot intensity begins to rise again. The plotted data in Figure 6.1 (c) indicates that increasing substrate temperature reduces the critical thickness required for the amorphous-to-crystalline transition, supporting the hypothesis that overcoming an energy barrier is necessary for the transition which can be facilitated either by increasing film thickness or by raising the substrate temperature. For a substrate temperature of 100°C, the critical thickness is 3.6 nm which decreases with rate of 0.052 nm/°C with increasing temperature. At 140°C, the critical thickness for crystallization is nearly 1.4 nm, which is in good agreement with Wang et al.'s findings, where crystallization occurred at around 4 bilayers (1.4 nm, with 1 bilayer = 0.35 nm).

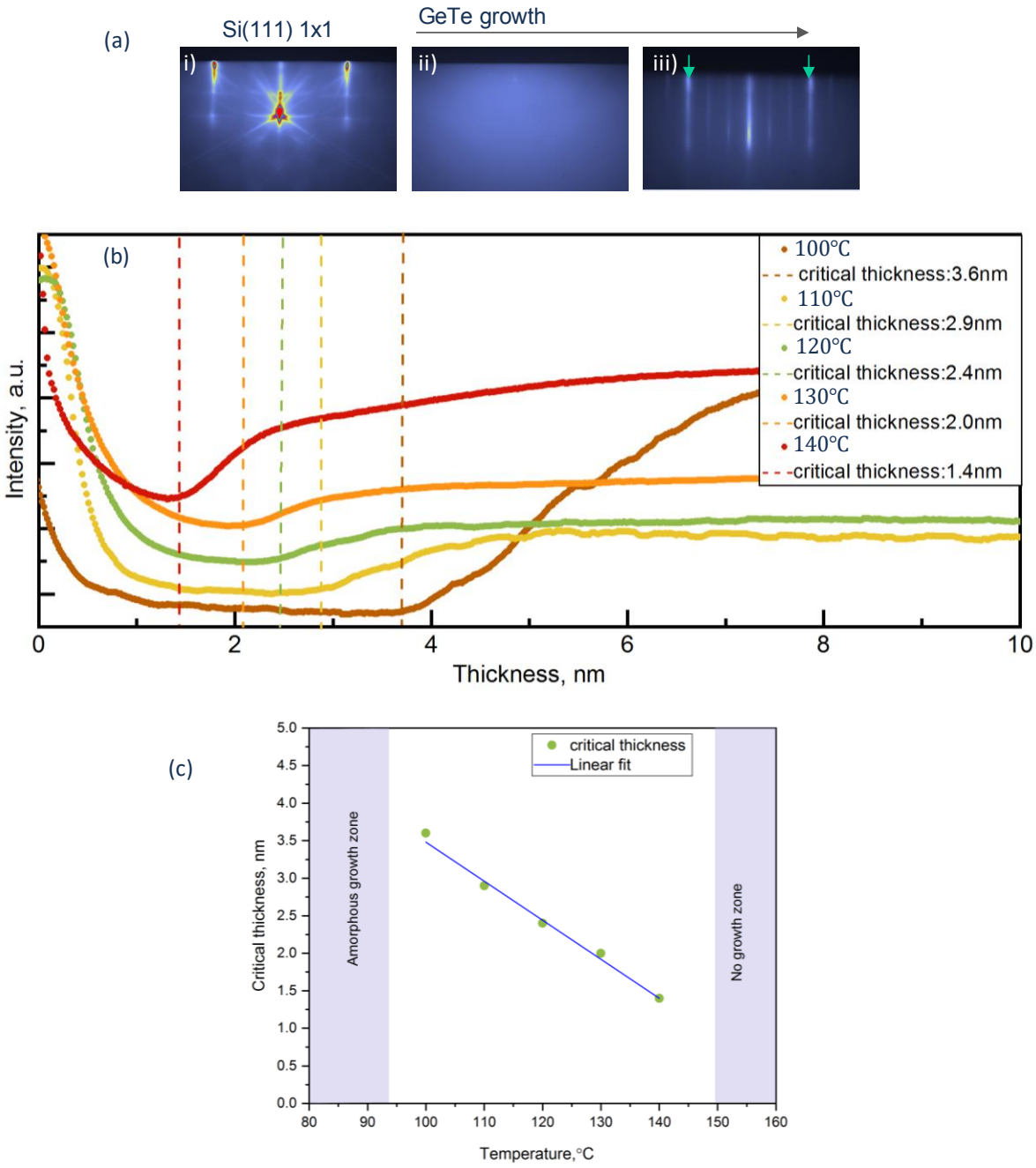

Figure 6.1: (a) shows the RHEED images of GeTe growth on Si(111)1x1 surface,(i) image of si(111)surface taken before growth,(ii) GeTe growth begins with the blackout phase,(iii) indicates the crystalline GeTe. Image (b) represents the analysis of specular spot intensity as function of film thickness for growth conducted at various temperatures. (c) plot of critical thickness vs substrate temperature.

In summary, it is demonstrated that the growth of GeTe films on Si(111)-1x1 substrates transitions from an amorphous to crystalline phase, with the critical thickness for this transition being significantly influenced by substrate temperature. RHEED analysis indicates that temperatures below 95°C result in an amorphous film, while increasing temperatures lead to a decrease in the critical thickness for crystallization. Specifically, at 140°C, a critical thickness of approximately 1.4 nm is observed. This critical thickness is aligning with findings from Wang et al. These findings enhance the

understanding of the growth dynamics of GeTe films and provide valuable insights for optimizing their use in electronic applications.

6.2 Structural changes through confinement in GeTe.

To date, the GeTe films investigated have consistently been deposited with a thickness more than 20 nm. However, previous research has suggested that very thin GeTe films undergo significant structural changes as a result of confinement effects.[8, 60] To investigate these phenomena, a series of GeTe samples with varying thicknesses was deposited. The structures of these samples were analyzed using In-situ RHEED, X-ray diffraction, Ellipsometry and Raman spectroscopy to assess the potential influence of confinement on their properties. This work was conducted in collaboration with M.Sc. Peter Kerres. The GeTe growth on Si(111) surfaces are provide in Chapter 5. Growth on the Si(111) 7×7-reconstructed substrate was selected for this study, to avoid the doping effect which occurs the on the Si(111)-(√3 × √3)R30°-Sb substrate. On this substrate, a conductive surface layer on the silicon wafer is created which complicates the analysis of electrical transport measurements.

Here, we have investigated the in-plane lattice constant with in-situ RHEED while depositing GeTe on the Si(111) 7x7 reconstructed surface. The epitaxial relationship between GeTe film and the silicon substrate was further confirmed through ARHEED and Phi-scan measurements, showing GeTe (-1100)||Si (-110), as explained in Chapter 5. Figure 6.2 presents the evolution of the lattice constant as a function of film thickness, with multiple samples analyzed to ensure reproducibility. At the beginning of the growth, the films have an amorphous structure. Hence the data density is scattered till 2 nm of film thickness. As the film thickness increased, the in-plane lattice constant increased from lower values towards the bulk value, i.e. from ~ 4.11 Å to ~ 4.16 Å. This corresponds to an approximate 1.21% increment in lattice parameters. Figure 6.3 shows the analysis of the 60 nm thick film, which indicates the major deviations in the in-plane lattice shift are present in the thinner films that are below 7nm, while the minor deviations are observed in thicker films that are 15-20 nm. Film thickness from 20 nm to 60 nm shows no deviation in lattice constant as shown in Figure 6.3. This lattice shift is further confirmed by RSM analysis for the (-1100) peak.[105] The fact that the same trends are observed by RHEED during deposition and by XRD after deposition indicates that the distortion is already formed during deposition and is thus an inherent film property. These lattice shifts indicate the distortion in crystal structure. Furthermore, DFT calculations of freestanding GeTe slabs as presented by Wang et al. show a similar behavior of the in-plane lattice constant which implies that the change is not governed by strain imposed from the substrate. In addition, the out of plane lattice constant as a function of film thickness has been studied by XRD θ-2θ scans as shown in Figure 6.4. In all films only the (0003n) GeTe family peaks are present apart from the substrate peaks, indicative of highly textured crystalline films. The (0003n) peaks broaden due to the finite film thickness and gradually shift towards lower values in Q-space and thus higher lattice constants for ultrathin films. Figure 6.5 shows that the out of lattice constant shift is pronounced up to 10 nm of film thickness. Both in-plane and out of plane lattice constant shifts with film thickness. This serves as indication of change in atomic arrangements with film thickness.

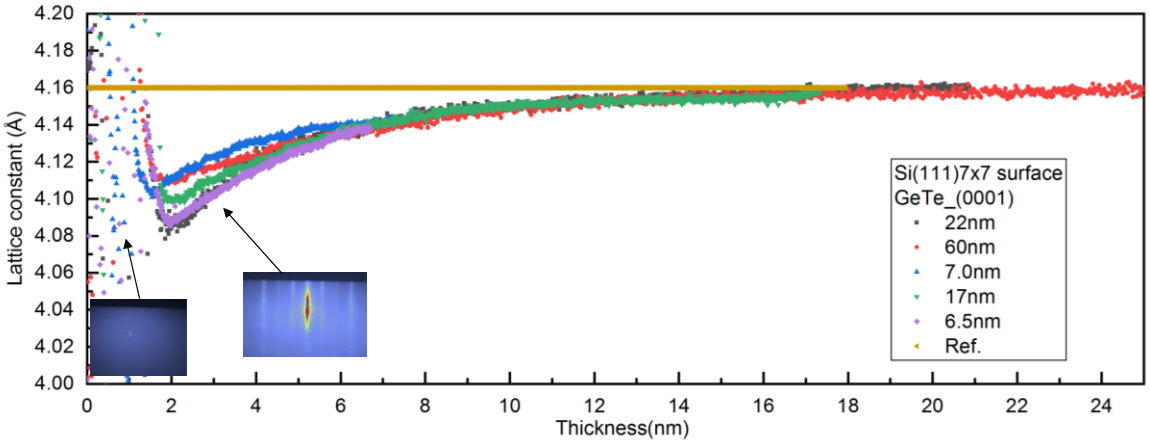

Figure 6.2: Analysis of the in-plane lattice constant of GeTe films as a function of film thickness via RHEED. Films thinner than ~2 nm exhibit an amorphous state, resulting in scattered data density in this region. As the film thickness increases beyond 2 nm, crystalline growth allows for lattice constant analysis, revealing a shift in the lattice constant with increasing film thickness. This trend was confirmed through the analysis of multiple films. [published work [105]]

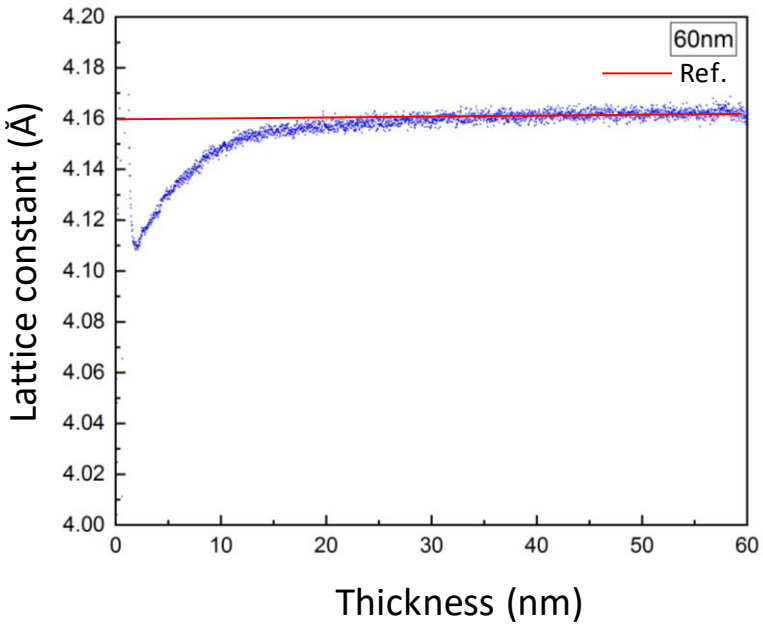

Figure 6.3: : Analysis of in-plane lattice constant of GeTe films as function of film thickness upto 60nm. [published work [105]]

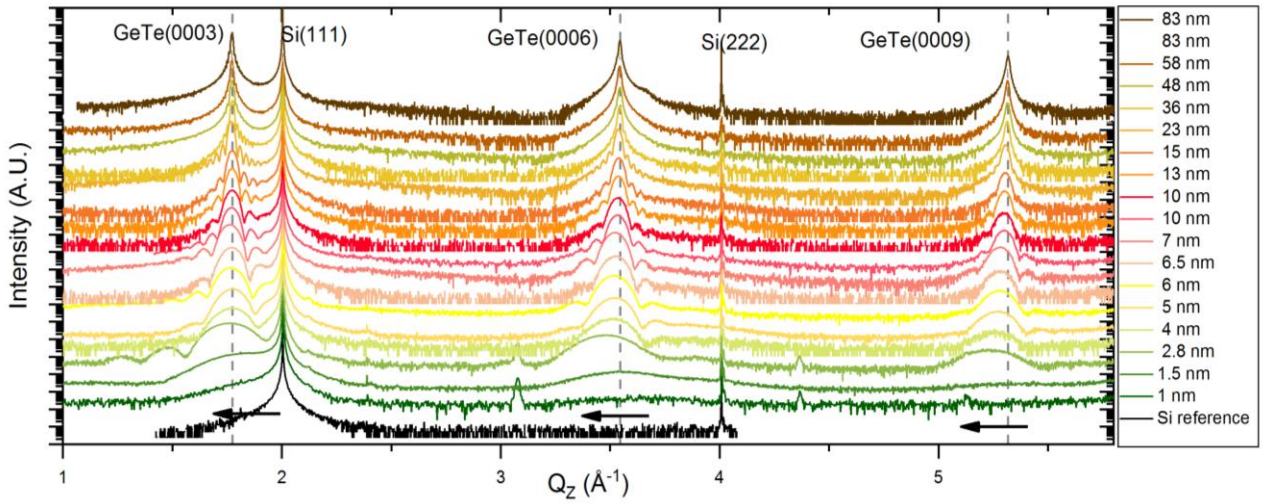

Figure 6.4: X-ray diffraction $\theta - 2\theta$ scans measurements of crystalline GeTe films for different thicknesses, which are textured in (0001) direction and show Laue fringes besides the main diffraction peaks. The (0003n) peaks show a thickness dependent distortion towards lower Bragg angles and a larger out of plane lattice constant in ultrathin films. The dashed lines, given for reference, indicate the shift in the out-of-plane lattice constant in the thinner films. [published work [105]]

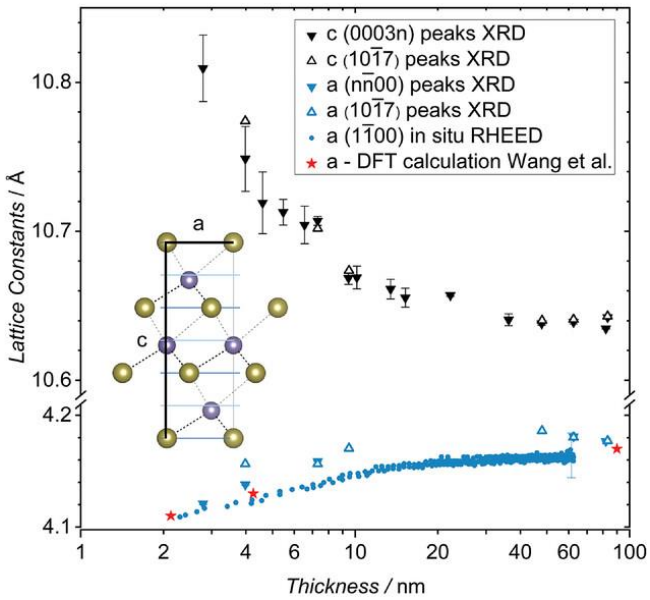

Figure 6.5: In-plane and out of plane lattice constants obtained as function of film thickness. Closed triangles correspond to values obtained from reflections with h, k, or l = 0, while open triangles represent data from reciprocal space maps of the (10 7) peaks. Closed circles indicate lattice parameters measured via RHEED during the growth of the 62.5 nm sample. Red stars mark in-plane lattice parameters from simulated freestanding GeTe films by Wang et al.[60] The results consistently indicate that ultrathin films undergo lattice distortion, with an increase in the c-axis parameter and a decrease in the a-axis parameter. The inset was created using VESTA. [published [105]]

A similar study of the confinement effect was attempted on SnTe (001) films grown on the Si(111) 1×1 surface with limited film thickness. However, no pronounced lattice shifts were observed in both RHEED and XRD θ-2θ scans. The minimum film thickness investigated in this study was 5 nm, as further reduction was constrained by the film's coverage limitations on the substrate. Detailed discussions regarding film growth are provided in Chapter 5. Figure 6.6 shows the θ-2θ scan, in which only the (002n) family peaks are present alongside the substrate peaks, indicating highly textured crystalline films. Laue fringes around all lattice peaks ((002), (004), and (006)) are visible for the thicker films shown in (b, c, d). The values in Q space do not show a variation with film thickness, indicating that the out-of-plane lattice constant remains constant in contrast to the GeTe films. The calculated out-of-plane lattice constant from XRD is 6.33 ± 0.02 Å, and the in-plane lattice constant calculated from RHEED is approximately 6.31 Å for the thicker films. These values are in close agreement with the reported bulk values.[86]

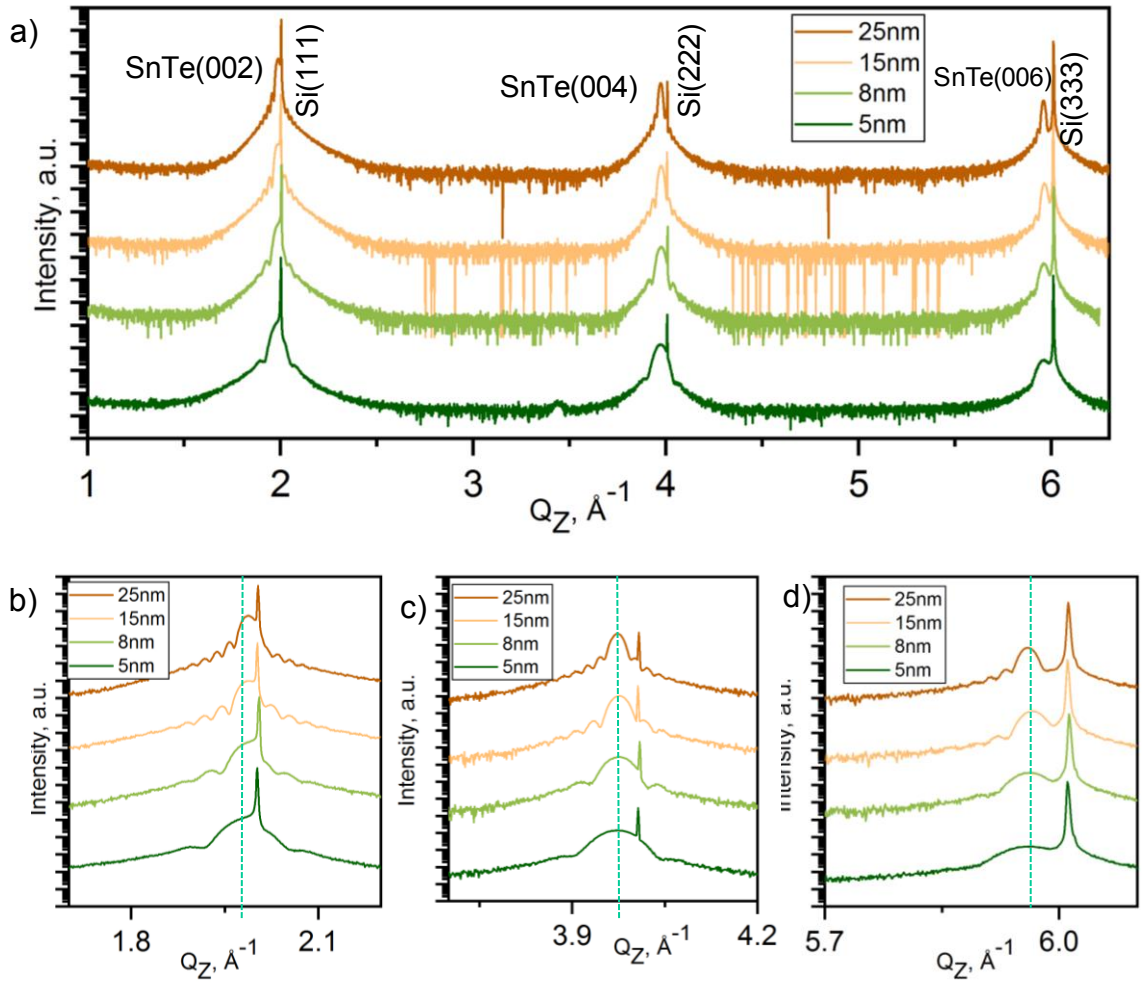

Figure 6.6: θ − 2θ scans of the thickness series for SnTe. All films were deposited on a Si(111) 1x1 substrate and capped with about 20nm Al_2O_3.The (002) peak family of all samples is clearly visible. Laue-oscillations indicate a low roughness, although they become rather weak for the thinner films. (b,c,d) close ups of the (002n) peaks for the films.

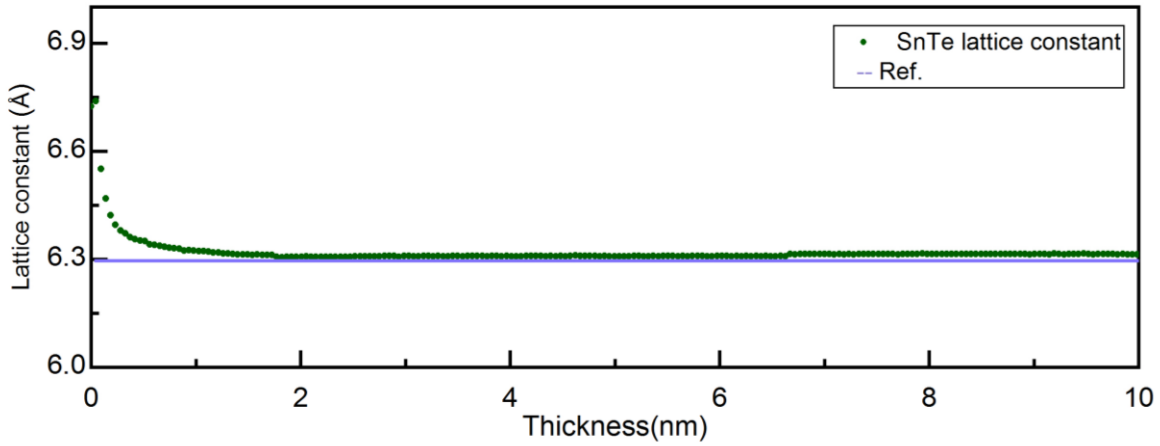

Figure 6.7: Analysis of in-plane lattice constant of SnTe films as function of film thickness via RHEED.

In summary, this study investigated the structural changes in ultra-thin films of GeTe (0003) films grown over Si(111) 7x7 reconstructed surface. In-situ RHEED and XRD revealed that as the film thickness increased, both in-plane and out-of-plane lattice constants shifted toward bulk values, with pronounced distortions observed in films thinner than 10 nm. The findings highlight the significant influence of film thickness on the structural properties of GeTe. In contrast, a similar study on SnTe (001) films grown on Si(111) 1×1 surfaces showed no significant lattice shifts in either RHEED or XRD θ-2θ scans. The minimum film thickness examined was 5 nm, constrained by limitations in substrate coverage at lower thicknesses. XRD analysis revealed only (002n) family peaks, indicating highly textured crystalline films, with Laue fringes visible around thicker film peaks.

6.3 SnSe Phase transition from Pnma towards Cmcm in ultra-thin film thicknesses

The motivation behind this study is to address the lack of fundamental understanding of the structural properties, electronic behavior, and thermal conductivity of few-layer SnSe, a material known for its superior thermoelectric performance.[99] While bulk SnSe has been widely studied, little is known about how its properties change at reduced thicknesses, particularly in the two-dimensional (2D) limit. The recent DFT calculation reported by Xue et al. reveals significant structural changes in SnSe as the number of atomic layers decreases.[106] Their study indicates that 4 layers of SnSe show bulk-like structural properties, with Pnma symmetry dominating at room temperature. This phase stability is largely influenced by the Peierls distortion, which stabilizes the structure by breaking symmetry. As the thickness decreases, the competitive coupling between the Peierls distortion and phonon anharmonicity becomes more pronounced. These layers exhibit an increased instability, deviating from the bulk Pnma phase and transitioning towards a less stable structure. In the thinnest layer, 1L SnSe, a significant structural change occurs with a phase transition from Pnma to the higher-symmetry Cmcm phase. This transition is driven primarily by strong phonon anharmonicity, rather than the Peierls distortion. Therefore, it is worth to investigate this structural transition experimentally by depositing ultra-thin SnSe films via MBE and characterizing them using techniques such as XRD, RSM, and Raman spectroscopy.

In Chapter 5, the growth conditions for highly textured SnSe (h00) films on three different Si(111) surfaces were discussed. It was found that the growth of SnSe films on the Si(111) 1×1 surface resulted in the highest quality compared to the Si(111) 7×7 reconstructed surface and the Si(111) surface with a (√3 × √3)R30°-Sb termination. Consequently, the quantum confinement effects in ultra-thin films of SnSe grown on the Si(111) 1×1 surface are now being investigated.

To characterize the structure of SnSe thin films an XRD θ - 2θ scan is performed. Figure 6.8 shows the measurements of all samples. In all films only (200n) SnSe family peaks are present apart from the substrate peaks, indicative of highly textured crystalline films. The (002n) peaks broaden due to the finite film thickness and gradually shift towards lower values in Q-space and thus higher lattice constants for ultrathin films. The calculated a-axis lattice constant for thicker film (31.8 nm) using (200) peak is ~11.509Å, which is in good agreement with reported value 11.49 Å.[99] Further, these out of plane lattice constant shifts with changing film thickness are conformed via reciprocal space mapping of the (400) peak shown in Figure 6.9. The peak at 2 $Å^{-1}$ belongs to the silicon substrate. Results from RSM supports the trend observed in the θ-2θ scan measurement, at lower film thickness, out of plane lattice constant is exceeding the bulk value. All samples were measured via XRR to determine the film thickness; measurements are given in the Appendix in Figure 0.3 . Further investigation for in-pane lattice constant of b and c axes are conducted via reciprocal space mapping of (020) and (002) peaks, respectively shown in Figure 6.11. These measurements are essential for understanding how the in-plane lattice parameters change with film thickness, complementing the out-of-plane analysis provided by the θ-2θ scans and RSM. All XRD Measurements were taken in collaboration with Dr. Jalil Abdur Rehman.

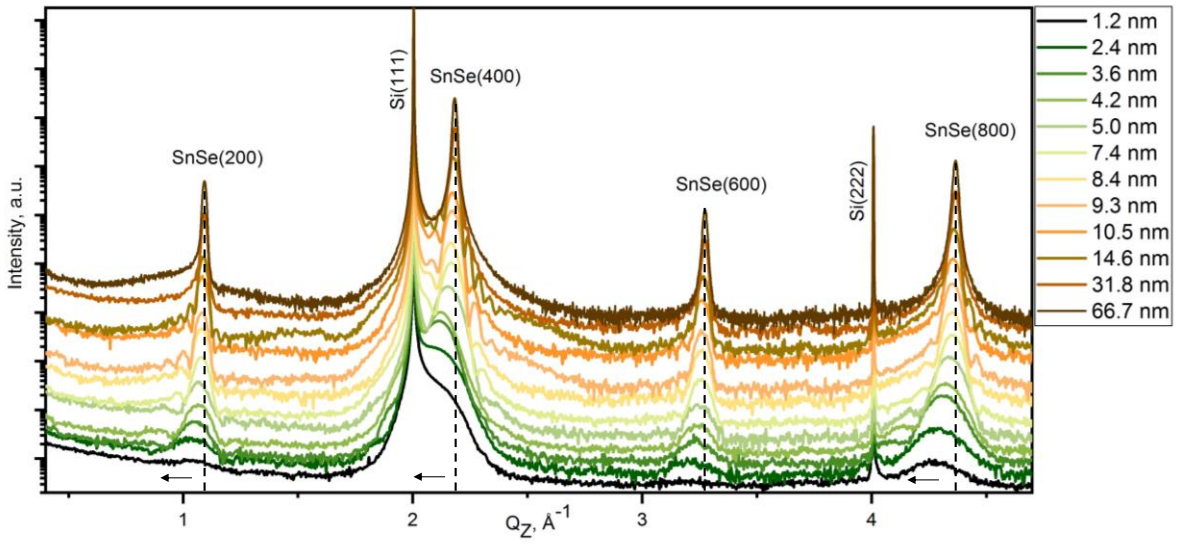

Figure 6.8: : X-ray diffraction $\theta - 2\theta$ scan measurements of crystalline SnSe films for different thicknesses, which are textured in (100) direction. The (200n) peaks show a thickness dependent distortion towards lower Bragg angles and a larger out of plane lattice constant in ultrathin films. Black lines are included as a reference to highlight the peak shifts with decreasing film thickness.

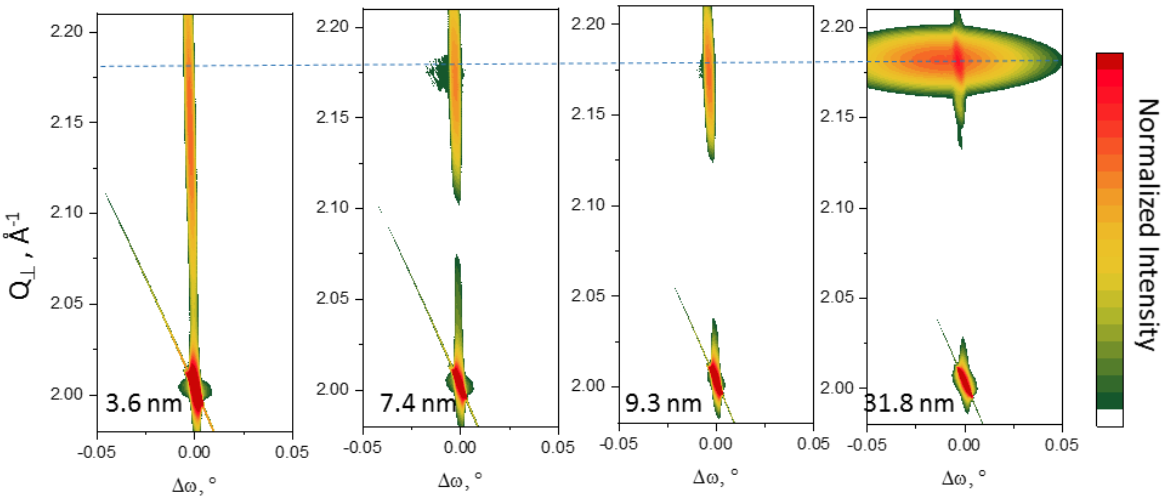

Figure 6.9: Reciprocal space mapping of (400) peak of SnSe films of various thickness. The blue dashed line indicates that as the film thickness decreases, the out-of-plane lattice constant shifts to higher values.

Figure 6.11 shows the combination of RSMs of samples of different thickness. The in-plane RSM of (020) and (002) peaks shows the gradual shift with film thickness in Q space. Both peaks are shifting towards each other as film thickness is reducing. This observation suggests the both b and c axes, i.e. the in-plane lattice constants are changing with film thickness. The resulting lattice constants for thicker film (31.8nm) are ~ b= 4.395Å and ~ c= 4.194 Å , resulting b/c value 1.047. The previously reported experimental in-plane values for bulk phase SnSe (Pnma phase) are b= 4.450 Å and c= 4.150 Å and the theoretical values are b= 4.524 Å and c= 4.2190 Å, and for both cases the b/c value is 1.072. For the film thickness (3.6nm) both lattice constants b= 4.333 Å and c= 4.231 Å deviate from the bulk values. This suggests, as the film thickness is reduced, that the in-plane lattices are adjusting in symmetric manner. The aspect ratio b/c decreases from 1.047 (31.8nm film) to 1.024 (3.6nm film), indicating that the anisotropy between the lattice parameters is reduced upon the decrease of the film thickness. This is in good agreement with DFT calculations reported by Xue et al.[106] Figure 6.10 (i) shows the lattice constant b and c for different film thicknesses. The graph suggests that deviations of the in-plane lattices are pronounced below 10 nm of film thickness in both dimensions. Figure 6.10 (ii) shows the out of plane lattice constant a follows the same trend. As the film thickness reduces, the lattice constant is shifting towards higher value 11.509 Å to 11.865 Å (3.6 nm film). These observations are in line with the DFT calculated shifts by Xue et al., suggesting that the with reducing film thickness the crystal structure is transiting from the Pnma phase to the higher symmetric Cmcm phase.

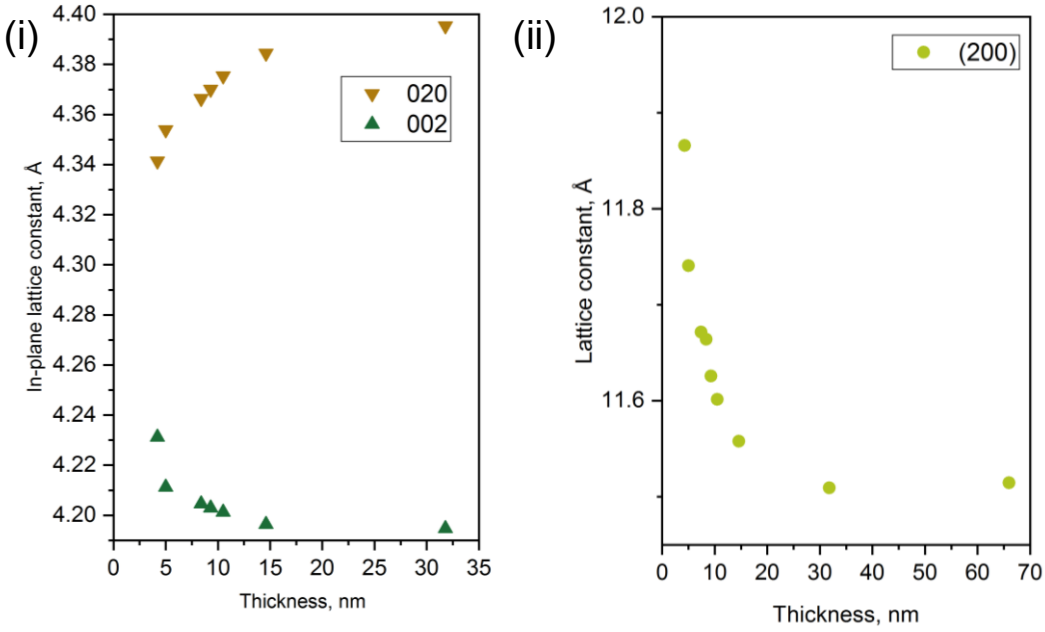

Figure 6.10: (i) In-plane lattice constants b and c are obtained as function of film thickness, (ii) out of plane lattice constants a plotted as a function of film thickness.

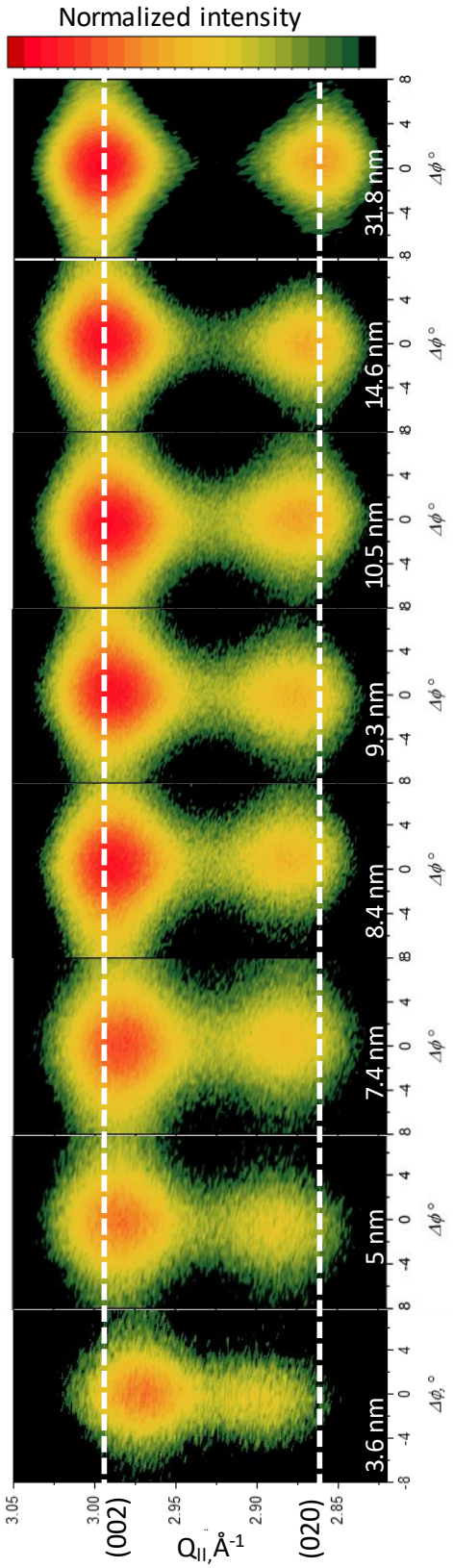

Figure 6.11: In plane reciprocal space maps of the (002) and (020) Peaks for different thickness reveal that the in-plane lattice constants are shifting towards each other in ultra-thin films. The dashed lines are included as a reference to highlight the peak shifts with reducing film thickness.

In plane reciprocal space maps of the (002) and (020) peaks for different thickness reveal that the in plane lattice constant values are shifting towards each other in ultra-thin films. The transition from the Pnma phase to the Cmcm phase involves a structural rearrangement that typically results in a volume expansion. Figure 6.12 shows the volume change of the unit cell as function of film thickness.

The unit cell volume changes with the film thickness as shown in figure. As the film thickness reduces the crystal structure transitions from Pnma to Cmcm and vice versa. The unit cell volume for (31.6nm film) is ~ 212.203 $Å^3$, which is in good agreement with previously reported Pnma phase ~212.29$Å^3$. For thinner film (3.6 nm), the unit cell volume changes to ~ 217.96 $Å^3$, in good agreement with Cmcm phase ~ 217.12 $Å^3$.[99]

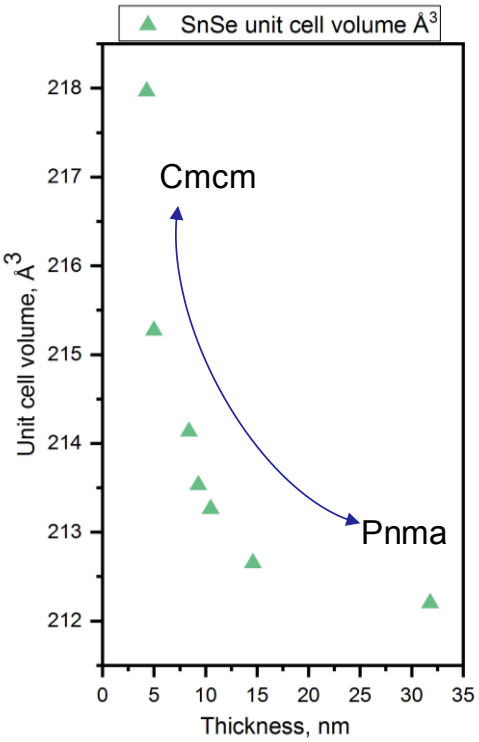

Figure 6.12:The unit cell volume shows a thickness dependent shift for thin films of SnSe grown on Si(111) 1x1 *surface. The unit cell volume for thicker film is ~212.203 $Å^3$ and thinner film is ~217.96 $Å^3$.*

All observations from XRD are suggesting that a phase transition from lower symmetric Pnma towards higher symmetric Cmcm structure occurs with decreasing film thickness. Further this change in structure can be confirmed by analyzing vibrational modes as shown next.

Raman measurements were performed using a laser wavelength of 532 nm on a WITecalpha300R confocal microscope. Spectra were recorded using a 100× objective under ambient conditions. Low laser energy (0.1 mW) was used for the Raman measurements to avoid laser-induced damage of the SnSe samples, which were sensitive to heat. Measurements were performed on various spots to ensure representative results and the homogeneity of the sample. Measurements are conducted in collaboration with Dr. Mohit Raghuwanshi.

In order to characterize the thickness dependency of vibration modes of the lattice and the phase components in the samples, Raman spectroscopy of the SnSe films were investigated. As shown in Figure 6.13 (a) the spectra reveal five main vibrational modes for thicker film (60 nm) at 29 cm^{-1}, 67 cm^{-1}, 103 cm^{-1}, 122 cm^{-1} and 149 cm^{-1}, in which the peak at 103 cm^{-1} belongs to the B_{3g} phonon mode and the other three belong to A_g phonon modes. These modes are in good agreement with previously reported bulk samples. Raman modes B_{3g} and A_{2g} belong to the in-plane vibration mode, while the remaining A_g modes belong to the interlayer vibration modes. All the observed vibrational modes agree well with the characteristic modes of orthorhombic SnSe crystals, which are stable at ambient conditions.

As the film thickness decreases, the Raman peaks at 103 cm^{-1} shows the most significant red shit, which gives further confirmation of structural changes upon reducing film thickness. The pronounced shift is observed in films less than 5nm, which is in good agreement with theoretical calculation presented by Xue et al. Nevertheless, a pronounced shift is only observed for B_{3g} mode, while the shift in A_g mode at 120 cm^{-1} is not significant as shown in Figure 6.13 (b). In particular, 1.2 nm film is a challenge, since the number of scattering centers decreases as the thickness of SnSe reduces. Hence, measuring the intensity of the Raman signal vanishes due to the limitation of the Raman spectrometer.

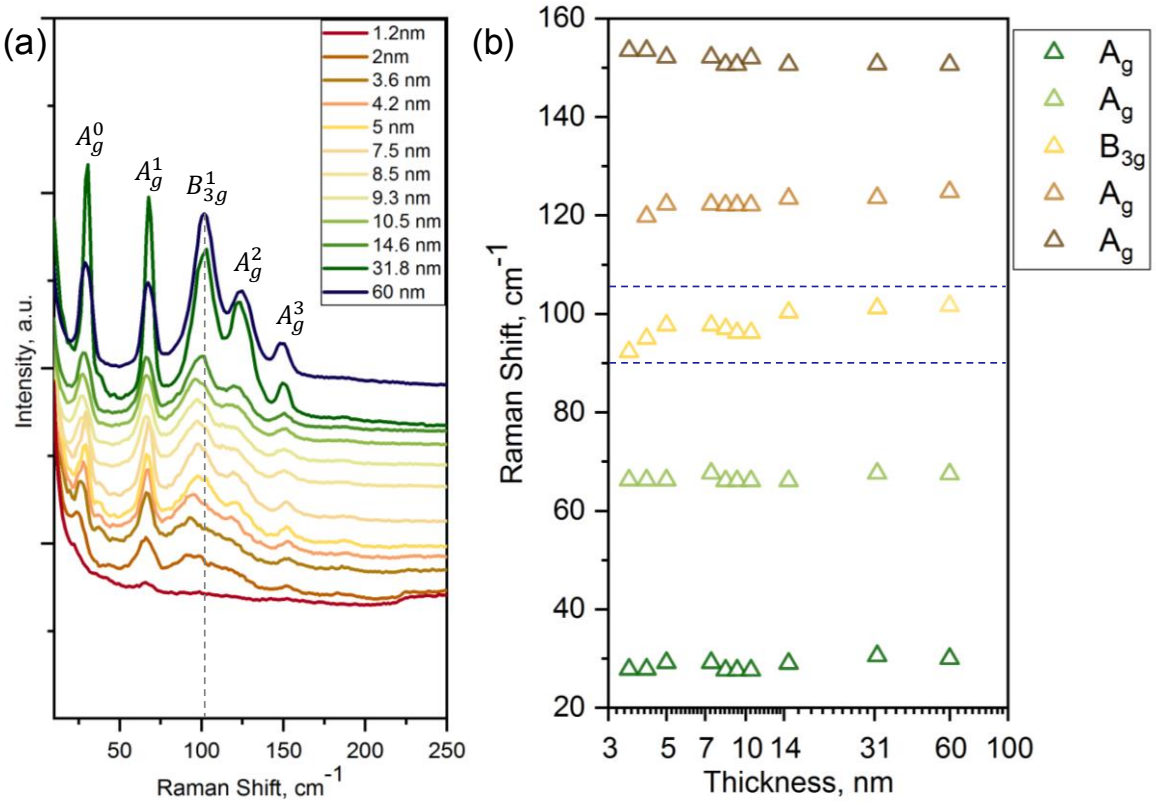

Figure 6.13: (a) Raman measurements of the thickness series of SnSe. The measurements were conducted using laser wavelength of 532 nm. The black line is included as reference to highlight the peak shit. (b plot of thickness dependent shifts of the SnSe modes.

This study has investigated the structural evolution of SnSe in ultra-thin films, motivated by the material's superior thermoelectric properties and the limited understanding of its behavior at reduced thicknesses. Using Raman spectroscopy and X-ray diffraction, significant lattice distortions and phase transitions were observed as the film thickness decreases. In films thinner than 5 nm, a pronounced redshift in the B_{3g} phonon mode was detected, indicative for structural changes. XRD analysis confirmed shifts in the lattice constants, particularly below 10 nm, suggesting a transition from the bulk orthorhombic Pnma phase to a higher-symmetry Cmcm phase. These findings are consistent with density functional theory (DFT) calculations reported in [106] and provide valuable insights into the structural behavior of SnSe in its two-dimensional form.

7 Conclusion and Outlook

In conclusion, a systematic investigation into the epitaxial growth and thin-film effects of GeTe, SnTe, and SnSe on various Si(111) surfaces has yielded valuable insights into their structural evolution. The study highlights the distinct influences of substrate type, temperature, and thickness on each material's structural properties. Key findings include:

- The epitaxial growth of GeTe thin films on various Si(111) substrates, including Si(111)-(7x7) reconstructed, Si(111)-(√3 ×√3)R30°-Sb terminated, and Si(111)-1x1 surfaces, was thoroughly investigated, yielding results consistent with prior literature. RHEED analysis displayed sharp streak patterns, confirming smooth, well-defined film surfaces, highlighting a transition from an amorphous to a crystalline phase on both the Si(111)-1x1 and Si(111)-(7x7) surfaces. A detailed investigation into GeTe growth on the Si(111)-1x1 surface demonstrated that increasing the substrate temperature decreases the critical thickness at a rate of 0.054 Å/°C, with a minimum thickness of 1.4 nm observed at 140°C, aligning with earlier findings. Further ARHEED and XRD ϕ-scan analyses revealed complex domain formations on the Si(111)-(7x7) surface, with twisted domains occurring at ±2.4° and ±7.3°. Additionally, a thickness-dependent study of GeTe films on the Si(111)-(7x7) surface showed significant shifts in both in-plane and out-of-plane lattice constants for films below 10 nm, indicating notable structural changes. Collectively, these findings emphasize the substantial impact of temperature and thickness on the structural characteristics of GeTe films. To gain a deeper understanding of the nature of chemical bonding at varying film thicknesses, further analyses—such as Raman shifts, dielectric constants, and electrical transport properties—have been pursued by collaborators in the research team.

- Similarly, a comparative analysis of SnTe growth on various Si(111) surfaces was conducted, which involved a detailed examination of the rotational domains in the films using ARHEED and ϕ-scan techniques. The combination of the threefold symmetry of the Si(111) substrate and the fourfold symmetry of the SnTe(001) film results in the formation of a twelvefold symmetry within the SnTe layer, consisting of three energetically equivalent rotational domains on the Si(111) 1x1 surface. In contrast, SnTe growth on the Si(111)-(√3 ×√3)R30°-Sb terminated surface exhibited significant suppression of two domains, while growth on the 7x7 reconstructed surface resulted in a higher degree of rotational domains, indicating 24-fold symmetry in the ARHEED data. To investigate the effects of thin films, growth on the Si(111) 1x1 surface was selected based on RHEED analysis. The minimum film thickness examined was 5 nm, constrained by limitations in substrate coverage at thinner dimensions. As a result, further optimization is necessary for conducting electrical measurements on ultra-thin films. Unlike GeTe, SnTe(001) has not exhibited significant lattice shifts in either the in-plane or out-of-plane orientations, as analyzed via RHEED and XRD θ-2θ scans. In the future, investigating the growth of SnTe(111) may provide insights into the directional dependency of distortions within the crystal system.

- The growth of highly textured SnSe (100) films on Si(111) surfaces—specifically on Si(111)-(√3×√3)R30°-Sb terminated, Si(111) 1x1, and Si(111) 7x7 reconstructed surfaces—was achieved. RHEED analysis indicated that growth on the (√3×√3)R30°-Sb terminated surface was notably complex. During the initial stages of growth, the surface exhibited a 1x1 reflex for 180 seconds, denoted as an intermediate stage, and a delay in the appearance of reflexes corresponding to SnSe was observed. To understand this intermediate stage, further investigations are required. In contrast, SnSe growth on the Si(111) 1x1 and 7x7 surfaces displayed rapid surface coverage and crystalline formation. XRD analysis confirmed that SnSe films demonstrated a strong (100) out-of-plane orientation across all three Si(111) surfaces, with lattice constants and unit cell volumes consistent with those of bulk SnSe in thicker films (30 nm). In-plane domain structures were further investigated using ϕ-scans and ARHEED measurements, revealing three rotational domains for SnSe films on the Si(111) 1x1 and Sb-terminated surfaces. The 7x7 surface exhibited more complex domain behavior, including additional twisted domains. Notably, the XRD and RHEED data indicated that the SnSe(100) film grown on the Si(111) 1x1 surface exhibited the highest quality crystalline structure among all the studied surfaces. Building on these observations, the thickness-dependent structural changes in SnSe films grown on the Si(111) 1x1 surface were investigated. Through Raman spectroscopy and XRD, significant lattice distortions and phase transitions were observed as the film thickness decreased. In films thinner than 5 nm, a pronounced redshift in the B_{3g} phonon mode was detected, indicating structural changes. XRD analysis revealed shifts in the lattice constants, particularly below 10 nm, suggesting a transition from the bulk orthorhombic Pnma phase to a higher-symmetry Cmcm phase. These findings align with theoretical calculations presented in the literature and provide valuable insights into the structural behavior of SnSe in its two-dimensional form.

Appendix

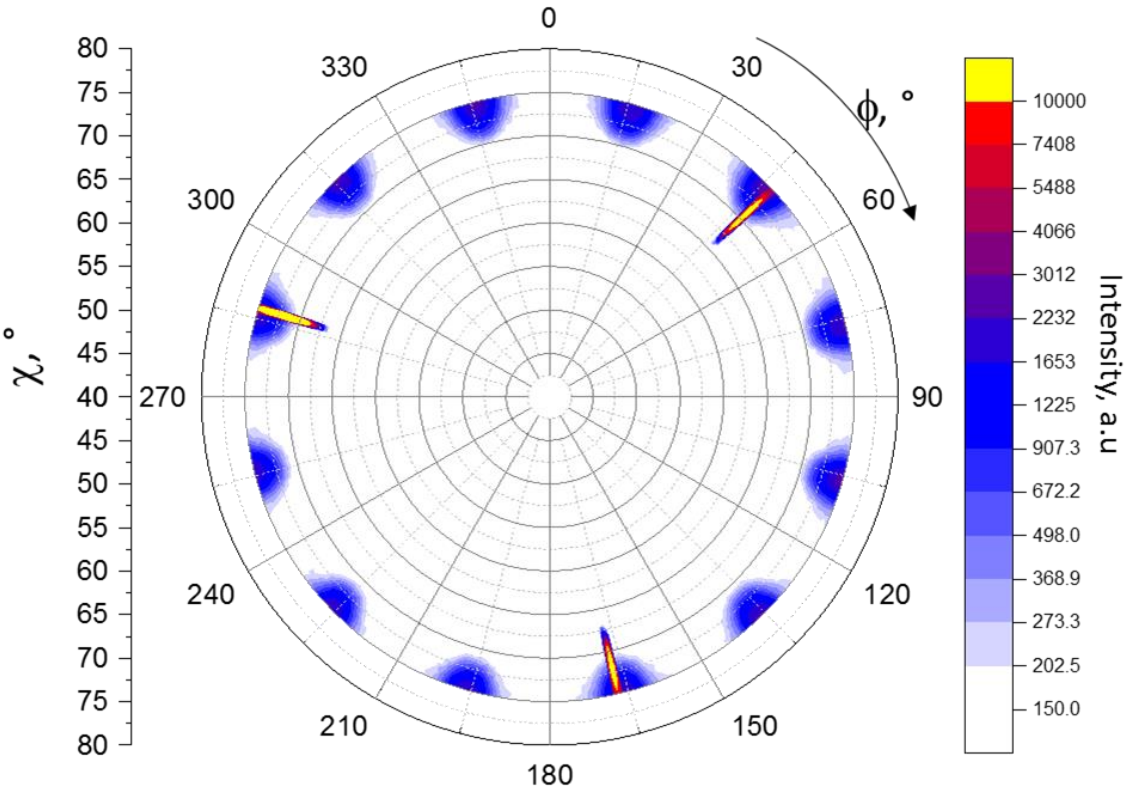

Figure 0.1: Pole figure of (111) plane (2ϑ = 30.44°) SnSe film grown over Si(111) 1x1 surface showing twelve poles (blue circles) corresponding to 3 domains. Additionally, three poles belong to Si substrate (-111) peaks.

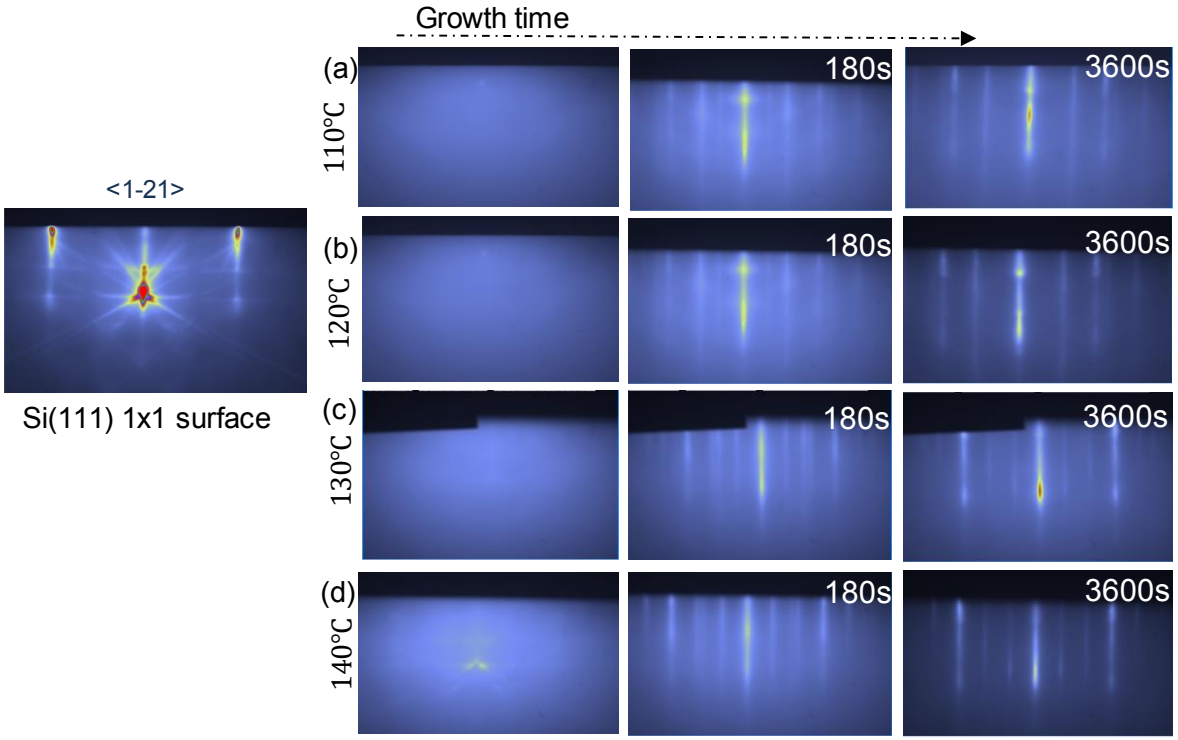

Figure 0.2: RHEED images taken during growth of GeTe on Si(111) 1x1 surface at various substrate temperature.

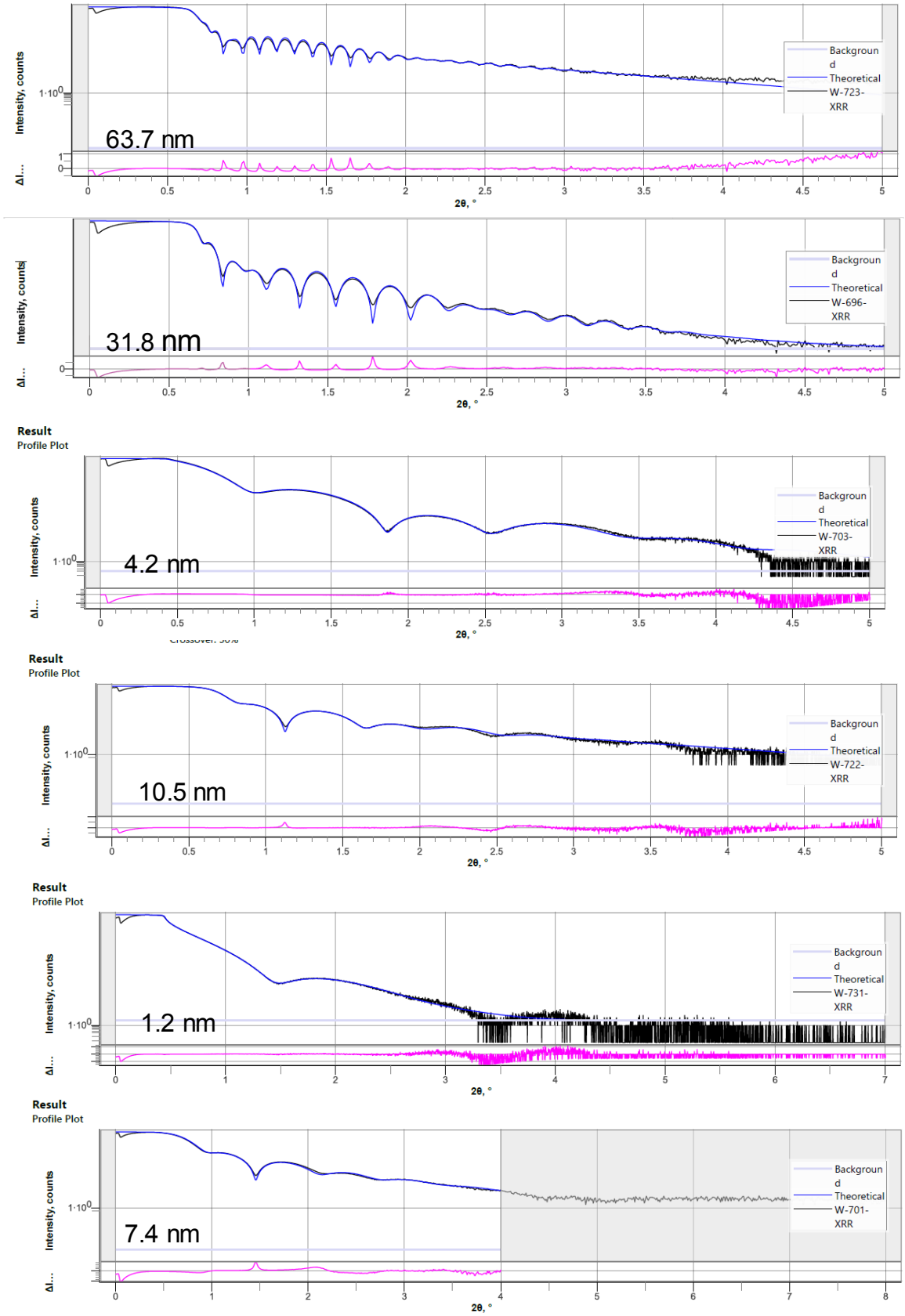

Figure 0.3: Shown are XRR measurements and fits of the SnSe thickness series. All films were deposited on a Si(111) 1x1 surface on double side polished substrate and capped with Al2O3.

Bibliography

1. Zhang W, Mazzarello R, Wuttig M, Ma E. Designing crystallization in phase-change materials for universal memory and neuro-inspired computing. *Nat Rev Mater.* 2019 Mar;4(3):150–68.

2. Wuttig M, Yamada N. Phase-change materials for rewriteable data storage. *Nat Mater.* 2007 Nov;6(11):824–32.

3. Lotnyk A, Behrens M, Rauschenbach B. Phase change thin films for non-volatile memory applications. *Nanoscale Adv.* 2019 Oct 9;1(10):3836–57.

4. Kersting B, Salinga M. Exploiting nanoscale effects in phase change memories. *Faraday Discussions.* 2019;213:357–70.

5. Kooi BJ, Wuttig M. Chalcogenides by Design: Functionality through Metavalent Bonding and Confinement. *Advanced Materials*. 2020;32(21):1908302.

6. Raty JY, Wuttig M. The interplay between Peierls distortions and metavalent bonding in IV–VI compounds: comparing GeTe with related monochalcogenides. *J Phys D: Appl Phys.* 2020 Apr;53(23):234002.

7. Raty JY, Schumacher M, Golub P, Deringer VL, Gatti C, Wuttig M. A Quantum-Mechanical Map for Bonding and Properties in Solids. *Advanced Materials.* 2019;31(3):1806280.

8. Ronneberger I, Zanolli Z, Wuttig M, Mazzarello R. Changes of Structure and Bonding with Thickness in Chalcogenide Thin Films. *Advanced Materials.* 2020;32(29):2001033.

9. Yu Y, Cojocaru-Mirédin O, Wuttig M. Atom Probe Tomography Advances Chalcogenide Phase-Change and Thermoelectric Materials. *Physica Status Solidi A*. Epub 2024 [cited 2024 Oct 1]:2300425.

10. Lin N, Han S, Ghosh T, Schön CF, Kim D, Frank J, et al. Metavalent Bonding in Cubic SnSe Alloys Improves Thermoelectric Properties over a Broad Temperature Range. *Advanced Functional Materials.* 2024;34(30):2315652.

11. Franssila S. *Introduction to Microfabrication*. John Wiley & Sons; 2010. 535 p.

12. Reinhardt K, Kern W. *Handbook of Silicon Wafer Cleaning Technology.* William Andrew; 2018. 794 p.

13. Mortelmans W, De Gendt S, Heyns M, Merckling C. Epitaxy of 2D chalcogenides: Aspects and consequences of weak van der Waals coupling. *Applied Materials Today*. 2021 Mar 1;22:100975.

14. Royer L. Recherches expérimentales sur l'épitaxie ou orientation mutuelle de cristaux d'espèces différentes. [Internet]. 1928 [cited 2024 Aug 3]. Available from: https://www.persee.fr/doc/bulmi_0366-3248_1928_num_51_1_4034

15. Narayan J, Larson BC. Domain epitaxy: A unified paradigm for thin film growth. *Journal of Applied Physics.* 2003 Jan 1;93(1):278–85.

16. Tuoc VN. First Principle Study on the Domain Matching Epitaxy Growth of Semiconductor Hetero-Interface. *Materials Transactions.* 2008;49(11):2491–6.

17. Bosi M, Attolini G. Germanium: *Epitaxy and its applications. Progress in Crystal Growth and Characterization of Materials*. 2010 Sep 1;56(3):146–74.

18. Myers MA, Lee JH, Bi Z, Wang H. High quality p-type Ag-doped ZnO thin films achieved under elevated growth temperatures. *J Phys Condens Matter.* 2012 Apr 11;24(14):145802.

19. Narayan J, Tiwari P, Chen X, Singh J, Chowdhury R, Zheleva T. Epitaxial growth of TiN films on (100) silicon substrates by laser physical vapor deposition. *Applied Physics Letters.* 1992 Sep 14;61(11):1290–2.

20. Boschker JE, Momand J, Bragaglia V, Wang R, Perumal K, Giussani A, et al. Surface Reconstruction-Induced Coincidence Lattice Formation Between Two-Dimensionally Bonded Materials and a Three-Dimensionally Bonded Substrate. *Nano Letters.* 2014;14(6):3534–8.

21. Grundmann M. Formation of epitaxial domains: Unified theory and survey of experimental results. *Phys Status Solidi B*. 2011;248(4):805–24.

22. Woodruff DP, King DA. *The Chemical physics of solid surfaces.* Amsterdam, Oxford: Elsevier; 1997. xxi, 650 p.

23. Ptak AJ. Principles of molecular beam epitaxy. In: Kuech TF, editor. *Handbook of Crystal Growth* [Internet]. 2nd ed. Boston: North-Holland; 2015. p. 161–92. Available from: https://www.sciencedirect.com/science/article/pii/B9780444633040000044

24. Minchev G, Eddrief M, Trendafilov L, Naradikian H, Trendafilov K. Investigation of Se molecular beams used for MBE. *Vacuum*. 1996 Feb 1;47(2):157–65.

25. King DA, Woodruff DP. *The chemical physics of solid surfaces*. 1st ed. Amsterdam: Elsevier; 1997.

26. Voigtländer B, Zinner A. Influence of surfactants on the growth-kinetics of Si on Si(111). *Surface Science.* 1993;292(1):L775–80.

27. Aliofkhazraei M. Wetting and wettability [Internet]. London: IntechOpen; 2015 [cited 2024 Jul 31]. Available from: https://www.intechopen.com/books/5319

28. Rich DH, Franklin GE, Leibsle FM, Miller T, Chiang TC. Synchrotron photoemission studies of the Sb-passivated Si surfaces: Degenerate doping and bulk band dispersions. *Phys Rev B.* 1989 Dec 15;40(17):11804–16.

29. Bennett MR, Cafolla AA, Cairns JW, Dunscombe CJ, Williams RH. Photoemission studies of the interactions of CdTe and Te with Si(100). *Surface Science.* 1996 Jul 10;360(1):187–99.

30. Yang P, Zhang S, Pan S, Tang B, Liang Y, Zhao X, et al. Epitaxial Growth of Centimeter-Scale Single-Crystal MoS2 Monolayer on Au(111). *ACS Nano.* 2020 Apr 28;14(4):5036–45.

31. Braun W, editor. *Kikuchi lines. In: Applied RHEED: Reflection High-Energy Electron Diffraction During Crystal Growth* [Internet]. Berlin, Heidelberg: Springer; 1999 [cited 2024 Jul 31]. p. 75–89. Available from: https://doi.org/10.1007/BFb0109553

32. Wang R, Boschker JE, Bruyer E, Sante DD, Picozzi S, Perumal K, et al. Toward Truly Single Crystalline GeTe Films: The Relevance of the Substrate Surface. *J Phys Chem C.* 2014 Dec 26;118(51):29724–30.

33. Perumal K. *Epitaxial growth of Ge-Sb-Te based phase change materials* [Internet] [Doctoral Thesis]. Humboldt-Universität zu Berlin, Mathematisch-Naturwissenschaftliche Fakultät I; 2013 [cited 2024 Oct 1]. Available from: https://edoc.hu-berlin.de/handle/18452/17467

34. Mengui UA, Abramof E, Rappl PHO, Ueta AY. Characterization of SnTe films grown by molecular beam epitaxy. *Braz J Phys*. 2006 Jun;36(2a):324–7.

35. Yan CH, Guo H, Wen J, Zhang ZD, Wang LL, He K, et al. Growth of topological crystalline insulator SnTe thin films on Si(111) substrate by molecular beam epitaxy. *Surface Science.* 2014 Mar 1;621:104–8.

36. Kaminski M, Wuttig M, Waser R. *Phase change superlattices and thin film effects: MBE-growth and characterization*. [Aachen]; 2020.

37. Shi W, Gao M, Wei J, Gao J, Fan C, Ashalley E, et al. Tin Selenide (SnSe): Growth, Properties, and Applications. *Advanced Science.* 2018;5(4):1700602.

38. Kanaya K, Okayama S. Penetration and energy-loss theory of electrons in solid targets. *J Phys D: Appl Phys.* 1972 Jan;5(1):43.

39. Hasegawa S. Time-resolved reflection high-energy electron diffraction. In: Kaufmann EN, editor. *Characterization of Materials*. Hoboken, NJ: Wiley & Sons, Inc.; 2012. p. 1925–38.

40. Ingle NJC. Inelastic scattering techniques for in situ characterization of thin film growth: backscatter Kikuchi diffraction. In: Koster G, Rijnders G, editors. *In Situ Characterization of Thin Film Growth* [Internet]. Woodhead Publishing; 2011 [cited 2024 Jul 31]. p. 29–51. Available from: https://www.sciencedirect.com/science/article/pii/B9781845699345500023

41. Braun W, Möller H, Zhang YH. Reflection high-energy electron diffraction during substrate rotation: A new dimension for in situ characterization. *J Vac Sci Technol B Microelectron Nanometer Struct Process Meas Phenom*. 1998 May;16(3):1507–10.

42. Abukawa T, Yamazaki T, Yajima K, Yoshimura K. Weissenberg Reflection High-Energy Electron Diffraction for Surface Crystallography. *Phys Rev Lett.* 2006 Dec 13;97(24):245502.

43. Satapathy DK, Jenichen B, Ploog KH, Braun W. Azimuthal reflection high-energy electron diffraction study of MnAs growth on GaAs(001) by molecular beam epitaxy. *Journal of Applied Physics.* 2011 Jul 20;110(2):023505.

44. Harrington GF, Santiso J. Back-to-Basics tutorial: X-ray diffraction of thin films. *J Electroceram.* 2021 Dec 1;47(4):141–63.

45. Pohlmann M, Wuttig M, Mayer J. *Structure and growth characterization of biaxially textured PCM thin films and heterostructures* [thesis]. Aachen: RWTH Aachen University; 2020.

46. Lo RL, Ho MS, Hwang IS, Tsong TT. Diffusion by bond hopping of hydrogen atoms on the Si(111)-7×7 surface. Phys Rev B. 1998 Oct 15;58(15):9867–75.

47. Tokumoto H. High Temperature Dynamic Behavior of Silicon Surfaces Studied by STM. In: Gai PL, editor. *In-Situ Microscopy in Materials Research: Leading International Research in Electron and Scanning Probe Microscopies* [Internet]. Boston, MA: Springer US; 1997 [cited 2024 Jul 30]. p. 263–82. Available from: https://doi.org/10.1007/978-1-4615-6215-3_11

48. Rowe JE, Ibach H. Surface and Bulk Contributions to Ultraviolet Photoemission Spectra of Silicon. *Phys Rev Lett.* 1974 Feb 25;32(8):421–4.

49. Takayanagi K, Tanishiro Y, Takahashi M, Takahashi S. Structural analysis of Si(111)-7×7 by UHV-transmission electron diffraction and microscopy. *J Vac Sci Technol A.* 1985 May;3(3):1502–6.

50. Wang J, Jin L, Zhou H, Fu H, Song C, Meng S, et al. Direct imaging of surface states hidden in the third layer of Si(111)-7×7 surface by Pz-wave tip. *Appl Phys Lett.* 2018 Jul 17;113:031604.

51. Nagayoshi H. Theoretical study of the electronic structure of the Si(111)-√3×√3:Sb surface. *Surf Sci.* 1993 Feb 10;282(1):163–72.

52. Nakatani S, Kuwahara Y, Takahashi T, Aono M. Structure determination of Si(111)-√3×√3–Sb surface by X-ray diffraction. *Surf Sci.* 1996 Jun 20;357–358:65–8.

53. Park CY, Abukawa T, Kinoshita T, Enta Y, Kono S. Low Energy Electron Diffraction and X-Ray Photoelectron Spectroscopy Studies of the Formation of Submonolayer Interfaces of Sb/Si(111). *Jpn J Appl Phys.* 1988 Jan;27(1R):147.

54. Kim C, Walko DA, Robinson IK. Refined structure of (√3 × √3) Sb/Si(111). *Surf Sci.* 1997 Oct 23;388(1):242–7.

55. Lüpke F, Just S, Bihlmayer G, Lanius M, Luysberg M, Doležal J, et al. Chalcogenide-based van der Waals epitaxy: Interface conductivity of tellurium on Si(111). *Phys Rev B.* 2017 Jul 5;96(3):035301.

56. Gervacio-Arciniega JJ, Prokhorov E, Espinoza-Beltrán FJ, Trapaga G. Characterization of local piezoelectric behavior of ferroelectric GeTe and $Ge_2Sb_2Te_5$ thin films. *J Appl Phys.* 2012 Sep 4;112(5):052018.

57. Polking MJ, Han MG, Yourdkhani A, Petkov V, Kisielowski CF, Volkov VV, et al. Ferroelectric order in individual nanometre-scale crystals. *Nat Mater.* 2012 Jul;11(8):700–9.

58. Liebmann M, Rinaldi C, Di Sante D, Kellner J, Pauly C, Wagner R, et al. Giant Rashba-type spin splitting in ferroelectric GeTe(111). *Adv Mater* [Internet]. 2016 Jan 20 [cited 2024 Oct 14];28(3). Available from: https://pubmed.ncbi.nlm.nih.gov/26599640/

59. Chen M, Rubin KA, Barton RW. Compound materials for reversible, phase-change optical data storage. *Applied Physics Letters.* 1986 Sep 1;49(9):502–4.

60. Wang R, Zhang W, Momand J, Ronneberger I, Boschker JE, Mazzarello R, et al. Formation of resonant bonding during growth of ultrathin GeTe films. *NPG Asia Mater.* 2017 Jun;9(6):e396.

61. Chattopadhyay T, Boucherle JX, vonSchnering HG. Neutron diffraction study on the structural phase transition in GeTe. *J Phys C: Solid State Phys.* 1987 Apr;20(10):1431.

62. Matsunaga T, Fons P, Kolobov AV, Tominaga J, Yamada N. The order-disorder transition in GeTe: Views from different length-scales. *Applied Physics Letters.* 2011 Dec 8;99(23):231907.

63. Momma K, Izumi F. VESTA: a three-dimensional visualization system for electronic and structural analysis. *J Appl Cryst.* 2008 Jun 1;41(3):653–8.

64. Bletskan DI. Phase Equilibrium in the Systems A^{IV}—B^{VI}. Part 2: Systems germanium–chalcogen. *J Ovonic Res*. 2005;1(5):53–60.

65. Giussani A, Perumal K, Hanke M, Rodenbach P, Riechert H, Calarco R. On the epitaxy of germanium telluride thin films on silicon substrates. *Physica Status Solidi (b).* 2012;249(10):1939–44.

66. Wang R, Campi D, Bernasconi M, Momand J, Kooi BJ, Verheijen MA, et al. Ordered Peierls distortion prevented at growth onset of GeTe ultra-thin films. *Sci Rep.* 2016 Sep 9;6(1):32895.

67. Hsieh TH, Lin H, Liu J, Duan W, Bansil A, Fu L. Topological crystalline insulators in the SnTe material class. *Nat Commun.* 2012 Jul 31;3(1):982.

68. Tanaka Y, Ren Z, Sato T, Nakayama K, Souma S, Takahashi T, et al. Experimental realization of a topological crystalline insulator in SnTe. *Nature Phys.* 2012 Nov;8(11):800–3.

69. Cardona M, Greenaway DL. Optical Properties and Band Structure of Group IV-VI and Group V Materials. *Phys Rev.* 1964 Mar 16;133(6A):A1685–97.

70. Tung YW, Cohen ML. Relativistic Band Structure and Electronic Properties of SnTe, GeTe, and PbTe. *Phys Rev.* 1969 Apr 15;180(3):823–6.

71. Pawley GS, Cochran W, Cowley RA, Dolling G. Diatomic Ferroelectrics. *Phys Rev Lett.* 1966 Oct 3;17(14):753–5.

72. Allen PB, Cohen ML. Carrier-Concentration-Dependent Superconductivity in SnTe and GeTe. *Phys Rev.* 1969 Jan 10;177(2):704–6.

73. Savage HT, Houston B, Burke JR. Fermi-Surface Studies in SnTe. *Phys Rev B.* 1972 Sep 15;6(6):2292–304.

74. Akiyama R, Fujisawa K, Sakurai R, Kuroda S. Weak antilocalization in (111) thin films of a topological crystalline insulator SnTe. *J Phys: Conf Ser.* 2014 Dec;568(5):052001.

75. Assaf BA, Katmis F, Wei P, Satpati B, Zhang Z, Bennett SP, et al. Quantum coherent transport in SnTe topological crystalline insulator thin films. *Applied Physics Letters.* 2014 Sep 12;105(10):102108.

76. Yan C, Liu J, Zang Y, Wang J, Wang Z, Wang P, et al. Experimental Observation of Dirac-like Surface States and Topological Phase Transition in $Pb_{1-x}Sn_xTe(111)$ Films. *Phys Rev Lett.* 2014 May 5;112(18):186801.

77. Chang K, Liu J, Lin H, Wang N, Zhao K, Zhang A, et al. Discovery of robust in-plane ferroelectricity in atomic-thick SnTe. *Science.* 2016 Jul 15;353(6296):274–8.

78. Plekhanov E, Barone P, Di Sante D, Picozzi S. Engineering relativistic effects in ferroelectric SnTe. *Phys Rev B.* 2014 Oct 28;90(16):161108.

79. Aggarwal L, Banik A, Anand S, Waghmare UV, Biswas K, Sheet G. Local ferroelectricity in thermoelectric SnTe above room temperature driven by competing phonon instabilities and soft resonant bonding. *Journal of Materiomics.* 2016 Jun 1;2(2):196–202.

80. Moshwan R, Yang L, Zou J, Chen ZG. Eco-Friendly SnTe Thermoelectric Materials: Progress and Future Challenges. *Advanced Functional Materials.* 2017;27(43):1703278.

81. Riedl HR, Schoolar RB, Houston B. Preparation of epitaxial SnTe films of controlled carrier concentration. *Solid State Communications.* 1966 Aug 1;4(8):399–402.

82. Ishikawa R, Yamaguchi T, Ohtaki Y, Akiyama R, Kuroda S. Thin film growth of a topological crystal insulator SnTe on the CdTe (111) surface by molecular beam epitaxy. *Journal of Crystal Growth.* 2016 Nov 1;453:124–9.

83. Höchst H, Niles DW, Engelhardt MA, Hernández-Calderón I. Strained-layer epitaxy of SnTe on CdTe(110). *Journal of Vacuum Science & Technology A.* 1989 May 1;7(3):775–9.

84. Stoemenos J, Vincent R. Twining faults in epitaxial films of germanium telluride and GeTe-SnTe alloys. *Physica Status Solidi (a).* 1972;11(2):545–58.

85. Taskin AA, Yang F, Sasaki S, Segawa K, Ando Y. Topological surface transport in epitaxial SnTe thin films grown on Bi_2Te_3. *Phys Rev B*. 2014 Mar 17;89(12):121302.

86. Zhang D, Baek H, Ha J, Zhang T, Wyrick J, Davydov AV, et al. Quasiparticle scattering from topological crystalline insulator SnTe (001) surface states. *Phys Rev B.* 2014 Jun 27;89(24):245445.

87. Wirtssohn M. *Study on growth of epitaxial single-domain tin-telluride and epitaxial antimony on silicon and sputter-grown bismuth-tin-telluride nanowhiskers*. [PhD thesis]. Aachen: RWTH Aachen University; 2019.

88. Li Z, Sun L, Liu Y, Zhu L, Yu D, Wang Y, et al. SnSe@SnO2 core–shell nanocomposite for synchronous photothermal–photocatalytic production of clean water. *Environ Sci: Nano.* 2019 May 16;6(5):1507–15.

89. Yılmaz S, Başol BM, Polat İ, Olğar MA, Bayazıt T, Küçükömeroğlu T, et al. Improvement in performance of SnSe-based photodetectors via post deposition sulfur diffusion. *Sensors and Actuators A: Physical.* 2024 Jul 1;372:115348.

90. Chung KM, Wamwangi D, Woda M, Wuttig M, Bensch W. Investigation of SnSe, $SnSe_2$, and Sn_2Se_3 alloys for phase change memory applications. *Journal of Applied Physics.* 2008 Apr 21;103(8):083523.

91. Rani S, Kumar M, Garg P, Parmar R, Kumar A, Singh Y, et al. Temperature-Dependent n–p–n Switching and Highly Selective Room-Temperature n-SnSe2/p-SnO/n-SnSe Heterojunction-Based NO2 Gas Sensor. *ACS Appl Mater Interfaces*. 2022 Apr 6;14(13):15381–90.

92. Kim Y, Kim Y, Park Y, Jo YN, Kim YJ, Choi NS, et al. SnSe alloy as a promising anode material for Na-ion batteries. *Chem Commun.* 2014 Dec 2;51(1):50–3.

93. Dar MA, Majid SR, Satgunam M, Batoo KM, Kalpana S, Arularasan P, et al. Electrochemical performance of Fe-doped SnSe material electrodes for supercapacitors. *Journal of Energy Storage.* 2024 Jul 30;94:112403.

94. Sun Y, Zhong Z, Shirakawa T, Franchini C, Li D, Li Y, et al. Rocksalt SnS and SnSe: Native topological crystalline insulators. *Phys Rev B.* 2013 Dec 19;88(23):235122.

95. Zhou C, Lee YK, Yu Y, Byun S, Luo ZZ, Lee H, et al. Polycrystalline SnSe with a thermoelectric figure of merit greater than the single crystal. *Nat Mater.* 2021 Oct;20(10):1378–84.

96. Dar MA, Ahmed SR, Rather MA, Kalpana S, Rather AA, Ahamed SR, et al. The features of the solvothermal synthesis of SnSe nanosheets and nanoflowers for supercapacitor applications. *Inorganic Chemistry Communications.* 2023 Jul 1;153:110838.

97. Zhong Y, Zhang L, Sun M, Wang M, Chen W, Lin S, et al. Large scale self-assembly of SnSe nanosheets prepared by the hot-injection method for photodetector and capacitor applications. *Materials Today Energy*. 2019 Jun 1;12:418–25.

98. Govindan V, Kashinath L, Geetha GV, Senthilpandian M, Ramasamy P, Sankaranarayanan K. One-pot microwave synthesis of SnSe and Lanthanum doped SnSe nanostructure with direct Z scheme pattern for excellent photodegradation of organic pollutants. *Ceramics International.* 2022 May 1;48(9):12228–39.

99. Zhao LD, Lo SH, Zhang Y, Sun H, Tan G, Uher C, et al. Ultralow thermal conductivity and high thermoelectric figure of merit in SnSe crystals. *Nature.* 2014 Apr;508(7496):373–7.

100. Han Y, Yu J, Zhang H, Xu F, Peng K, Zhou X, et al. Photoinduced Ultrafast Symmetry Switch in SnSe. *J Phys Chem Lett.* 2022 Jan 20;13(2):442–8.

101. Nguyen VQ, Duong VT, Nguyen TH, Kang R, Pham AT, Tran VT, et al. Se/Sn flux ratio effects on epitaxial SnSe thin films; crystallinity & domain rotation. *Journal of Alloys and Compounds.* 2020 Nov 5;840:155680.

102. Xie Y, Zhou Y, Gong XG. The intrinsic low lattice thermal conductivity in the rock salt SnSe. *Computational Materials Science.* 2018 Jun 1;148:54–9.

103. Okamoto H. Se-Sn (Selenium-Tin). *J Phase Equil.* 1998 Jun 1;19(3):293–293.

104. Tracy BD, Li X, Liu X, Furdyna J, Dobrowolska M, Smith DJ. Characterization of structural defects in SnSe2 thin films grown by molecular beam epitaxy on GaAs (111)B substrates. *Journal of Crystal Growth.* 2016 Nov 1;453:58–64.

105. Kerres P, Zhou Y, Vaishnav H, Raghuwanshi M, Wang J, Häser M, et al. Scaling and Confinement in Ultrathin Chalcogenide Films as Exemplified by GeTe. *Small.* 2022;18(21):2201753.

106. Xue F ning, Zhao Z hao, Zhang Y, Liu T, Lu Y, Zhang J cai. Layer-dependent electronic structure, dynamic stability, and phonon properties of few-layer SnSe. *Phys Rev B.* 2022 Sep 1;106(10):104301.

Acknowledgements

I would like to express my heartfelt gratitude to my doctoral supervisor, Prof. Dr. Matthias Wuttig, for granting me the opportunity to engage in fundamental research in thin films and for instilling in me a deep enthusiasm for chalcogenide materials. Throughout my doctoral journey, his invaluable guidance and insightful suggestions during numerous intensive discussions have greatly shaped my research. Through Prof. Wuttig's mentorship, I consistently found opportunities to push my boundaries and grow as a researcher. I sincerely thank him for his unwavering support.

Thank you Prof. Joachim Mayer for being my second examiner. A couple of technical discussion with you in the start of my research and your insight into the field of thin film has guided me on various occasions during the course of this work.

I am also deeply grateful to Prof. Arnab Bhattacharya for his insightful feedback and encouragement during my research. His expertise and perspective have been invaluable to both my academic and personal growth.

Additionally, I would like to extend my appreciation to all members of the MBE Group. In my first year, Marvin Kaminski played a crucial role; without his expertise, I would have faced significant challenges in starting my journey with MBE growth.

My thanks go to Jalil Abdur Rehman for his exceptional teamwork and the seamless collaboration we shared. I also thank Peter Kerres for our collaborative work; thanks to him, I maintained a strong connection to Aachen. A special thanks to all Aachen team members for their support. Thanks to Christoph Ringkamp and Mohit Raghuwanshi.

A very special thanks to my colleagues at the nanocluster. In particular, Christoph Krause and Benjamin Bennemann were always there to answer my technical questions, making a significant impact on my research journey.

Thank you, Ted Engels, for motivating me throughout my journey. A heartfelt thank you to Cheshta Jaitely, Ruchi Kamdar, Binny Rudani, Shuping and Aida for continuously encouraging me to persevere in writing my thesis.

Thank you Emroj Hossian, A Azizur Rahman for all your support for defense preparation.

Finally, I want to express my gratitude to all who have supported me, directly or indirectly, in pursuing my dream.